



CERN-SPSC-2023-033 / SPSC-P-369

31 October 2023

BDF/SHiP at the ECN3 high-intensity beam facility

Proposal

SHiP Collaboration¹ with support from the BDF Working Group ²

Abstract

The BDF/SHiP collaboration has proposed a general-purpose intensity-frontier experimental facility operating in beam-dump mode at the CERN SPS accelerator to search for feebly interacting GeV-scale particles and to perform measurements in neutrino physics. CERN is uniquely suited for this programme owing to the proton energy and yield available at the SPS. This puts BDF/SHiP in a unique position worldwide to make a breakthrough in a theoretically and experimentally attractive range of the FIP parameter space that is not accessible to other experiments. The existing ECN3 experimental facility makes it possible to implement BDF at a fraction of the cost of the original proposal, without compromising on the physics scope and the physics reach. SHiP has demonstrated the feasibility to construct a large-scale, versatile discovery experiment capable of coping with 4×10^{19} protons per year at 400 GeV/c and ensuring a < 1 -event background for the FIP decay search even up to 6×10^{20} PoT. With the feasibility of the facility and the detector proven, the BDF/SHiP collaboration are ready to proceed with the TDR studies and commence implementation in CERN's Long Shutdown 3. During the operational lifetime of BDF/SHiP, several prominent opportunities for upgrades and extensions are open, such as the use of a LAr TPC, a synergistic tau flavour violation experiment, and exploiting the secondary mixed-field radiation from the proton target for nuclear and astrophysics, as well as for material testing.

Keywords: Beam Dump Facility, BDF, SHiP, SPS, ECN3

Contacts: Andrey.Golutvin@cern.ch, Richard.Jacobsson@cern.ch

¹Complete author list at the end

²Complete list of contributors in Acknowledgments

Contents

1 Physics programme	2
1.1 FIP physics programme	4
1.2 Light dark matter physics programme	8
1.3 Neutrino physics programme	9
2 BDF/SHiP at ECN3	14
2.1 MC simulation	14
2.2 Beam requirements and delivery	15
2.3 Production target and target complex	16
2.4 Muon shield	21
2.5 Overview of the SHiP detector	27
2.5.1 Scattering and Neutrino Detector	28
2.5.2 Hidden Sector Decay Spectrometer	29
2.6 Integration and civil engineering	29
2.7 Radiation protection	31
2.8 Evaluation of radiation to electronics	34
3 Detector status and R&D	38
3.1 SND	38
3.1.1 Emulsion target	38
3.1.2 Target tracker	39
3.1.3 Muon spectrometer	40
3.2 HSDS	41
3.2.1 Decay volume	41
3.2.2 Upstream background tagger	44
3.2.3 Surrounding background tagger	46
3.2.4 Spectrometer magnet	49
3.2.5 Main tracker	52
3.2.6 Timing detector	55
3.2.7 Particle identification detectors and photon detection	57
3.3 Common detector electronics and online system	59
4 Physics performance	62
4.1 FIP decay search performance	62
4.2 FIP decay search background analysis	69
4.2.1 Muon-induced background	69
4.2.2 Neutrino-induced background	71
4.2.3 Studies with He-filled decay volume	71
4.3 Scattering-signature search performance	72
4.4 Neutrino physics performance	74
4.4.1 Muon identification	75
4.4.2 Hadronic energy measurement	76
4.4.3 Tau neutrino detection	78
4.4.4 Neutrino-induced charm production	79

4.4.5	Tau neutrino magnetic moment	80
4.5	Measurement of charm production with the BDF/SHiP prototype target	81
5	Road map and detector cost	83
5.1	Detector cost	85
5.2	Status of the Collaboration	87
6	Future upgrades and extensions of the facility	89
6.1	Spill intensity increase	89
6.2	Opportunities with BDF irradiation stations	90
6.3	Liquid argon TPC detector for extending searches for FIPs	93
6.3.1	Physics reach with a LAr TPC detector	95
6.4	Tau lepton flavour violation experiment	95
	Acknowledgements	99
	References	100
	Author list	114

1 Physics programme

In spite of the remarkable achievements of the Standard Model (SM) of particle physics, substantial evidence supports the existence of new physics that goes beyond its scope. Among various shortcomings, the SM as-is cannot account for neutrino flavor oscillations, dark matter, and generation of the matter-antimatter asymmetry in the early Universe.

However, there is no solid predictions of where to search for this "new physics". New particles capable of resolving the problems of the SM can have masses from sub-eV to Planck scale and coupling constants with SM particles ranging many orders of magnitude. At this crossroad point of particle physics, it is essential to use efficiently available and planned experimental facilities to push forward different frontiers of physics, probing whole classes of models simultaneously.

The quest for heavy new particles is carried out through two principal strategies: direct search experiments (e.g. ATLAS and CMS) and indirect searches (e.g. flavour physics experiments, like LHCb and NA62). While from the perspective of theory, both types of experiments are pushing the "energy frontier", experimentally flavour physics experiments rely heavily on high intensity to probe higher energy realms, higher than those reachable by direct search experiments.

If the mass of a new particle is below the electroweak (EW) scale, it becomes possible for this particle to be generated at accelerators, not only as a resonance but also through the decay processes of Standard Model (SM) particles, such as the heavy bosons W, Z, H^0 , as well as mesons like π, D and B . This characteristic makes the mass range of these new particles particularly intriguing from an experimental perspective.

The reason that such new particles have not yet been detected may not be due to a limitation in accelerator energy, but rather because their production is exceedingly rare. Past experiments and those currently taking data worldwide have conducted numerous searches, leading to constraints on sizeable coupling constants. This is precisely why new particles of this nature are often referred to as feebly-interacting particles, or FIPs (see e.g. [1, 2]). In the absence of a specific reason, such as a symmetry that enforces particle stability, the lifetime of these new particles is related to their coupling constant g and mass m_{FIP} as $\tau_{\text{FIP}} \propto g^{-2} m_{\text{FIP}}^{-\alpha}$ where $\alpha = 1 - 5$ [3]. Efficient exploration of the FIP parameter space thus requires the adoption of distinct search strategies depending on the lifetime of the feebly-interacting particles. Feebly-interacting particles (FIPs) with lifetimes $c\tau_{\text{FIP}} \gtrsim 1 \text{ mm}$ can be effectively probed using displaced-vertices techniques at the LHC and upcoming colliders [4, 5, 6, 7]. The relatively long lifetime enables the distinction of these FIPs from various Standard Model (SM) background events, which typically occur at shorter displacements. However, the lifetime of FIPs cannot be excessively long to be effectively searched for at colliders. This limitation arises because collider detectors can only probe decay signatures over relatively short distances, typically on the order of $\mathcal{O}(1) \text{ m}$, as determined by the dimensions of their inner trackers [4]. Consequently, long-lived FIPs predominantly undergo decay outside the fiducial volume. Additionally, in order to minimise Standard Model (SM) backgrounds, stringent selection criteria must be applied. These criteria typically involve considering specific kinematic properties and final states, which can lead to low signal efficiencies. For instance, recent searches for Heavy Neutral Leptons (HNLs) at CMS [4] achieved a typical selection efficiency of the order of 1%. Consequently, even if a long-lived FIP decays within

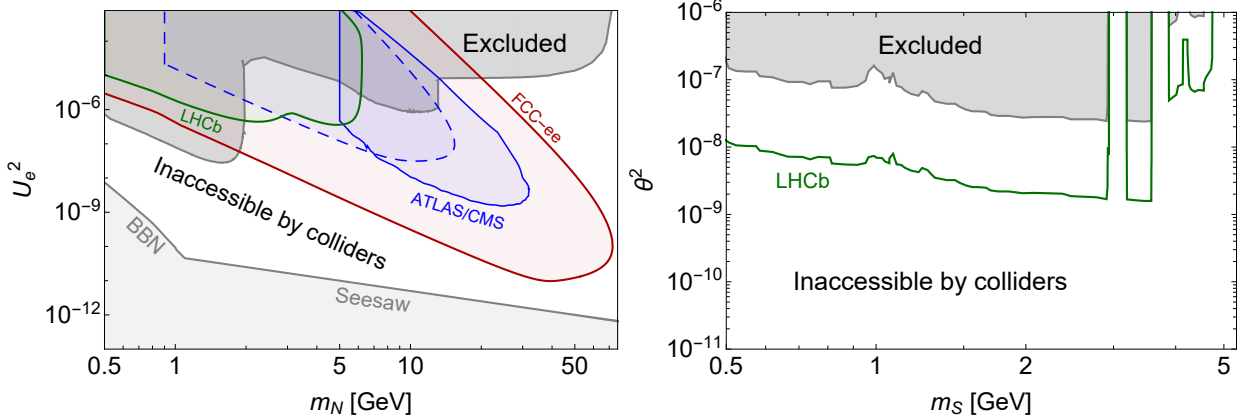


Figure 1: The potential of future collider searches to probe the parameter space of feebly-interacting particles in the plane FIP mass - FIP coupling to SM particles. Left: parameter space of heavy neutral leptons (HNLs) that mix with electron neutrinos. The see-saw line is included as a visual guide. It is only defined for the total mixing angle $U^2 = |U_e|^2 + |U_\mu|^2 + |U_\tau|^2$. HNLs with the total mixing below the see-saw line do not contribute to the neutrino mass generation. Right: dark scalars mixing with Higgs bosons. The figures demonstrate that colliders cannot efficiently explore the parameter space of FIPs with mass of the order of GeV/c^2 . Instead this parameters space, and similarly for other feebly-interacting particles, can be more efficiently explored in the coming years with beam dump experiments. The parameter space excluded by past experiments is taken from [8].

the tracker region, the event is likely to fall outside the selection acceptance, making it challenging to identify and isolate these FIPs efficiently. Such a limitation becomes crucial in the domain of small FIP masses, where the FIP lifetimes are parametrically very large and are out of the colliders' accessibility. Effectively, the LHC experiments in the high luminosity phase [5, 7] and lepton collider experiments [6] are mainly sensitive to lifetimes $c\tau_N \lesssim \mathcal{O}(100) \text{ m}$. As illustrated in Figure 1, the scaling of the HNL lifetime with the mass as $\tau_N \propto m_N^{-5} U_e^{-2}$ imply that collider experiments have poor sensitivity to masses $m_N \lesssim 10 \text{ GeV}/c^2$. For dark scalars, due to the strict event selection to cope with the backgrounds and the available triggers, the event rate with displaced vertices at collider experiments is insufficient to provide a competitive sensitivity. The situation is similar for the other types of FIPs.

While high-energy exploration forms the mainstay of experimental particle physics, characterised by a well-structured program including initiatives like the Future Circular Collider, the current landscape is yet to feature a dedicated, flagship experiment targeting small couplings. Ideally, it would not only be capable of simply probing the couplings, but also, in case a signal is observed, identify the properties of the FIP such as its mass, spin, decay modes, or its relation to the BSM problems, which may be achieved if the event kinematics is fully reconstructed.

The Search for Hidden Particles (SHiP) experiment at the SPS [9, 10, 11, 12] is designed to fill this gap. Its mission is to serve as the leading experiment for the exploration of the FIP sector with small masses $m < 5 \text{ GeV}/c^2$ and low couplings. Although having a much lower

centre-of-mass energy of collisions than at colliders, it can deliver extremely high luminosity by operating with a more intensive proton beam combined with a high-A/Z target. This means in particular that an unprecedented number of D , as well as a large number of B , mesons can be produced and subsequently decay into FIPs, in the mass range of interest, within a relatively small forward solid angle. There is no limitation on the decay volume length. It can easily be several tens of metres to cover a much larger lifetime acceptance than at collider detectors. Moreover, backgrounds can be significantly reduced by placing the decay volume behind a chain of components designed to suppress beam-induced particle backgrounds, such as a hadron absorber and a muon deflector, considerably reducing the need to impose strict signal selection criteria. Finally, SHiP is designed to fully reconstruct the signal kinematics.

By pushing the boundaries of small coupling and low mass investigations, the implementation of the SHiP experiment serves to enrich the tapestry of high-energy physics research, introducing a vital diversification to the planned experimental programmes.

1.1 FIP physics programme

Should new physics prove to be both heavy and weakly interacting, it may elude experimental detection in the foreseeable future. However, compelling arguments suggest a pursuit of FIPs with masses comparable to known Standard Model particles. These FIPs could provide answers to several persistent conundrums within the Standard Model, such as the nature of neutrino masses and oscillations, the existence of dark matter, and the baryon-antibaryon asymmetry in the universe.

For a comprehensive review of FIP models, see reference [3]. The strategy employed by SHiP hinges on the high-intensity proton beam of the SPS, dumped onto a heavy target to produce FIPs, with search for decays within an isolated fiducial volume, distinct from Standard Model background. The characteristic experimental signature of these FIPs is a reconstructed isolated vertex pointing back towards the proton target.

Such a strategy facilitates an inclusive search for FIPs in the $\text{MeV}/c^2\text{-GeV}/c^2$ range, providing sensitivity to a wide array of existing models, as well as sensitivity and constraints to models that may be formulated in the future. Key among the models that SHiP stands to investigate are heavy neutral leptons (HNLs), dark scalars, dark vectors, axion-like particles (ALPs), and light dark matter (LDM). These models have served as benchmarks in the design and optimisation process of the experiment and are briefly described in the following sections. Examples of physics models with feebly interacting particles and the corresponding final states are listed in Table 1.

Many FIP models occupy a broad parameter space, yet some can be restricted through cosmological factors. For instance, HNLs can be constrained by factors such as baryon-antibaryon asymmetry, dark matter, and neutrino mixing. Although parts of the HNL parameter space is experimentally unreachable, SHiP aims at exploring a significant portion that is accessible to experiments.

The redundant selection strategy chosen by SHiP enables direct background measurements within the experiment itself. For example, in the case of fully reconstructed signals, the backgrounds can be minimised to an inconsequential level without relying on the veto systems, as discussed in Section 4.1. This allows the veto to be used for calculating the

Physics model		Final state
HSDS	SUSY neutralino	$\ell^\pm\pi^\mp, \ell^\pm K^\mp, \ell^\pm\rho^\mp, \ell^+\ell^-\nu$
	Dark photons	$\ell^+\ell^-, 2\pi, 3\pi, 4\pi, KK, q\bar{q}, D\bar{D}$
	Dark scalars	$\ell\ell, \pi\pi, KK, q\bar{q}, D\bar{D}, GG$
	ALP (fermion coupling)	$\ell^+\ell^-, 3\pi, \eta\pi\pi, q\bar{q}$
	ALP (gluon coupling)	$\pi\pi\gamma, 3\pi, \eta\pi\pi, \gamma\gamma$
	HNL	$\ell^+\ell'^-\nu, \pi l, \rho l, \pi^0\nu, q\bar{q}'l$
	Axino	$\ell^+\ell^-\nu$
	ALP (photon coupling)	$\gamma\gamma$
SND	SUSY sgoldstino	$\gamma\gamma, \ell^+\ell^-, 2\pi, 2K$
	LDM	electron, proton, hadronic shower
	$\nu_\tau, \bar{\nu}_\tau$ measurements	τ^\pm
Neutrino-induced charm production (ν_e, ν_μ, ν_τ)		$D_s^\pm, D^\pm, D^0, \overline{D^0}, \Lambda_c^+, \overline{\Lambda_c^-}$

Table 1: Examples of the physics models and final states that the SHiP’s scattering and neutrino detector (SND) and the hidden sector decay spectrometer (HSDS) are sensitive to. Here, $\ell = e, \mu, \tau$, and the abbreviates are HNL=heavy neutral lepton, ALP=axion-like particle, LDM=light dark matter.

expected background, leveraging on the factorisation of different selection criteria. Finally, even if only a single event is observed, the nominal selection criteria can be relaxed to employ the invariant mass and particle identification as additional, potent means of identifying new signals.

Heavy neutral leptons

Heavy neutral leptons (HNLs) are formed through mixing interactions with active neutrinos. The strength of this mixing is characterized by the mixing angle, denoted by U_ℓ^2 , where $\ell = e, \mu, \tau$.

HNL production is dependent on their mass. For HNLs with low mass (below $5 \text{ GeV}/c^2$), the primary production processes are semi-leptonic decays of the type $h \rightarrow \ell^\pm NX$, and fully leptonic decays $h^\pm \rightarrow \ell^\pm N$, where h stands for K, D and B . For those with higher mass, the dominant production mechanisms involve decays of W and Z bosons. This classification naturally bifurcates the sensitivity regions into two: low-mass HNLs, where beam-dump experiments hold sway, and high-mass HNLs, where collider experiments dominate.

Following production, HNLs with masses $m_N \lesssim 1 \text{ GeV}/c^2$ decay predominantly via two channels, $N \rightarrow h\ell$ or $N \rightarrow \ell\ell'\nu$, where h represents a hadron, ℓ and ℓ' are leptons, and ν denotes a neutrino. In the case of high mass HNLs $m_N \gtrsim 1 \text{ GeV}/c^2$, the two quarks present in the decay channel $N \rightarrow q\bar{q}'\ell$ do not undergo hadronisation together. This leads to an experimental signature consisting of two jets and a charged lepton. The relative probabilities of these decay channels further depend on the mass and mixing angles of the HNLs.

Numerous experiments have sought HNLs, with the current boundaries approaching the theoretically most intriguing region. The main motivation for the HNLs is that they may provide a simple explanation of the observed active neutrino masses via the GeV see-saw mechanism [13]. For this, however, (i) at least two HNLs are required to explain the observed

neutrino mass differences $\Delta m_{\text{solar}}^2, \Delta m_{\text{atm}}^2$; (ii) their coupling constants U should be above the "see-saw line" in Figure 1 [3].

Apart from generating neutrino masses, HNLs in this region can explain the baryon-antibaryon asymmetry observed in the Universe [14].

The SHiP experiment offers the opportunity to explore a substantial portion of this theoretically intriguing region. The experiment's unique capabilities position it well for detecting and studying these elusive particles. It can probe the domain of mixing angles where the HNLs may be responsible for the resolution of the BSM problems by careful reconstruction of the properties of the HNLs, such as their nature – Dirac or Majorana [15], mass, and the mixing angles pattern [16].

Dark vectors

Dark photons (DP), which mix with SM photons through a coupling parameter represented by ϵ , are quintessential examples of dark vectors. These particles are predicted by several extensions of the SM.

They can be generated through the decay of mesons into photons, where one of the photons mixes with the dark photon. This leads to decays such as $\pi^0/\eta \rightarrow A'\gamma$, where A' denotes the dark photon. Following the same principle, the dark photon can decay by mixing back into a photon. Heavier dark photons may be also produced by the proton bremsstrahlung mechanism or deep inelastic scattering (via the Drell-Yan process) [1].

The branching ratios of dark photons (A') decays can be precisely predicted by using the measurement of $e^+e^- \rightarrow \gamma \rightarrow X$, where $X = f\bar{f}, 3\pi, \dots$ represents the full set of final states [17]. Although numerous experiments have established constraints on dark photons, a large portion of the parameter space remains unexplored. This leaves ample opportunity for new insights and discoveries in the realm of dark sector physics. Of particular interest is the domain of relatively short lifetimes of $c\tau \ll 1\text{ m}$, where dark photons may be mediators for light dark matter particles χ with mass $2m_\chi > m_{A'}$ [18]. Due to a large beam energy and the on-axis placement, SHiP may explore this domain. Beyond this, it would allow exploring the dark photon masses $m_{A'} \simeq 4\text{ GeV}/c^2$, which is well above what is excluded by past experiments.

Dark scalars

From a theoretical perspective, dark scalars (DS) are intriguing due to their potential role in some of the open problems in particle physics and cosmology. For instance, if dark scalars exist and interact weakly with SM particles, they could potentially account for the elusive dark matter [19, 20].

Moreover, dark scalars are often considered in the framework of hidden sector models that assume the existence of particles and interactions separated from the Standard Model particles and their interactions. In these models, the Higgs portal, characterised by the mixing parameter Θ^2 , often serves as the only means of communication between the hidden sector, containing the dark scalars, and the SM sector.

Furthermore, the mass-dependent branching fractions of the dark scalar pose intriguing implications for particle physics and cosmology. If the mass of the dark scalar is less than

twice the mass of certain SM particles, decays into those particles are kinematically forbidden. This can lead to a highly asymmetric decay pattern, which may influence the dynamics of the early Universe, including the processes of baryogenesis and leptogenesis [21]. It is also worth noting that dark scalars could be instrumental in solving the hierarchy problem [22].

Given that any interaction with SM particles is mediated through the mixing with the Higgs boson, the branching fraction of the dark scalar decaying into a pair of SM particles is inherently a function of their mass.

Common decay channels for the dark scalar include electron-positron pairs (e^+e^-), muon-antimuon pairs ($\mu^+\mu^-$), tau-anti-tau pairs ($\tau^+\tau^-$), pion pairs ($\pi\pi$), kaon pairs ($K\bar{K}$), and D-meson pairs ($D\bar{D}$), among others [23]. This diversity of potential decay products enhances the opportunity for the detection and study of these elusive particles.

Axion-like particles

Axion-like particles (ALPs) are hypothetical particles that share some properties with axions, but can have a mass and couplings unrelated to the scale of the Peccei-Quinn symmetry breaking.

For instance, in various compactifications of string theory, the presence of numerous additional scalar fields is predicted, some of which can act as ALPs. These fields, often called ‘moduli’, parameterise the size and shape of the extra compactified dimensions. In many scenarios, these moduli fields possess a shift symmetry, much like the axion, and can therefore have suppressed couplings to Standard Model particles, making them phenomenologically akin to ALPs [24, 25, 26].

ALPs have a diverse range of possible couplings to Standard Model particles, which is what makes them interesting from the point of view of experimental searches. This diversity arises because, unlike axions, the properties of ALPs are not restricted by any particular theoretical framework, giving them potentially large couplings to fermions, photons, and gluons. Depending on the coupling, such ALPs may have a rich phenomenology at beam dump experiments [27, 28, 29]:

- ALPs coupling to fermions. If ALPs have significant couplings to fermions, they could be produced in decays of heavier particles. For instance, in decays of B mesons, an ALP could be emitted together with a strange meson. Another production channel is the mixing with neutral pseudoscalars. Detection of these ALPs at SHiP relies on searching for the associated decay channels, which are pairs of leptons or hadrons.
- ALPs coupling to photons. These ALPs could be most efficiently produced through the Primakoff conversion process. In this process, secondary photons copiously produced in the interactions of the proton beam with the target get converted into an ALP in the presence of the external electric or magnetic field of heavy nuclei. The reverse process can occur as well, where the ALP converts back into photons, providing the potential detection method. Hence, the main detection channel of these ALPs at the beam dump experiments is via decays into a pair of photons.
- ALPs coupling to gluons: ALPs with substantial gluonic couplings could be produced in strong interactions. The production modes are very similar to the ALPs coupled

to fermions, although having different magnitudes; the same is true for the hadronic modes. Unlike the latter, ALPs that couple to gluons do not decay into leptons; the main production channel below the $\pi\pi\gamma$ threshold is into a pair of photons.

Finding such ALPs may deliver interesting insights, given their possible connection to dark matter, as ALPs may be mediators between light dark matter particles and the Standard Model (see, e.g., [30, 31, 32]).

Millicharged particles

A generic effective model of millicharged particles (MCP) κ is $\mathcal{L}_{\text{MCP}} = \epsilon e \bar{\kappa} \gamma^\mu \kappa A'_\mu$, where e is the electron charge and $\epsilon \ll 1$. Such particles may emerge in generic extensions of the SM with an additional abelian gauge symmetry in the high-energy sector [33]. They are interesting because of several aspects. Firstly, their existence would mean the breakdown of the electric charge quantisation and may give hints about the properties of the UV completions of the SM. Secondly, MCPs may constitute a fraction of the dark matter [34, 35].

Phenomenologically, they behave as a heavy SM fermion with a charge $Q = \epsilon e \ll e$. The main production channel depends on the κ mass. It can be three-body decays of pseudoscalar mesons $\pi^0, \eta, \eta' \rightarrow \kappa \bar{\kappa} \gamma$, two-body decays of vector mesons $\rho, \omega, \phi, J/\psi, \Upsilon \rightarrow \kappa \bar{\kappa}$, or a deep-inelastic direct production $q + \bar{q} \rightarrow \kappa + \bar{\kappa}$. The detection channel would be similar to the LDM – the scattering of κ off atomic electrons in the detector material. However, there is an important difference caused by the masslessness of the mediator in the MCP case. The differential scattering cross-section $d\sigma/dQ^2$, with Q being the momentum transfer, is highly peaked at small Q . Therefore, the smallness of ϵ may be compensated by the largeness of the cross-section. This, in particular, makes it possible to consider different strategies for MCPs. Apart from a single scattering signature with a high-energy electron (similar to the case of the LDM), one may search for a multi-scattering signature with low-energy depositions [36].

1.2 Light dark matter physics programme

The FIPs described above may be related to the dark matter of the Universe. The connection may arise via two distinct scenarios. Firstly, the FIPs may be constituting the dark matter itself, as in the case of keV-scale HNLs [14] and ultra-light axions with mass below eV [37, 38, 39, 40]. Secondly, they may be mediators [41, 31, 42] between the SM and so-called light dark matter (LDM), which in this case is made of particles with mass below the Lee-Weinberg bound [43].

Beam dump experiments are not optimal for probing the first option since the particles are too weakly coupled to be efficiently produced and subsequently decay in the detector. However, beam dump experiments can explore the second scenario by producing LDM particles in the proton-target collisions and subsequently detect their interactions in the detector.

Depending on the model, several detection signatures are possible. If the dark matter particle χ is elastic, such that the FIP mediator couples to the bilinear combination $\chi\chi$, the main signature is scattering of the produced χ off the atomic electrons or nucleons in the detector material, $\chi + \text{detector} \rightarrow \chi + X$. The scattering may be elastic or inelastic, depending on the mass of the mediator and the energy of the χ . For the scattering off

electrons, the main background at SHiP comes from the scattering of neutrinos. This may be significantly reduced by imposing specific selection cuts, see Section 4.3 and Ref. [44].

Another phenomenologically distinct possibility is when the dark matter is inelastic, i.e. when the mediator couples to $\chi'\chi$, where χ' is an unstable particle. Models of inelastic dark matter do not have constraints from direct detection experiments that probe scattering signatures of galactic dark matter. Apart from the pure scattering signature, there are signatures involving multiple interactions. The χ scattering inside the detector, $\chi + \text{detector} \rightarrow \chi' + X$, produces the heavier χ' , which may itself decay within the detector. The combined event looks like a “double bang”, where the first “bang” occurs due to the χ scattering and the second one due to the χ' decay [45].

1.3 Neutrino physics programme

The high intensity and high energy proton beam at BDF produces a high intensity neutrino flux of all flavours: electron, muon and tau neutrinos, and the corresponding antineutrinos.

The presence of a hadron absorber and a muon shield that clear the forward region from hadrons and muons makes the SHiP experiment ideally suited to perform neutrino physics studies. A compact detector, located immediately downstream of the muon shield, and incorporating nuclear emulsion technology and a muon spectrometer, allows the detection of all neutrino flavours and measurement of their energy. This enables SHiP to perform tau neutrino studies with unprecedented statistics, observing for the first time the tau antineutrino in the muonic decay channel of the tau lepton, as well as measuring the relevant kinematical variables of the deep inelastic scattering (DIS) processes for both the charged and neutral current (CC and NC) interactions for all neutrino flavours.

Tau neutrino physics

The tau neutrino is the least known particle in the Standard Model. Four candidates were first reported in 2001 by the DONUT experiment [46] and the observation of this particle was finally confirmed in 2008 when nine candidate events were reported with an estimated background of 1.5 [47]. In the same paper they reported, for the first time, the tau neutrino cross-section where the constant term was measured to be

$$\sigma_{\nu_\tau}^{\text{const}} = (0.39 \pm 0.13 \pm 0.13) \times 10^{-38} \text{cm}^2 \text{GeV}^{-1}$$

The large uncertainty is due to the poor statistical sample and to the rather scarce knowledge of the incoming flux. On top of the large uncertainty, DONUT could not separate tau neutrinos from tau antineutrinos. Later, the OPERA experiment [48] detected ten tau neutrinos [49, 50, 51, 52, 53], discovering the tau neutrino appearance from muon neutrino oscillations. The only leptonic decay observed by OPERA [50] shows negative charge as expected from a ν_τ interaction. Therefore, so far there is no direct evidence for tau antineutrinos.

DIS structure functions

The large sample of neutrino events possible with SHiP provides an opportunity to make new measurements of the structure functions in tau neutrino and antineutrino charged-current

events. In general, with the usual DIS variables: $x = Q^2/2p \cdot q$ and $y = p \cdot q/p \cdot k$ where the momentum assignments are:

$$\nu_\tau/\bar{\nu}_\tau(k) + N \rightarrow \tau^-(k') + X$$

$$q^2 \equiv (k - k')^2 = -Q^2,$$

the tau neutrino and antineutrino charged-current cross-sections in terms of the structure functions F_1, \dots, F_5 are [54]:

$$\frac{d^2\sigma^{\nu(\bar{\nu})}}{dxdy} = \frac{G_F^2 ME_\nu}{\pi(1+Q^2/M_W^2)^2} \left((y^2x + \frac{m_\tau^2 y}{2E_\nu M})F_1 + \left[(1 - \frac{m_\tau^2}{4E_\nu^2}) - (1 + \frac{Mx}{2E_\nu}) \right] F_2 \right.$$

$$\left. \pm \left[xy(1 - \frac{y}{2}) - \frac{m_\tau^2 y}{4E_\nu M} \right] F_3 + \frac{m_\tau^2(m_\tau^2 + Q^2)}{4E_\nu^2 M^2 x} F_4 - \frac{m_\tau^2}{E_\nu M} F_5 \right),$$

where $+F_3$ applies to neutrino scattering and $-F_3$ to anti-neutrinos, M and m_τ are the nucleon and τ lepton masses respectively, E_ν is the initial neutrino energy and G_F is the Fermi constant.

The structure functions F_4 and F_5 , pointed out by Albright and Jarlskog in Ref. [54], are negligible in muon neutrino interactions because of a suppression factor depending on the square of the charged lepton mass divided by the nucleon mass times neutrino energy. Given the higher mass value of the τ lepton, F_4 and F_5 structure functions contribute, instead, to the tau neutrino cross section. At leading order, in the limit of massless quarks and target hadrons, $F_4 = 0$ and $2xF_5 = F_2$, where x is the Bjorken- x variable (Albright-Jarlskog relations). Calculations at NLO show that F_4 is about 1% of F_5 [55].

With the statistics of tau neutrino interactions collected in 15 years of SHiP, the experiment is capable of measuring both F_4 and F_5 .

Tau neutrino magnetic moment

The bounds on the neutrino magnetic moment are obtained via elastic neutrino-electron scattering, in which the scattered neutrino is not observed. The constraints coming from various experiments, including low-energy solar neutrino, depend on the initial neutrino flavour and its propagation between the source and the detector. A non-zero magnetic moment has been excluded for the muon neutrino and the electron neutrino down to $\mu_{\nu_\mu} < 6.9 \times 10^{-10} \mu_B$ [56] and to $\mu_{\nu_e} < 2.9 \times 10^{-11} \mu_B$ [56], respectively. For the ν_τ , that can be directly produced only at accelerators, the current upper limit was set by the DONUT experiment to $3.9 \times 10^{-7} \mu_B$ [57]. With thousands of tau neutrino charged-current interactions in SHiP's LDM/neutrino detector target, the experiment can improve this upper limit by an order of magnitude in a model independent way.

Neutrino-induced charm production

Charmed-hadron production in neutrino interactions was observed for the first time in 1974, with the observation of opposite sign dimuons [58]. Nowadays it is known that charmed hadrons are produced at a level of a few percent in high energy neutrino and anti-neutrino charged-current interactions whose Feynman diagrams are shown in Figure 2.

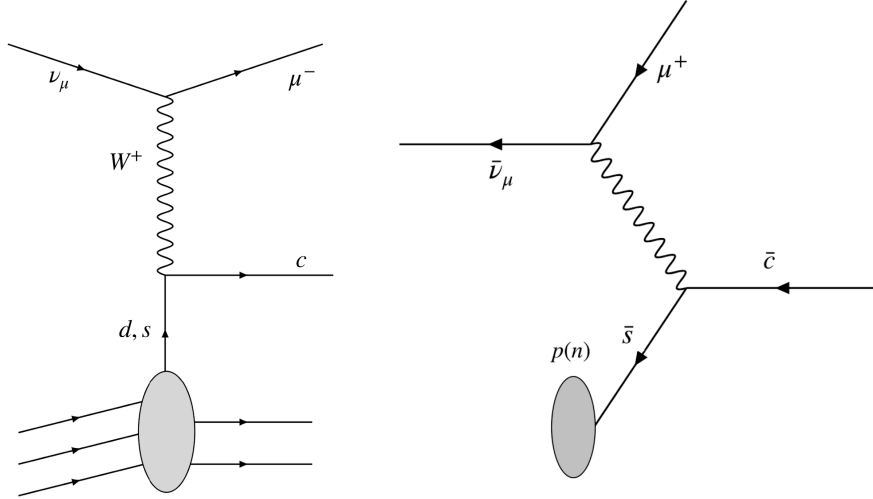


Figure 2: Left: diagram for charm production in neutrino charged-current interactions. Right: anti-charm production in antineutrino charged-current interactions.

So far, the identification of charmed hadrons produced in neutrino interactions using calorimetric techniques was only based on the dimuonic decay channel, with two opposite charged muons expected in the final state, requiring also a 5 GeV cut on the minimum momentum to reduce the background from pion decays. This has limited the available statistics to less than eight thousand charm candidates coming from muon neutrinos, and to less than two thousand charm candidates from muon antineutrinos [59]. No charm candidate from electron-neutrino interactions has been observed yet.

Parton distribution functions

The production of charmed hadrons in neutrino scattering against nucleons can occur either when the neutrino scatters off a d or an s quark. Even though the CKM coupling favours the $s \rightarrow c$ transition, this process is suppressed with respect to the $d \rightarrow c$ transition since the d -quark is a valence quark. On the contrary, in antineutrino scattering, the production of an anti-charm quark occurs through the scattering of the neutrino off a \bar{d} or a \bar{s} quark, both being sea quarks. As a result, anti-charm-production selects the anti-strange quark content of the nucleon. The fraction of $\bar{\nu}$ -induced anti-charmed hadrons coming from an $\bar{s} \rightarrow \bar{c}$ transition is above 90%.

The precise knowledge of nucleon strangeness is critical for BSM physics at the LHC and for many precision tests of the SM. Until now, the strange sea quark determination has been performed by all the PDF groups using the dimuon data collected by the NuTeV/CCFR collaboration [60]. The current status of the measurement of the proton strangeness ($s + \bar{s}$) is summarised, including uncertainty bands, in Figure 3. As shown in Figure 59 (Section 4.4), SHiP can collect large data samples of events from neutrino-induced charm production and greatly improve the measurement of the strange-quark content up to high x -values.

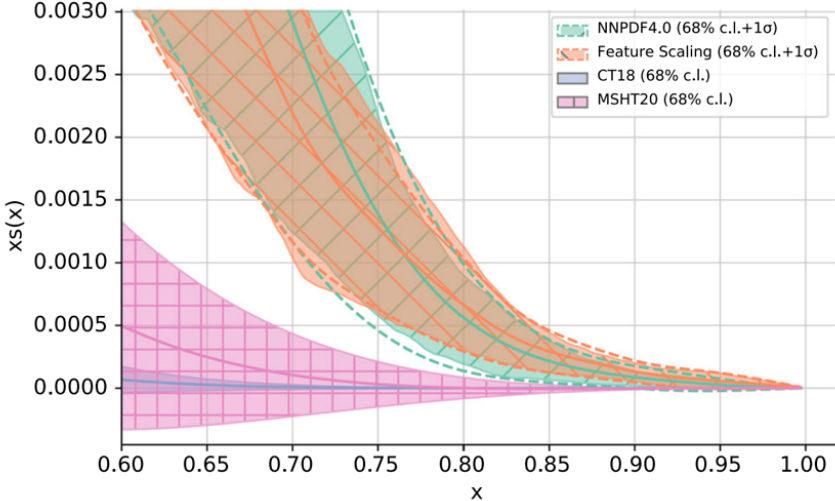


Figure 3: Current status for the $s + \bar{s}$ distribution in the proton [61].

Precision measurement of the CKM matrix element $|V_{cd}|$

Improved precision on the measurement of $|V_{cd}|$ is essential for testing the unitarity of the CKM matrix. In the past $|V_{cd}|$ was determined in two different ways, firstly from leptonic and semileptonic decays of charmed mesons [62]:

$$|V_{cd}| = 0.2173 \pm 0.0051 \pm 0.0007 \text{ (leptonic } D^+ \text{ decays)}$$

$$|V_{cd}| = 0.2330 \pm 0.0029 \pm 0.0133 \text{ (semi-leptonic } D \rightarrow \pi \ell \nu \text{ decays)}$$

using Lattice QCD calculations of the relevant decay constant and form factor.

Secondly, $|V_{cd}|$ was obtained with CC deep-inelastic scattering (DIS) of muon-(anti)-neutrinos on nucleons, using the di-muon events. Di-muon events with oppositely charged muons provide evidence of production of (anti-)charm, where charm can only be produced by d - and s -quarks and anti-charm can only be produced by anti- d/s quarks, hence involving also sea quarks in the nucleon. The main uncertainties in the extraction of $|V_{cd}|$ include the systematic error on the charm fragmentation, the theoretical uncertainty on the scale variations, and the branching fraction of charm to muon [63, 64, 65, 66]. The final result on $|V_{cd}|$ from the past neutrino DIS experiments CDHS [67], CCFR [68, 69], and CHARM II [70] is: $|V_{cd}| = 0.230 \pm 0.011$ [62].

The large neutrino DIS sample with dim-muons that can be collected with the emulsion detector of SND allows significantly reducing the $|V_{cd}|$ uncertainty from (anti-)muon DIS by tagging inclusive (anti-)charm production, and hence avoiding the dependence on the knowledge of the branching fraction of charm to leptons [65]. In addition, the branching fraction of charm to leptons can be directly measured with the SND detector, allowing in turn to reduce the corresponding systematic uncertainty in previous DIS measurements. With the high statistics samples in the SND, the sources of systematic uncertainty can also be better constrained, and advances in perturbative calculations have the potential to reduce theoretical uncertainties, such as ones from scale variations. In Ref. [65], it was estimated that such an experiment may reduce the $|V_{cd}|$ uncertainty from (anti)-muon DIS to the 2% level.

In summary, SND has the potential to significantly reduce the uncertainty on $|V_{cd}|$ from

neutrino DIS with an uncertainty competitive to or even better than the results currently achieved using leptonic charmed meson decays, which in turn allows for a more precise unitarity test of the CKM matrix in the first column.

2 BDF/SHiP at ECN3

2.1 MC simulation

The experiment optimisation and the evaluation of the expected physics performance of BDF/SHiP in ECN3 have been studied in detail with the help of the GEANT4-based Monte-Carlo framework that was developed for the original proposal. The detector responses have been tuned with the measurements done in test beams with prototypes of all subdetectors during the Comprehensive Design Study (CDS) phase. Extensive simulations of the background components were done in order to study the backgrounds generated by muon and neutrino deep inelastic scattering (DIS) in and around the detector, and by combinatorial events from residual muons leaking through the muon shield. For the implementation in ECN3, the simulation has been updated with the geometry of the underground complex and the revised muon shield and detectors. The ECN3 background evaluation and signal yields have been obtained in a rerun of the background samples through the new geometry and analysis chain.

The SHiP software framework for simulation, reconstruction, and analysis is based on the FairRoot package [71] and is called FairShip. The framework incorporates GEANT4 [72, 73] to simulate the particles through the target and the experimental setup, PYTHIA8 [74] for the primary proton fixed-target interaction, PYTHIA6 [75, 76] for muon deep-inelastic scattering and cascade production of charm and beauty [77], and GENIE [78] for interactions of neutrinos. The production and decays of various types of FIPs have been implemented in FairShip. Mainly PYTHIA8 is used to generate the different signal processes.

A total of 6.5×10^{10} protons on target (PoT) have been simulated with an energy cut of 10 GeV for transporting particles after the hadron absorber. This simulation was run with strongly enhanced muon production from QED processes, such as resonance decays and gamma conversion. For the studies of muon-induced backgrounds, the sample corresponds to 6.5×10^{12} PoT. In addition, a total of 1.8×10^9 PoT have been simulated with an energy cut of 1 GeV. Dedicated samples of charm and beauty hadrons, known to produce muons with kinematics similar to signal events, corresponding to about 10^{11} PoT have been produced. These simulation samples give sufficient statistics after the muon shield for the background determination to be extrapolated to the full run of BDF/SHiP with 6×10^{20} PoT with good statistical accuracy, and such that any known rare contribution to the muon flux is subdominant.

In order to produce a background sample of muon DIS events that is equivalent to what is expected for the full run of BDF/SHiP, the muon samples from the simulations above were used to produce DIS events with the cross-section boosted such that every muon interacts according to the material distribution of the experimental setup at ECN3.

For neutrino DIS, the neutrino spectra from the simulated minimum bias, and charm and beauty samples were used to produce a sample of neutrino interactions in the material of the detector with the help of the GENIE generator that is equivalent to seven times the full run of BDF/SHiP, again by forcing every neutrino to interact according to the material distribution of the experimental setup in ECN3.

The validity of the FairShip prediction of the particle fluxes has been verified by compar-

ing to the data from the CHARM beam-dump experiment at CERN [79]. The most realistic cross-check of FairShip has been performed in summer 2018 in a dedicated experiment at the CERN SPS [80]. It has directly measured the rate and momentum of muons produced by 400 GeV/c protons dumped on a replica of the BDF/SHiP target, and found a very good agreement at the level of 30% between the prediction by the simulation and the measured spectrum [81], which is sufficient to design the experiment.

2.2 Beam requirements and delivery

At the SPS, the optimal experimental conditions for BDF/SHiP are obtained with a proton beam energy of 400 GeV and slow extraction of the proton spills over one second, effectively 1.2 s flat top over a cycle length of 7.2 s. With the stop of the CNGS project [82] in 2013, the SPS has typically been delivering only $1 - 1.5 \times 10^{19}$ protons per year, while it is capable of delivering $> 5 \times 10^{19}$ protons. The design of the BDF is based on returning to the full exploitation of the CERN accelerator complex with the SPS at its present performance. Detailed investigations on the proton sharing in the CERN accelerator complex have been undertaken during the BDF/SHiP CDS phase [83, 84] and more recently in the studies of the feasibility of a high-intensity beam to ECN3 [85, 86]. Corresponding to an average of 200 days of operation per year and 5000 spills per day, the detailed studies confirm the possibility of delivering 10^6 spills of 4×10^{13} PoT per year, in order to annually deliver a total of 4×10^{19} PoT per year to BDF/SHiP, while satisfying the current beam requirements in the injector complex and the HL-LHC. The working point of 4×10^{19} protons per year for BDF/SHiP ensures 1.25×10^{19} protons to the other SPS beam facilities, and 0.85×10^{19} protons in case a month is dedicated to ions. It has been verified that there is no technical limitation in the accelerator complex, or in the facility design, to continue operation at 4×10^{19} protons per years for up to 15 years, guaranteeing up to 6×10^{20} PoT for BDF/SHiP.

In terms of the electrical power consumption, it was estimated that the SPS consumes about 39 MW (measured recently [87]) when operating close to the maximum RMS power, while the consumption of the rest of the injectors (PS, PSB and Linac4) is around 2 MW. The study concluded that there is no significant difference in the yearly SPS power consumption when using shared cycles for the whole North Area, as compared to dedicated BDF-like cycles for ECN3 only. Therefore, from the point of view of the accelerator, the SPS should be able to deliver the total of $\sim 5 \times 10^{19}$ protons per year at a similar power or cost as currently, approximately 150-170 GWh/year for the main magnets.

The potential capability to deliver more protons to BDF/SHiP and/or to the other beam facilities on the longer term is discussed in Section 6.1.

Figure 4 shows an overview of the North Area beam lines. The TCC8 target hall and the ECN3 experimental area are located at the end of the P42 beam line. The details of the beam delivery through the complex has been reported on by the PBC ECN3 Beam Delivery Task Force [88, 89].

For BDF/SHiP, the present T10 production target in TCC8 will be removed along with the entirety of the K12 kaon beam line. At the upstream end of TCC8, BDF/SHiP requires the installation of a set of kicker magnets along with a vacuum chamber spanning the length of TCC8 towards the BDF/SHiP proton target. The ~ 150 m drift distance is used to increase the beam size and to develop a circular beam sweep on the target's front face in order to

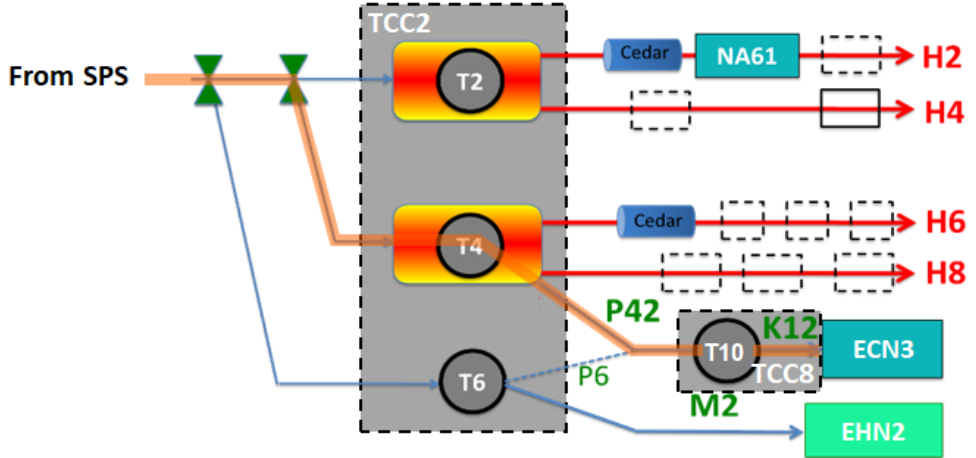


Figure 4: Overview of the North Area beam lines, targets and beam facilities.

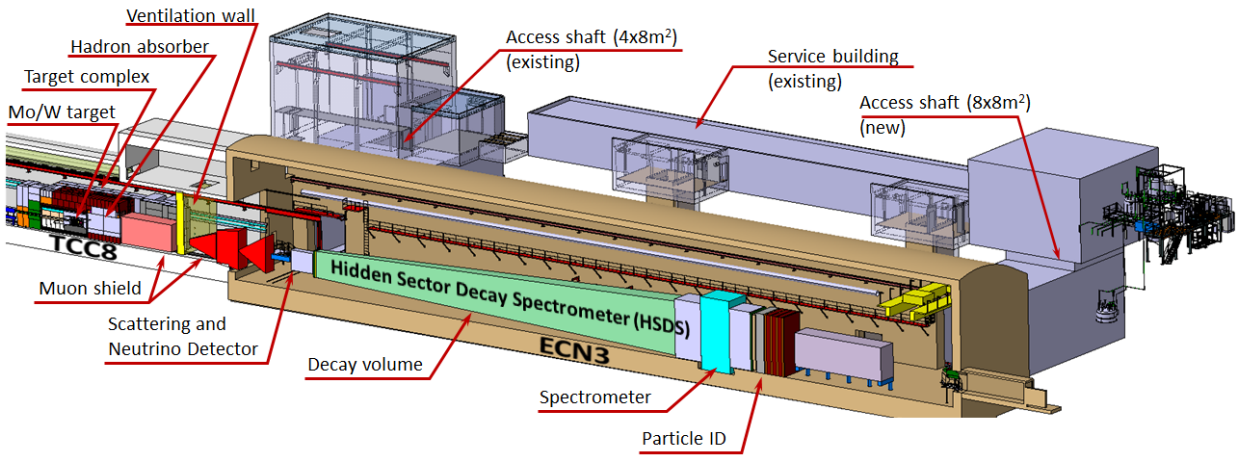


Figure 5: Overview of the BDF/SHiP experimental setup in the SPS TCC8/ECN3 experimental facility.

dilute the energy deposition. An alternative to this method is based on blowing the beam up with the help of an additional quadrupole triplet 100 m upstream of the target to produce a large beam spot of $\sigma=35$ mm on the target. Further studies aim at increasing the beam spot to >40 mm, while keeping the beam tails under control. The final choice will be made during the TDR phase.

2.3 Production target and target complex

The layout of BDF/SHiP at the end of TCC8 and throughout ECN3 is shown in Figure 5. The setup consists of the high-density proton target, effectively acting as a beam dump and absorber, followed by a hadron absorber and a magnetic muon shield immediately downstream [90, 91]. The shield deflects the muons produced in the beam dump in order to reduce the flux in the detector acceptance to an acceptable level. The hadron absorber is an integral part of the overall shielding that is completely surrounding the target system.

Together they form a compact and free-standing target complex, shown in Figure 9.

The target complex design draws from the experience gained during the CDS phase [92, 83]. With respect to the CDS design in ECN4, significant simplification and reduction in shielding is possible thanks to the use of an already operational underground area and thanks to the depth of TCC8. The handling of the target systems may be carried out by the existing crane in TCC8, taking inspiration from the recently developed design of the new SPS beam dump [93] and developments during 2023. This has led to a revision of the shielding and the system handling in ECN3 to meet the space and access constraints, while fully respecting the constraints from radiation protection, equipment maintenance and operation.

In order to maximise the production of heavy-flavoured hadrons, and photons, and at the same time provide the cleanest possible background environment by suppressing decays of pions and kaons decaying to muons and neutrinos, the target should be long and made from a combination of materials with the highest possible atomic mass and atomic number, and be optimised for maximum density with a minimum of space taken by internal cooling. The corresponding target system developed during the CDS phase [94, 95] requires no modifications with respect to the implementation in ECN3. The baseline target design is composed of blocks of titanium-zirconium-doped molybdenum alloy (TZM), cladded by a tantalum-alloy, in the core of the proton shower, followed by blocks of tantalum-cladded pure tungsten (Figure 6). The blocks are interleaved with a minimum number of 5 mm gaps for cooling, resulting in a total length of twelve nuclear interaction lengths.

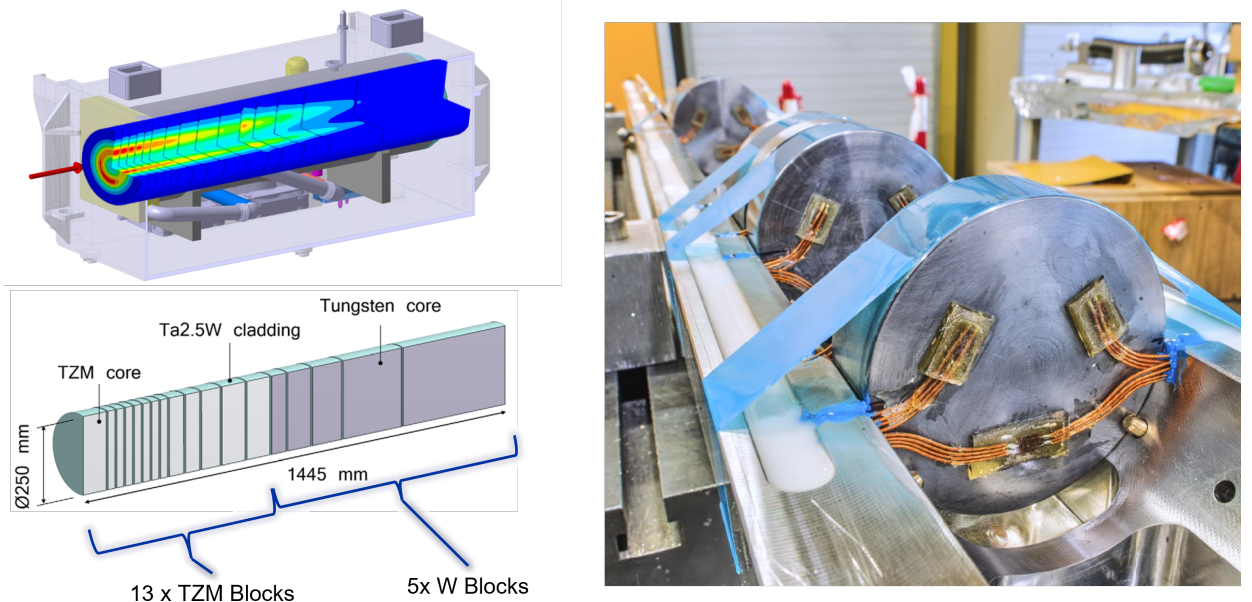


Figure 6: Views of the BDF baseline target design, with the expected temperature rise during the pulse from simulation (top left) and a cross-view of the core composition (bottom left). The photo on the right shows the instrumented prototype, prepared for the 2018 TCC2 beam test [95].

A prototype has been built in 2017 and tested with beam at the slow extraction test stand in the North Area during 2018 [95]. The beam tests allowed validation of the manufacturing route for the cladding of the target blocks [96], and provided an informative operational

experience under thermo-mechanical conditions as extreme as in the final facility. The post-irradiation examination carried out in 2022-2023 confirmed the robustness of the design, and allowed identifying the remaining quality assurance steps to be pursued in the TDR phase [97, 98]. These are mostly related with the forging of tungsten and TZM, aiming at reducing their porosity, brittleness and increasing their ultimate tensile strength.

In spite of the sound baseline design with Ta cladding, Nb-based claddings have also been investigated (Figure 7) [99, 100] with the aim of establishing an alternative solution in case the risk of Loss-of-Coolant Accident (LOCA) becomes a challenging aspect in the safe operation of the facility [101].

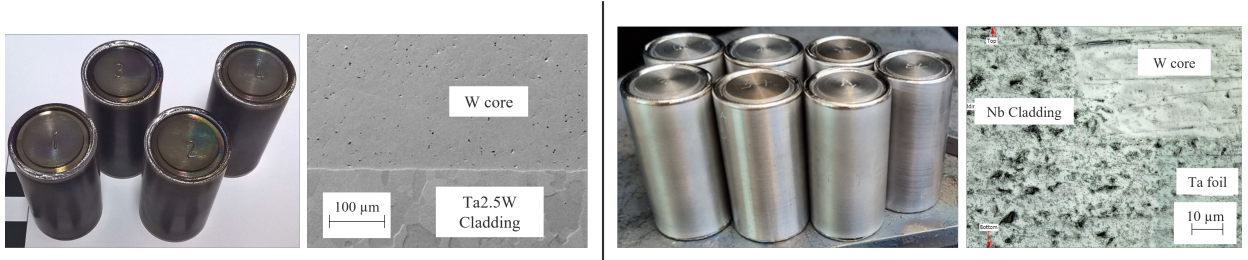


Figure 7: Hot isostatic pressing trials of Ta-alloys (left) and Nb-alloys (right) bonding on W and TZM. The images shows good bonding obtained in the different processes, resulting in the validation of the technique with these materials and providing confidence in the proposed production target design.

Moreover, an alternative target design concept is currently under evaluation, aiming at further optimising the physics performance and at having an improved design which is engineered for 4×10^{13} ppp and beyond. The idea is to remove the water gaps in-between the core materials, increasing the amount of tungsten, and by surrounding the high-A/Z core with a shroud of high-performance copper-alloy or TZM. A hot-isostatic pressed (HIP) cooling system embedded in the latter would provide optimum cooling while mitigating the risk of water contamination with spallation products. While the concept profits from the know-how gathered in the development of the PS and SPS internal dumps at CERN [102, 103], it still requires additional studies and prototyping. Collaboration with existing and future spallation user facilities, such as ISIS/STFC in the UK and the second target station at ORNL, is underway and will be further pursued in the TDR phase.

The target system has to fully absorb the 400 GeV/c, 2.6 MJ/pulse every 7.2 seconds, corresponding to roughly 350 kW of average beam power. This puts the BDF/SHiP target system in a category with technological synergies with neutron spallation sources worldwide. A bunker configuration with cooled stainless steel shielding, passive cast iron blocks (180 m^3), as well as concrete and marble shielding are foreseen, with a total volume of $\sim 360 \text{ m}^3$. A pit, 4 m long, 4 m wide and 1 m deep, will be excavated under the target station to embed part of the shielding and some of the services.

The first layer of shielding, aiming at absorbing the showers of secondary particles, consists of 400 cm of cast iron around the target vessel. Cast-embedded stainless-steel pipes for the water cooling are incorporated to extract up to 12 kW of thermal power deposited in the shielding. The target assembly and this proximity shielding is confined in a low vacuum (1×10^{-3} mbar) tank of approximately $6.2 \times 1.7 \times 2.6 \text{ m}^3$ in order to reduce air activation and

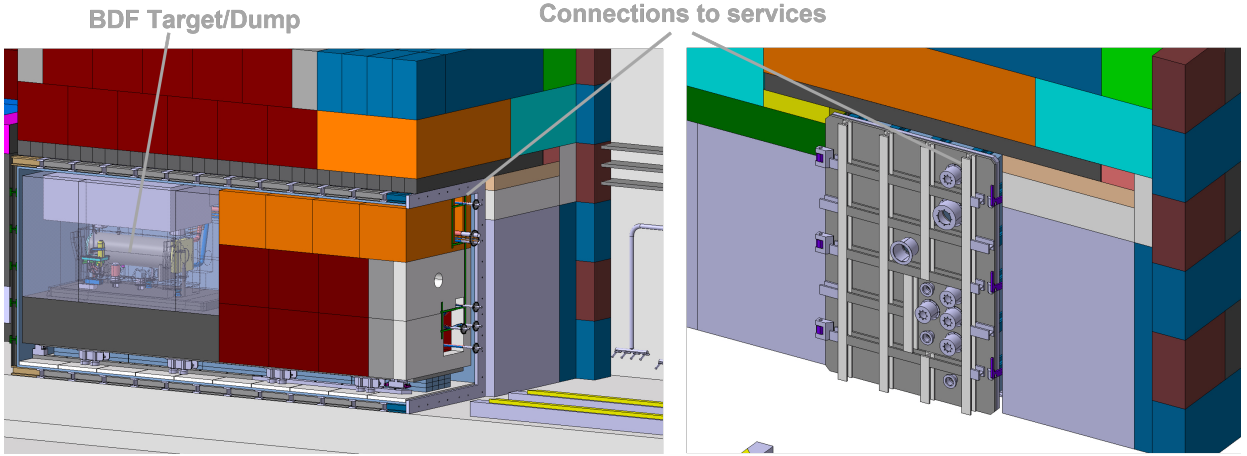


Figure 8: Target services connections upstream of the target complex vacuum vessel.

reduce radiation-accelerated corrosion due to ozone production and various other nitric acid compounds. A second assembly of cast iron and concrete blocks encapsulates the vacuum tank. The latter may be completed - in specific areas - with an outer layer of marble to reduce residual dose to workers during maintenance interventions. To ease access and limit the residual dose rate, the routing of the connections to services (vacuum, water, helium and electrical) is made upstream (Figure 8), where the beam instruments, beam window and a collimator are located [104].

For maintenance purposes, the first water-cooled shielding layer, surrounding the target, is mounted on a trolley. By opening the vacuum vessel, the trolley can be pulled upstream and the shielding extracted, facilitating access to any active component of the target system. The extraction process is carried out using the remotely controlled overhead travelling crane in TCC8.

The overall shielding design is based on CERN standard cast iron and concrete blocks. However, a particular effort is being made towards reusing already activated blocks from old facilities at CERN (CNGS target area, TT7 PS neutrino beam dump) in view of meeting CERN's sustainability goals and reducing the overall cost of the facility.

The five metres long hadron absorber stops hadrons and electromagnetic radiation emerging from the proton target. It is equipped with a coil which magnetises the iron shielding blocks [92] to serve as the first section of the active muon shield (Section 2.4). The rest of the muon shield consists of free-standing magnets. The target complex and part of the free-standing muon shield is located at the end of the TCC8 target hall, while the subsequent muon shield magnets are located in the taller ECN3 experimental hall.

A surface building with an area of 700 m^2 is foreseen to be built and connected to the existing building 911, which has the existing access shaft to TCC8/ECN3. The new service building (Figure 10), which is essential for the operation and long-term maintenance of the target complex, will host:

- cooling systems associated with the target complex;
- ventilation system for the dynamic confinement of the target complex;

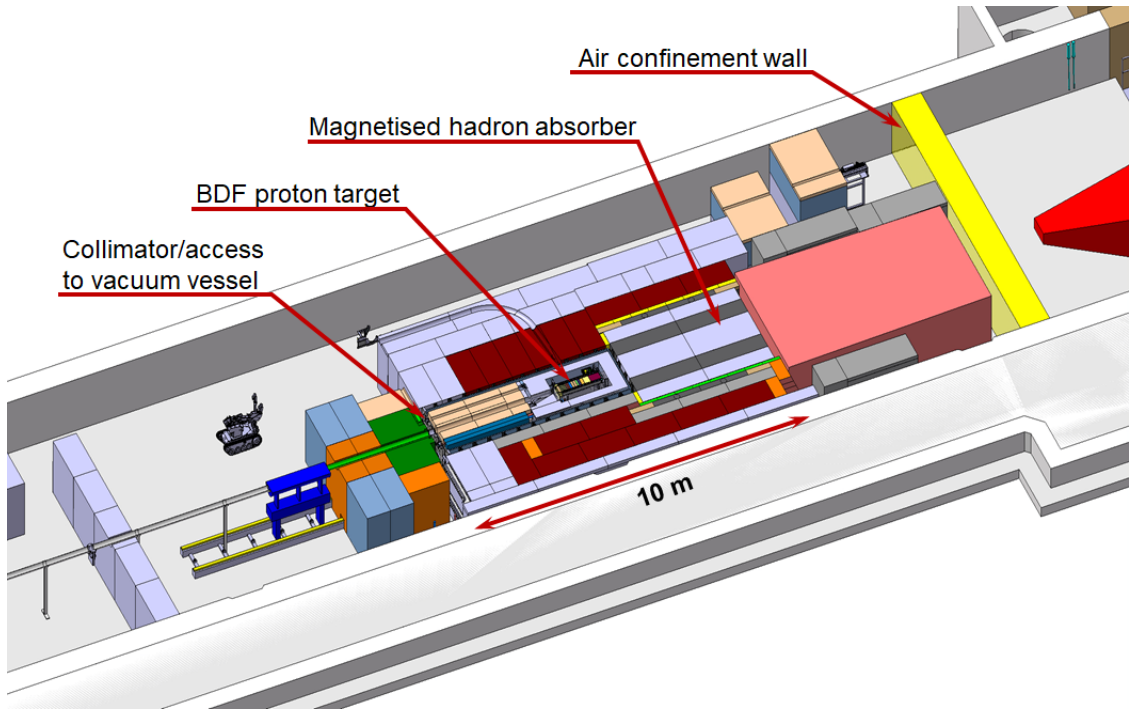


Figure 9: Preliminary design of the BDF/SHiP target systems as implemented in ECN3. The figure includes a preliminary view of the upstream vacuum beam line as well as a possible shielding configuration for the area downstream the hadron absorber.

- control racks for the hardware installed in TCC8;
- service cell for maintenance, post-irradiation examinations and preparation for final disposal of the radioactive target system components;
- buffer zone for intermediate storage prior to final removal.

In addition, an area of 200 m^2 inside the service building will be allocated to power converters required by the SHiP experiment. The associated power transformers will be located on a concrete slab outside the building.

The service cell consists of a shielded area equipped with a remotely controlled crane and a movable roof to enable transport in and out of the building of the largest equipment of the target complex. This area will be maintained under negative pressure to ensure the containment of any possible activated air/dust generated during disassembly of activated components. The aim of the service cell can be summarised as follows:

- execute repairs on defective components rather than instant replacements in order to reduce the amount of radioactive waste generated by the operation of the target complex;
- perform post-irradiation examinations to inform on the lifetime of the target complex equipment and materials along with the operation of the facility, and consequently provide inputs for new improved designs via root cause analysis;

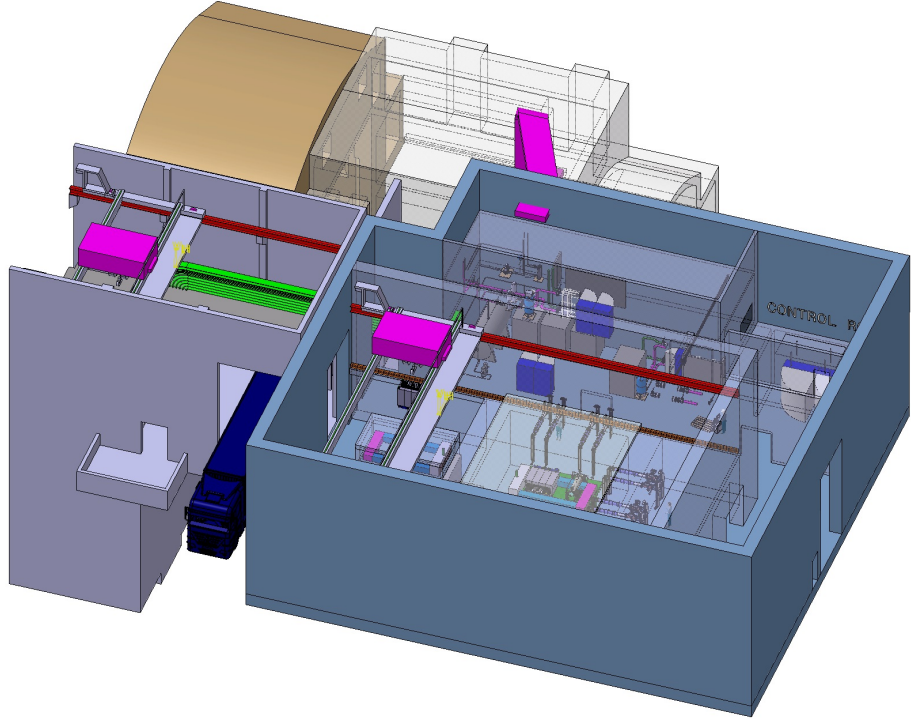


Figure 10: Preliminary 3D view of the target system service building integration.

- perform volume reduction and material separation of radioactivated material as the volume and the activation level drives the cost for the final long term disposal within the Host States;

To execute the activities, in addition to the remotely controlled crane, the service cell is equipped with a set of dedicated tools, e.g. remotely handled manipulators, and custom equipment adapted to robotic interventions.

2.4 Muon shield

The muon shield is a crucial component of the SHiP experiment. Muons are the only particles, among those that can interact strongly or electromagnetically, which emerge from the BDF target and hadron absorber in huge numbers. From simulation, about 2×10^{10} muons per spill are expected to come out of the hadron absorber with an energy larger than 10 GeV. Muons below that energy can be stopped with adequate shielding. The muon flux at the exit of the BDF/SHiP hadron absorber as a function of the muon momentum p and the transverse momentum p_T , as expected from Monte Carlo simulation, is shown in Figure 11. These muons produce excessive occupancies in the SND detector and can interact with matter and create fake signatures of FIPs decaying in the SHiP experimental setup. Random combinations of two muons in the detector can also mimic such signatures. SHiP has invested considerable effort to predict as accurately as reasonably possible the flux of muons emerging from the proton target. A large muon background sample, described in Section 2.1, is heavily used to study and optimise the design of the muon shield and establish its performance with adequate reliability.

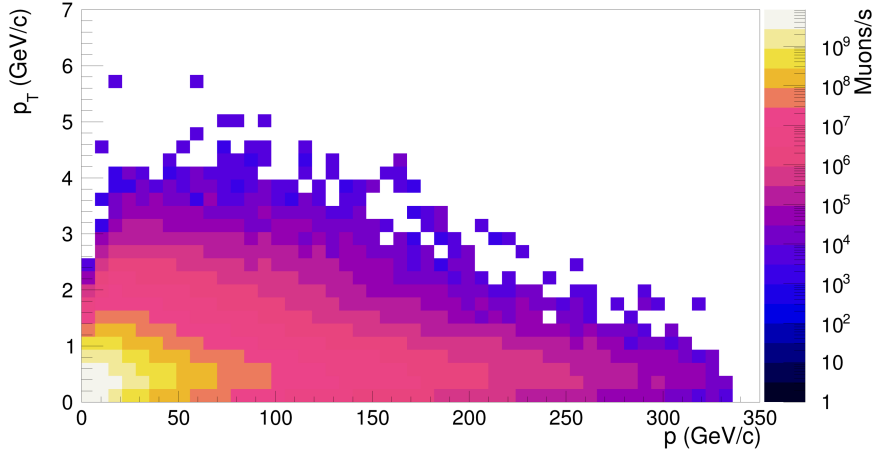


Figure 11: Expected muon flux from Monte Carlo simulation at the exit of the SHiP/BDF hadron absorber as a function of momentum p and transverse momentum p_T . Figure from [91].

The role of the muon shield is to sweep out or stop muons. An alternate-polarity scheme was proposed and developed [91] for the SHiP muon shield. The working principle of this scheme is displayed in the left graph of Figure 12. The high-energy muons are deflected by the core of the first section (with a given polarity) and continue to be deflected by the return field in the yoke of the second section (opposite polarity), while the mid-momentum muons are “refocused” by the return field of the first section onto the yoke of the second section and deflected back towards the outside. As a result, the muon shield splits the positive and negative muons emerging from the target into two prominent plumes to the left and to the right (see right graph of Figure 12) thus creating a sanctuary in the middle where the low background experiment can be implemented. The muon rate in the SHiP detector is suppressed by about six orders of magnitude.

The design of the muon shield was developed in several steps, based on the original idea of the alternate-polarity scheme with normal-conducting (NC) magnets made of grain-oriented steel (GOS) with an assumed $B = 1.7$ T field in the active medium. The design evolved from a two-magnet configuration towards a more elaborate six-magnet configuration [90, 105, 106]. A Bayesian machine-learning algorithm was developed [107] and applied. The procedure tested thousands of configurations and resulted in a set of optimised shapes with a strongly reduced iron weight for a similar muon shield performance. After the submission of the BDF/SHiP CDS report [84], time was invested to explore several other versions of the alternate-polarity scheme, still within the context of the ECN4 facility³. An alternative design was worked out, with an emphasis on engineering aspects, that uses six NC magnets made of standard iron with a conservative $B = 1.6$ T in the active medium, and making use of a tuned returned yoke [109, 110], i.e. with diluted transverse profile of the magnetic field $B_y(x)$. Another design, using two superconducting (SC) magnets of alternate polarity was also explored [111, 112, 113], assuming a conservative $B = 4$ T in the core region. These studies indicated that a reduction of the total length of the muon shield by about 9-13 m was

³A preliminary exploration with a different scheme, using a *single* unconfined field SC solenoid, is also ongoing [108].

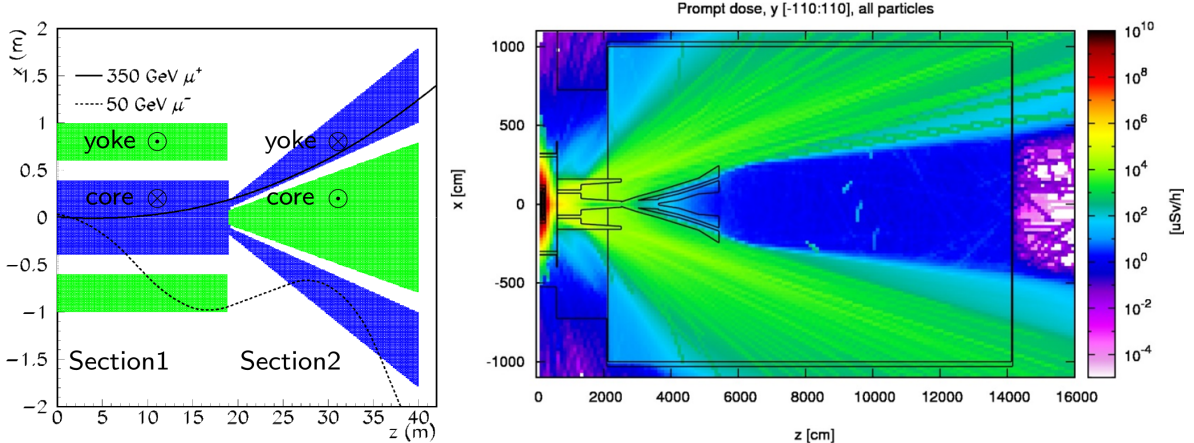


Figure 12: Principle of the alternate polarity scheme of the SHiP/BDF muon shield (see text for explanation). Left: the green/blue colors and \odot/\otimes symbols indicate the polarity of the field in the iron. Figure taken from [91] and adapted. Right: expected prompt dose (dominated by muons) at the SHiP experiment. Figure taken from [10].

possible. Both alternative muon shield designs achieved satisfactory performance in terms of muon rates in the detector, which illustrates the inherent robustness and versatility of the alternate-polarity scheme.

For SC magnets, exposure to high-energy particle showers must be limited, since a small and local energy deposition may provoke a quench. For LHC-type magnets at 7 TeV beam energy, depending on magnet location and magnet type, quenches are expected at energy deposition levels in the range of a few to a hundred mJ/cm^3 for losses occurring within $\sim 10 \mu\text{s}$ to 1 s [114]. The energy deposition in a magnet located just behind the hadron absorber of BDF/SHiP was studied by the CERN SY-STI-BMI group⁴. Figure 13 shows the preliminary result of their FLUKA simulation. The amount of energy deposited is well below standard quench limits for LHC-type magnets, which leaves room for further optimisation (reduction) of the length of the hadron absorber and distance of the SC magnet from the end of the proton target.

The proposal to implement the BDF/SHiP experiment in the existing ECN3 facility [86] called for further studies to adapt the experimental layout to this new context. For the muon shield, the main differences arising from an implementation in ECN3, when compared to ECN4, are

- constraint in available space (height and width) for part of the muon shield which must sit inside the existing TCC8 cavern;
- shortening of the distance between target and experiment in order to fit the decay volume and detector inside the ECN3 cavern without substantial loss of physics reach and create more space around and at the end of the experiment.

⁴See presentation by G. Mazzola in 24th SHiP collaboration week, 8-9 March 2023, CERN, at <https://indico.cern.ch/event/1256534>

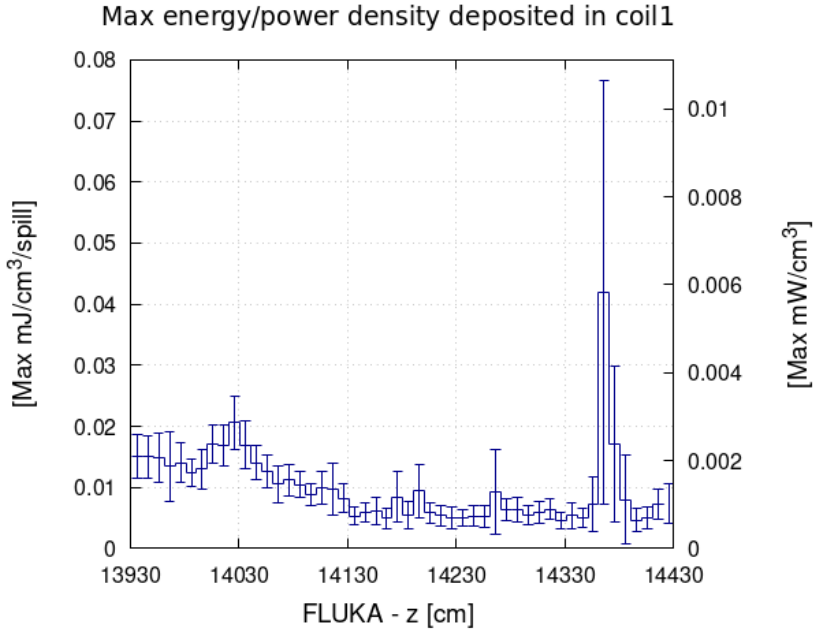


Figure 13: Expected deposited energy obtained with the FLUKA simulation and a model of a SC magnet located immediately behind the hadron absorber for 1 s spills every 7.2 s and $4 \times 10^{13} p/\text{spill}$. In the FLUKA model, the SC magnet starts at $z = 13930 \text{ cm}$.

In the first step, to obtain a prompt result, the GOS six-magnet scheme was manually modified, by simply shortening section 2 by about 5 m. The muon shield performance resulted in an acceptable increase by a factor three of the muon rate in the SST. This increase was mostly due to sub-optimal performance to re-deflect muons that have been swept out and bent back in section 1 towards the detector. Such result was expected, since the section 2 was only shortened, and not re-optimised. The result was already presented in the BDF/SHiP@ECN3 LoI [86] and is not further discussed here.

In the second step, configurations with SC magnets were studied with the scope of shortening the muon shield by exploiting the stronger bending power achievable with SC magnets, compared to NC magnets. Given the adaptation necessary to implement BDF/SHiP in ECN3, the shorter muon shield implies that the reduced dimension of the SHiP detector, i.e. smaller vacuum vessel and detectors, can be implemented while preserving the physics reach. In addition, it also frees up space behind SHiP to install possible future complementary detectors (see Section 6.3). The potential benefits are attractive enough to motivate such exploratory studies, although usage of the NC muon shield remains a valid option. Since section 2 of the muon shield acts mainly through its return yoke field, while the role of its core region is principally to collect the magnetic flux and *not* to sweep out muon trajectories, for this section the benefits of SC technology do not easily outweigh the disadvantages due to complexity (and, possibly, construction cost). Therefore, it was decided to focus explorations for ECN3 on a hybrid SC/NC scheme, i.e. a SC section 1 followed by a NC section 2.

A Bayesian machine-learning optimisation campaign was launched with a parametrised single SC magnet in section 1 followed by three parametrised NC magnets with the opposite

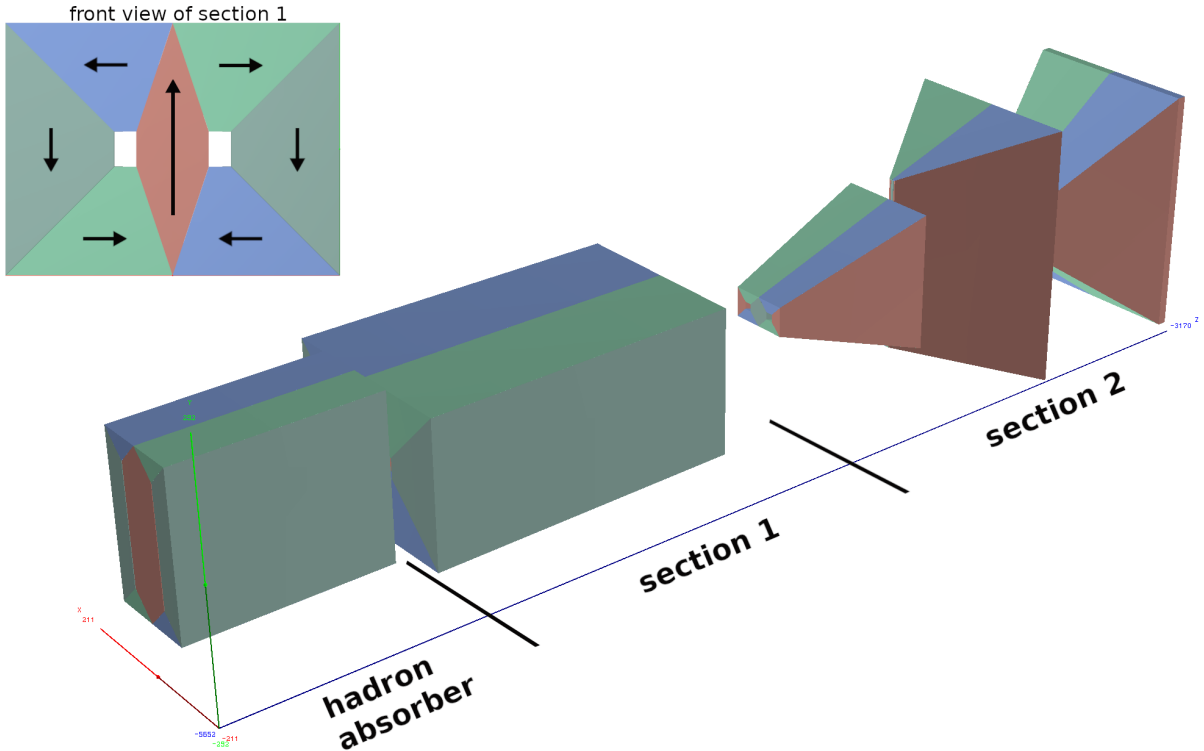


Figure 14: Geometry of the hybrid SC/NC muon shield configuration as used in the FairShip Monte Carlo for the background simulation studies. The top left insert (front view of section 1) explains the color code of the magnetic field orientation. The leftmost element of the muon shield depicts the magnetised hadron absorber, the second element is the SC magnet of section 1, the last three elements are the opposite polarity NC magnets of section 2.

polarity. The section 1 magnet contains an iron core, two voids on its sides for the SC coils and an iron yoke all around. For the optimisation, the magnetic fields are treated in a simplified manner, since a full finite-element model calculation per configuration is not available at run time. Verification with a realistic field map is then carried out for the selected configurations. The magnets are composed of seven iron volumes, each having a field with a fixed orientation and constant amplitude (see Figure 14). All iron volumes have a constant field set to 1.7 T, except for the core volume of the SC magnet which has a fixed vertical field of 5.1 T.

In the SC magnet the yoke has a thickness three times larger than half the width of the core in order to support the assumption of flux confinement. With such constraint, the simplified fields have been shown to be a valid approximation for the purpose of these studies. The coil spaces are such that a current density of less than 50 A/mm² is possible⁵.

The automated search found several configurations with a performance (muon track rates in the HSDS main tracker ~ 20 kHz) on par with or even better than the GOS six-magnet configuration for ECN4, while being about 10 m shorter along the beam axis. Among these

⁵The conservative dimensions and field values used for this preliminary studies were chosen such as to allow using robust SC cables, such as those used for the ATLAS [115] and CMS [116] experimental magnets.

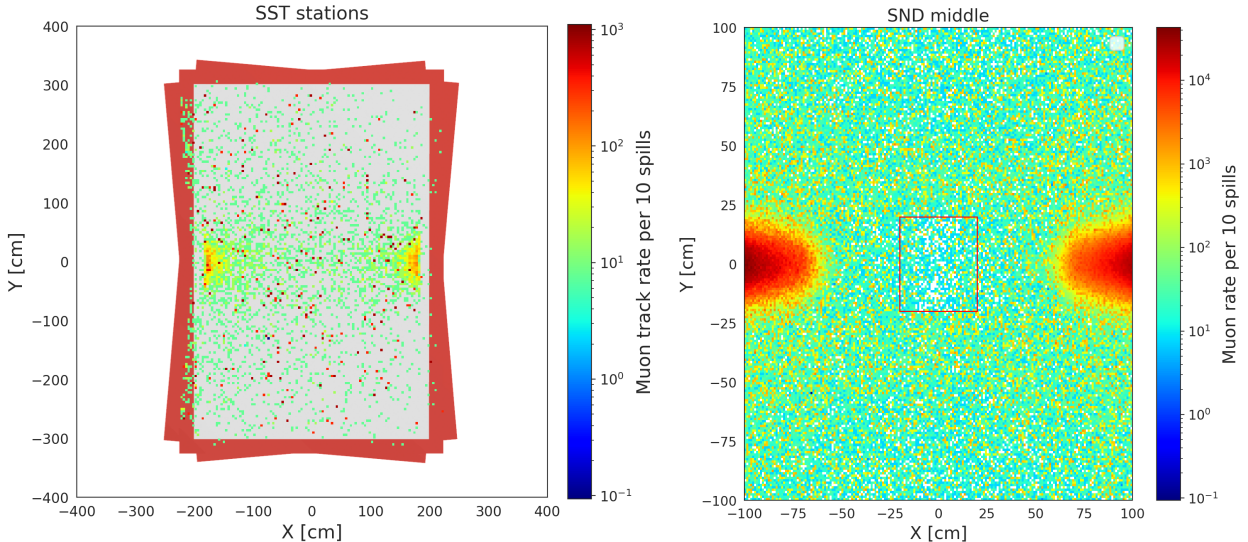


Figure 15: Typical muon hit maps in the SST (left) and SND (right) obtained from muon background simulation with the chosen hybrid SC/NC muon shield configuration, see text. The hit rates correspond to 10 s (10 proton spills). Left: Rate of muons per bin of $4 \times 4 \text{ cm}^2$ seen by the HDS main tracker; the red bands show the frames of the four views of a station. Right: Rate of muons per bin of $1 \times 1 \text{ cm}^2$ that cross a vertical scoring plane at a z position corresponding to the middle of the SND; the red rectangle shows the SND acceptance.

solutions, one was chosen which exhibit reasonably low muon rate in the SND acceptance ($\sim 4 \text{ Hz/cm}^2$)⁶. In this configuration, of which an overview is shown in Figure 14, the assumed 5.1 T core field of section 1 extends over a width of approximately 0.9 m and a length of 7 m along the beam. The coil space extends by 0.44 m in height and has a minimal width of 0.17 m. Without optimising the yoke dimensions, the total iron weight of the SC magnet is in the order of ~ 500 tonnes. Its stored energy is estimated to be $E_{\text{stored}} \approx 30 \text{ MJ}$ (for comparison, a 14.3 m long LHC dipole has an $E_{\text{stored}} \approx 7 \text{ MJ}$). The second section is composed of NC magnets, as depicted in Figure 14. This configuration was used to launch the intensive background simulation studies presented in Section 4, but it is important to note that studies are still ongoing which could further improve the design.

More studies are carried out in parallel to the Bayesian optimisation campaign in order to assess the impact of the assumed core field in section 1 and the possibility to separate the yoke from the coil and core, by inserting a gap all around, such that a reduced cold mass can be achieved. The simulation results also show that a gap of 20 cm all around the core and coil does not notably degrade the performance of the muon shield, and in some cases even improves it. This gives flexibility for the engineering design, as one could consider options with a fully-enclosing cryostat, including the yoke, or with a smaller cryostat embedded inside the yoke. The studies also show that the yoke dimensions, and therefore the yoke weight and cost, can be reduced substantially by accepting stray field without affecting the

⁶The current optimisation is not specifically including the SND muon rates in the optimisation cost function. It is expected that $\mathcal{O}(1) \text{ Hz/cm}^2$ can be achieved.

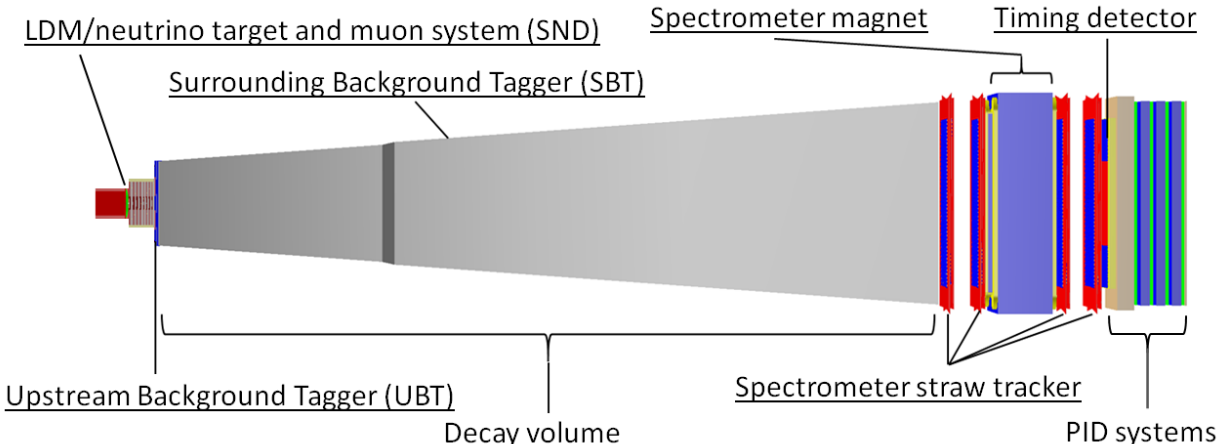


Figure 16: Overview of the SHiP Scattering and Neutrino Detector (SND) and Hidden Sector Decay Spectrometer (HSDS).

muon shield performance. Further optimisation studies will be pursued that include more flexibility in the transverse profile (x) of both the material distribution and the vertical magnetic field amplitude. This refinement invokes the use of more realistic field maps based on finite-element model calculations to properly take into account yoke iron saturation and stray fields. Finally, preliminary explorations also show that filling the core volume of the SC magnet with stopping and/or ferromagnetic material is not critical and can be decided at a later stage, during the engineering design phase.

Further considerations, beyond the physics performance, will have to be addressed, such as the availability of SC cable⁷, cost and time for development of a SC magnet, electricity consumption, which may also influence the decision to use a hybrid SC/NC muon shield or a full NC muon shield.

2.5 Overview of the SHiP detector

The SHiP experiment is composed of a dual system of complementary apparatuses, shown in Figure 16. The upstream system, the Scattering and Neutrino Detector (SND), is designed to search for LDM scattering and perform measurements in neutrino physics. The downstream system, the Hidden Sector Decay Search (HSDS) detector is designed to reconstruct the decay vertices of FIPs, measuring invariant mass and providing particle identification of the decay products in a background-free environment.

An overview of the concepts of the two detector systems is given below. Section 3 covers in detail the requirements and status of each subsystem, together with information about the development history and outlook on the main points to be addressed during the Technical Design Report (TDR) phase. More information on the detector, the design and the detector performance from measurements with prototypes in test beam have been reported in Refs. [10, 117, 84, 12]

⁷See presentation by M. Mentink and B. Cure in EP R&D Day 2023-1, 20 February 2023, CERN, at <https://indico.cern.ch/event/1233482/>

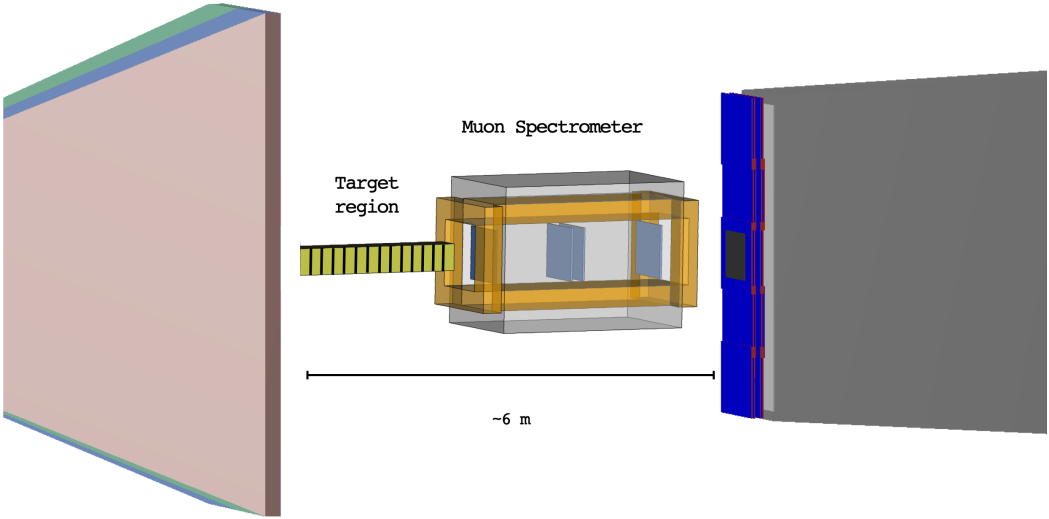


Figure 17: Schematic layout of the Scattering and Neutrino Detector (SND).

With the muon shield for ECN3 based on a hybrid superconducting/normal conducting magnet system, the SND detector is located at about 27 m and the HDS detector at about 33.5 m from the centre of the target (10.5 m and 13.5 m closer, respectively, than in the CDS design). The shorter distance between the target and the detectors allows adapting the overall footprint of the SND and the aperture of the HDS spectrometer to ECN3, while still preserving the signal acceptances for all physics modes, production and scattering/decay kinematics convolved together ([86] and Section 4). The new SND configuration occupies about 6 m in length, and the aperture of the HDS detector is reduced from the original 5 m width and 10 m height to $4 \times 6 \text{ m}^2$, consequently reducing also the decay volume and the particle identification systems in height and width. The lengths of the decay volume and the HDS spectrometer remain unchanged.

2.5.1 Scattering and Neutrino Detector

The Scattering and Neutrino Detector (SND) is located immediately downstream of the muon shield. Figure 17 shows the configuration of the SND, as implemented in the simulation. It consists of a LDM/neutrino target region followed by a muon spectrometer. The lateral detector size is driven by the profile of the area in the transverse plane which is cleared from the bulk of the muon flux (see Figure 15(right)). The neutrino flux and neutrino energy decreases with larger polar angles. This produces a strong radial dependence of the neutrino interaction yield, favouring the development of a narrow and long LDM/neutrino target.

The LDM/neutrino target is instrumented with vertexing capability in the form of emulsion films and fast electronic tracker planes alternated with tungsten plates. The configuration allows reconstructing the shower produced by the recoil electron or nuclei in LDM scattering. In addition, the micro-metric accuracy of the nuclear emulsion provides crucial topological discrimination of LDM interactions against neutrino-induced background events. For the neutrino physics programme, the emulsion technique allows detecting tau leptons and charmed hadrons by disentangling their production and decay vertices with the help of the

sub-micrometric position and milliradian angular resolution. The tracker planes within the target also provide accurate measurement of time, and together with the emulsion, the system also measures electromagnetic and hadronic energy in neutrino interactions. The SND muon spectrometer is designed to identify and measure the charge and momenta of muons produced in $\nu_\mu/\bar{\nu}_\mu$ and in $\nu_\tau/\bar{\nu}_\tau$ interactions. The momentum of charged pions and kaons are measured through the detection of their multiple-Coulomb scattering in the target [165].

2.5.2 Hidden Sector Decay Spectrometer

The HSDS measures both fully reconstructable decays of FIPs as well as partially reconstructable decays with neutrinos in the final state in a 50 m long decay volume of a pyramidal frustum shape. The decay volume is followed by a large spectrometer. The main element of the spectrometer is the tracker, designed to accurately reconstruct the decay vertex, the mass, and the impact parameter of the reconstructed FIP trajectory at the proton target. A particle identification system, including an electromagnetic calorimeter and a hadronic calorimeter, provide particle identification, which is essential in discriminating between the very wide range of models with FIPs, but also in providing information for background rejection. The electromagnetic calorimeter is designed to provide electron/hadron discrimination and precisely measure the electromagnetic shower axes, allowing reconstructing the vertex and the invariant mass in $\text{ALP} \rightarrow \gamma\gamma$ decays.

The key feature of the HSDS detector design is to ensure efficient control and suppression of the different backgrounds. Background from neutrinos interacting within the decay volume is eliminated by maintaining the decay volume under vacuum. The decay volume wall is instrumented upstream and on the sides by a system of high-efficiency background taggers in order to provide veto with spatial and time information against muon and neutrino interactions in the vessel walls and against particles entering the volume from outside, including cosmic particles. A dedicated timing detector is located between the last spectrometer tracker plane and the particle identification system to provide a measure of time coincidence in order to suppress combinatorial backgrounds.

The new muon shield and the new detector geometry, as well as the complete geometry of the implementation in ECN3 have been fully implemented in SHiP’s GEANT-based simulation framework (FairShip) to reevaluate the backgrounds and verify the signal yields.

2.6 Integration and civil engineering

The updated configurations and dimensions of the target complex, muon shield, both in the option with only NC magnets and in the SC/NC hybrid option, and the updated dimensions of the detectors, allow integrating BDF/SHiP in the TCC8/ECN3 with only limited modifications to the existing infrastructure. A preliminary integration and civil engineering study [118] of the required modifications has been carried out. The civil engineering foreseen, as well as the additional infrastructure and service buildings needed on site, have been included in the costing of the facility [119].

In the baseline integration model, the target is located 22 m upstream of the opening between the TCC8 target hall and the ECN3 experimental hall, at a height of 170 cm with respect to the TCC8 floor. This leaves 148 m between the entrance of the TCC8 hall and

the target. Apart from the beam line components (Section 2.2) required to generate the sweep/blow-up for the beam energy dilution on the target, the line up to the target consists of a beam vacuum chamber, equipped with beam instrumentation.

The entire target complex, shown in Figure 9, occupies a floor space of $7.8 \times 11 \text{ m}^2$, leaving a $\sim 2 \text{ m}$ wide passage for personnel and small material along the Jura side wall of TCC8. The complex fits below the existing bridge crane in TCC8. Dedicated fire resistant walls, constructed on both sides, upstream and downstream, separate the target area from the upstream underground complex and from the ECN3 cavern, and ensure confinement of the air volume around the target complex. Under the current assumptions related to radiation protection (Section 2.7), about a metre of additional iron shielding is required below the target complex to guarantee that soil activation remains below acceptable limits. To this end, a 4 m long, 4 m wide and 1 m deep pit will be excavated into the existing floor to embed the shielding, as well as some of the services associated with the target system. The strict soil activation limits currently applied are defined by the limited knowledge of the hydro-geological situation below TCC8/ECN3. A detailed hydrological study is underway that may allow relaxing the limits and reducing the requirement on the shielding pit⁸.

Downstream of the target complex, the muon shield and the detector components are positioned as in Figure 18. The downstream air confinement wall for the target complex is located in the space between the muon shield magnets.

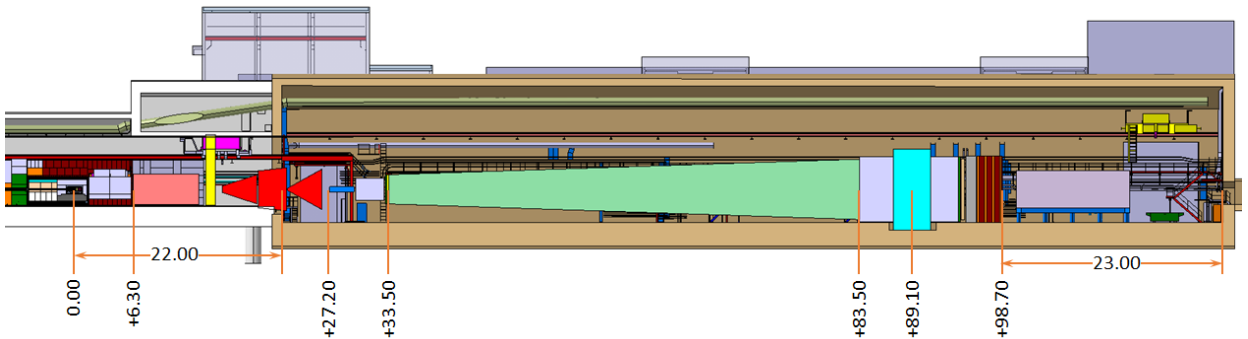


Figure 18: Space reservation and location of the SHiP detector components with respect to the centre of the proton target.

The SHiP detector is entirely housed in ECN3, leaving 23 m of free space up to the end wall of the cavern⁹. With the exception of the SHiP HSDS spectrometer magnet, the muon shield and the detector components are located on the current TCC8 and ECN3 floors. The entire detector fits below the existing bridge crane in ECN3. Limited excavation of the ECN3 floor is necessary under the spectrometer magnet to host the yoke, corresponding to a pit of $5 \times 7 \text{ m}^2$ and a depth of one metre (Figure 19). The pit is not interfering with the existing water drainage system or other existing service ducts.

While the distance between the Salève-side wall and the decay volume in ECN3 is between $\sim 4 - 2 \text{ m}$ (upstream/downstream), the Jura-side wall is at distance of $\sim 9 - 7 \text{ m}$, allowing space for detector construction and maintenance.

⁸Potential saving of up to 250 kCHF of civil engineering works.

⁹Future extension of BDF/SHiP using this space is under study (Section 6.3).

On the surface of the ECN3 site, an auxiliary service building of 700 m^2 will be constructed adjacent to the existing access building 911 to house power converters and the services needed for the target complex. The local electrical installation requires the construction of a concrete platform measuring about $12 \times 4\text{ m}^2$ to support the transformers.

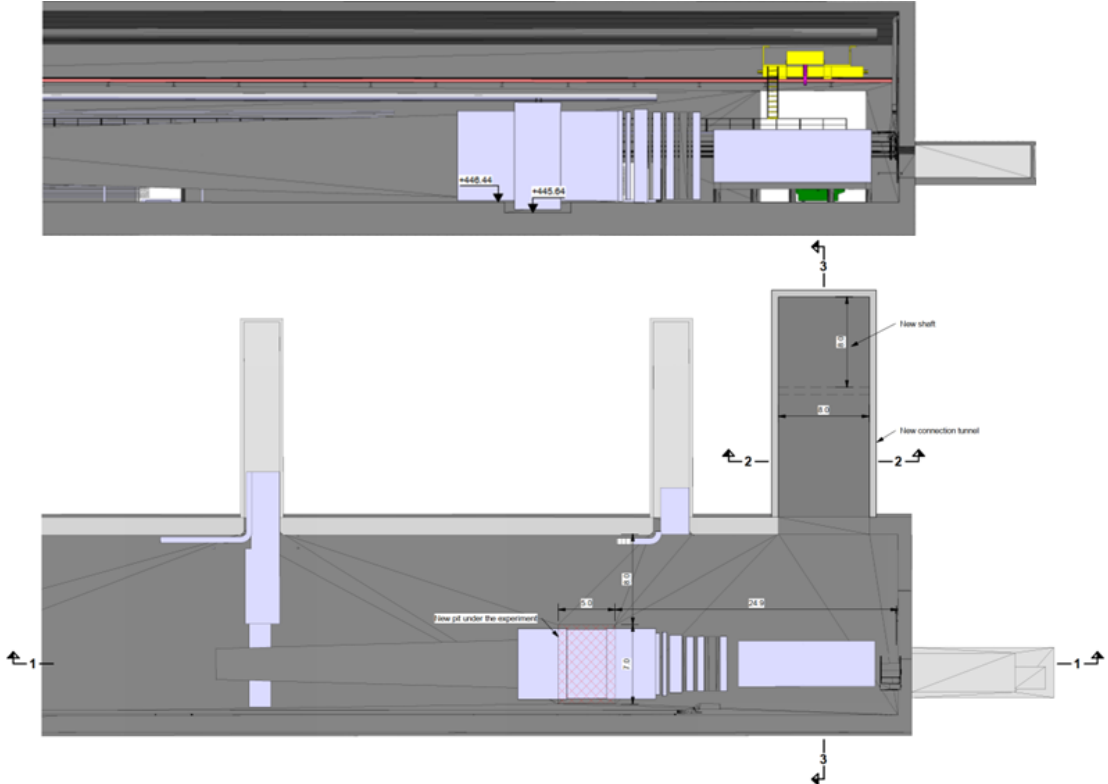


Figure 19: Views of the ECN3 cavern with the proposed floor excavation for the SHiP spectrometer magnet (red hatched area).

The current access shaft to TCC8/ECN3 of $4 \times 8\text{ m}^2$ in building 911 is considered a limiting factor in performing the decommissioning and installation works associated with both TCC8 and ECN3. An additional equipment shaft of $8 \times 8\text{ m}^2$ at the end of ECN3, shown in Figure 20 and in 21, allows separating the activities associated with TCC8 and the target complex, and the detector activities in ECN3. It reduces interference and significantly ease and simplify the detector installation. To allow the construction of the new shaft and the connecting tunnel to the ECN3 cavern, the existing detector-service building 918 will be shortened by $\sim 20\text{ m}$ and related services will be rerouted. A new access building will be constructed on top of the new shaft, equipped with only a crane for equipment handling. The remaining detector-service building appears sufficient to host detector electronics and computing, and space for operating the detector.

2.7 Radiation protection

The implementation of BDF/SHiP in ECN3 has undergone a series of exhaustive radiation protection studies [120] with the use of FLUKA Monte Carlo code [121, 122]. These studies

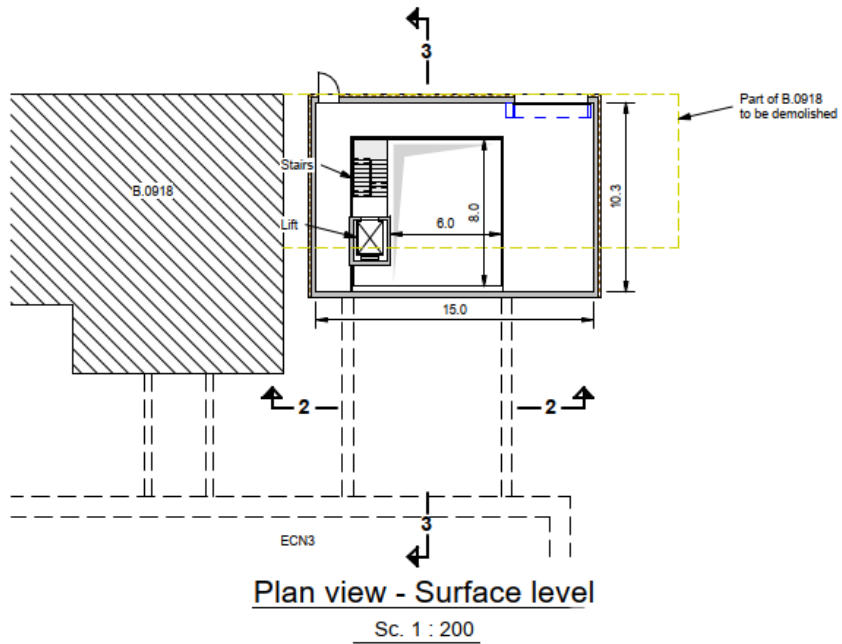


Figure 20: Proposed layout (top view) of the new shaft and access building with connection to the existing cavern.

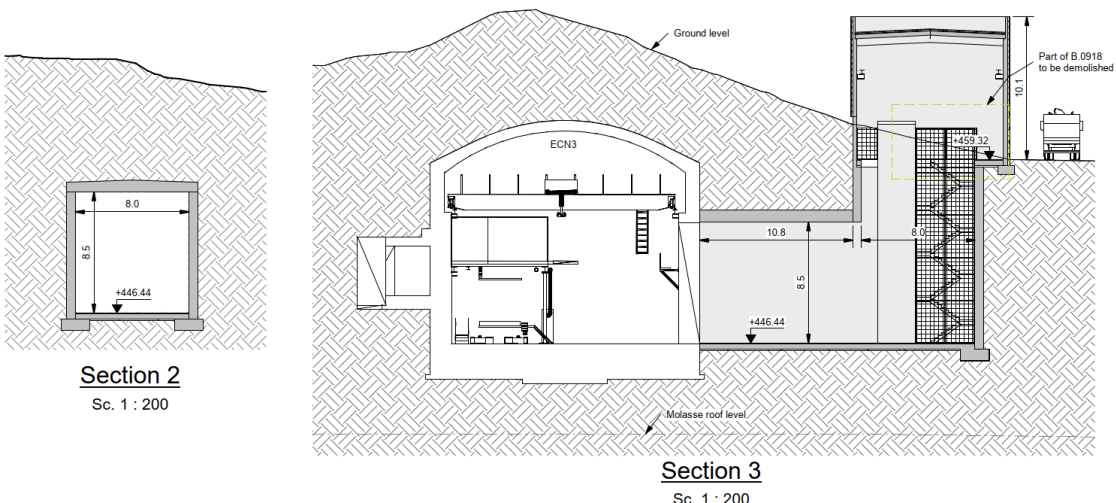


Figure 21: Section through the existing ECN3 cavern and the proposed new connecting tunnel and equipment shaft

have been aimed at optimising the implementation in TCC8 and ECN3 to ensure that the exposure to radiation of personnel and members of the public, as well as the radiological impact on the environment, would be compliant with CERN’s RP code [123] and as low as reasonably achievable (ALARA).

The optimisation takes into account the prompt and residual radiation, soil activation, air/He activation and the environmental impact. Compared to the original CDS design, it has been possible to significantly reduce the amount of shielding at strategic locations by

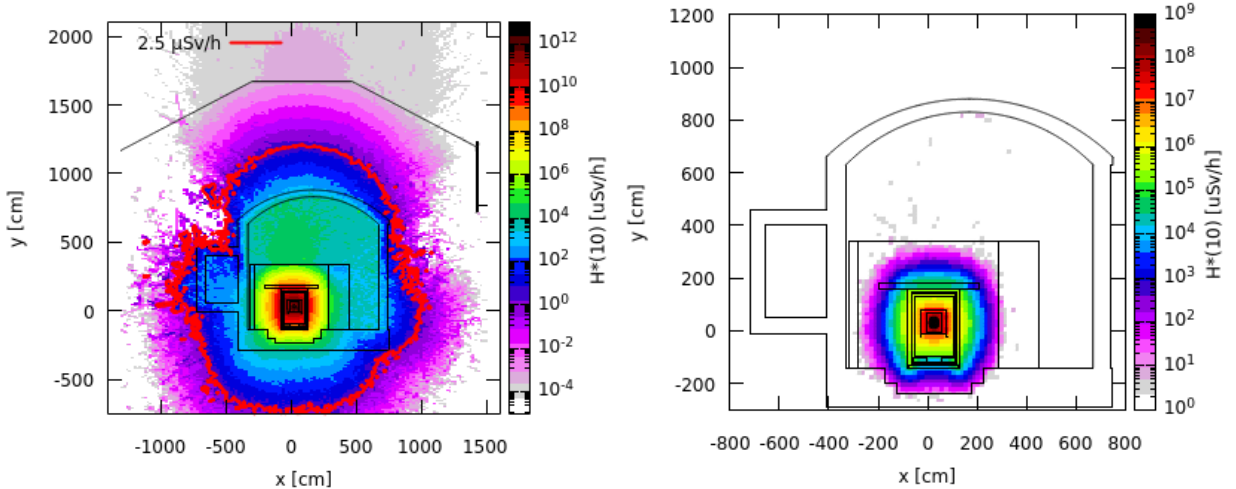


Figure 22: Left: prompt ambient dose equivalent $H^*(10)$ rate considering nominal BDF operation. Right: residual ambient dose equivalent rate $H^*(10)$ after 15 years of irradiation and one month of cool-down. Values represented in the xy plane are averaged in z around the target, which is the most critical area.

benefiting from the substantial soil layer above TCC8 and ECN3 and downstream of it, as well as the already existing activated shielding from the TCC8 target area. Consequently, decommissioning of the facility will also involve less newly produced radioactive waste.

Studies of prompt radiation above the target complex and beyond demonstrate that the ambient dose equivalent rates are far below the limit of a low-occupancy Non-designated Area (Figure 22), which amounts to $2.5 \mu\text{Sv}/\text{h}$. Considering nominal BDF operation with 4×10^{13} proton/cycle and a cycle length of 7.2s, the dose rate in the most critical area that is above the target station, is expected to be in the order of $1 \times 10^{-3} \mu\text{Sv}/\text{h}$ and is thus well optimised.

Furthermore, the annual doses due to stray radiation at the CERN fence downstream of ECN3 and beyond have been investigated. The results, presented in Figure 23, show that the ambient dose equivalent limit for the CERN fence will by far be met and that the effective dose, mainly due to muons, to the representative person from the public will remain well below $10 \mu\text{Sv}/\text{year}$. This situation is achieved thanks to the horizontal deflection of the muons by the active muon shield, which allows the bulk of the deviated muons to be confined well underground letting them range out without reaching the surface nor escaping the CERN domain.

Residual dose rates in the target area were evaluated for fifteen years of nominal operation with a total of 6×10^{20} PoT, showing that the target area is well optimised with the residual radiation well confined inside the target complex shielding. After one month of cool-down, the ambient dose equivalent rate outside of the shielding is very low.

Studies of air and nitrogen/helium activation occurring inside of the nitrogen/helium target vessel and the surrounding air in the TCC8 cavern have further demonstrated that air and nitrogen/helium releases into the environment have a negligible radiological impact on members of the public. The estimated maximum effective dose is $\sim 3 \text{nSv}/\text{y}$ for worst case of immediate release of the air. In order to further simplify the installation and increase

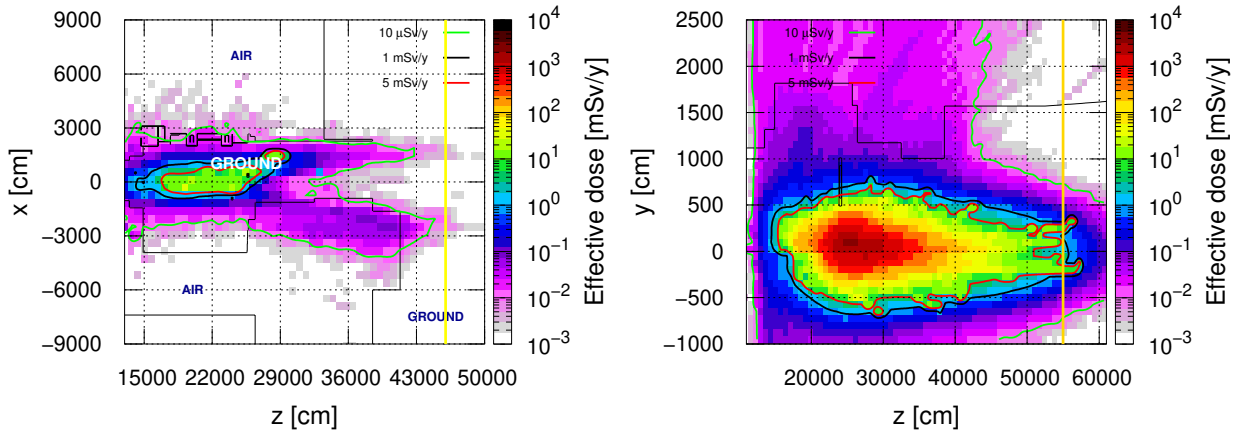


Figure 23: Left: the estimated effective annual dose due to muons downstream ECN3. Values have been averaged in y between 1225 cm and 1375 cm with the top of the hill downstream ECN3 at $y = 1770$ cm. Right: annual effective dose along the positive muon cone. Values are averaged for x between -2064 cm and -747 cm. Results are normalised considering 4×10^{19} PoT/year and a safety factor equal to 3. Yellow and gold lines in the two plots represent the location of the fence around the CERN domain.

the lifetime of the facility, it is currently considered to employ a primary vacuum around the target. This will further reduce the radiological impact of the facility and decrease the operational costs with extended lifetimes of components.

Finally, also soil activation and transfer of activation products to groundwater have been considered. Due to the current lack of information about the local groundwater transport, very conservative constraints on the activity concentration of longer-lived leachable radionuclides in the soil have been applied (1000 Bq/kg for ${}^3\text{H}$, 50 Bq/kg for ${}^{22}\text{Na}$). Shielding optimisation studies have been conducted to comply with the given design limits assuming 15 years of operation with a total of 6×10^{20} PoT. They concluded with the requirement of additional iron shielding embedded in a limited area of the TCC8 concrete floor below the BDF target (1 m of depth for a total volume of 13.2 m^3). A hydro-geological study is underway that will determine if the excessive conservatism in the applied limits can be relaxed.

To conclude, the design of the BDF in ECN3 can be considered optimised with respect to the radiological aspects. Thanks to this optimised design, the overall effective dose to members of the public remains well below CERN's dose objective of $10\text{ }\mu\text{Sv}/\text{y}$.

2.8 Evaluation of radiation to electronics

In conjunction with the RP studies of BDF/SHiP in ECN3, FLUKA Monte Carlo code has been used for the estimation of radiation environment in TCC8/ECN3 and its potential effect on electronics (R2E).

Generally, radiation when interacting in electronic components can cause different effects:

1. **Cumulative Effects** - Deterministic effects described by the damage to electronics

due to the energy deposited by radiation and to the induced displacement damage.

2. **Single Event Effects (SEE)** - Stochastic effects that can be either destructive (hard) or non-destructive (soft - e.g. Single Event Upset, SEU) for the electronics. SEEs are the main radiation effect of concern for largely distributed systems exposed to relatively low levels of radiation.

The study aimed at evaluating the risk that the installation of BDF/SHiP in TCC8 and ECN3 requires placing not-radiation tolerant commercial electronics in special R2E safe areas, or that radiation-tolerant electronics are required.

In order to have a quantitative description of the radiation effects to electronics, the following R2E-related quantities are considered in the study:

1. **Total Ionising Dose (TID)**
2. **Silicon 1-MeV Neutron Equivalent Fluence (Si1MeVNE)** - Particle fluence weighted by the damage function for silicon. The quantity is used for cumulative effects estimation.
3. **High Energy Hadron Equivalent Fluence (HEHeq)** - Proportional to the number of SEUs. It considers fluence of hadrons with energy higher than 20 MeV and neutron of lower energies weighted according to the ratio of their SEU cross section to the one of > 20 MeV hadrons.
4. **Thermal Neutron Equivalent Fluence (ThN-Eq)** - Proportional to the number of SEU's due to thermal neutrons. Neutrons of higher energies are weighted according to the ratio of their capture cross section to the one of thermal neutrons.

The quantities above are used to define general requirements, reported in Table 2, that allows characterising a particular zone as a R2E safe area.

Effects	R2E Quantity	Limit
Cumulative Effects	TID	10 Gy/year
	Si1MeVNE	$1 \times 10^{11} 1/(\text{cm}^2 \times \text{year})$
Single Event Effects	HEHeq	$3 \times 10^6 1/(\text{cm}^2 \times \text{year})$
	ThN-Eq	$3 \times 10^7 1/(\text{cm}^2 \times \text{year})$

Table 2: R2E safe area requirements

FLUKA simulations have been conducted to estimate the radiation environment both in TCC8, especially around the target complex and in the service room above, and in ECN3 at the detector locations. Results are reported in Figure 24 for TCC8 and Figure 25 for ECN3, considering the standard BDF operation with 4×10^{19} PoT/year.

The radiation to the detector and electronics in ECN3 is expected to be significantly below levels that require special measures, with the exception of the first part of the muon

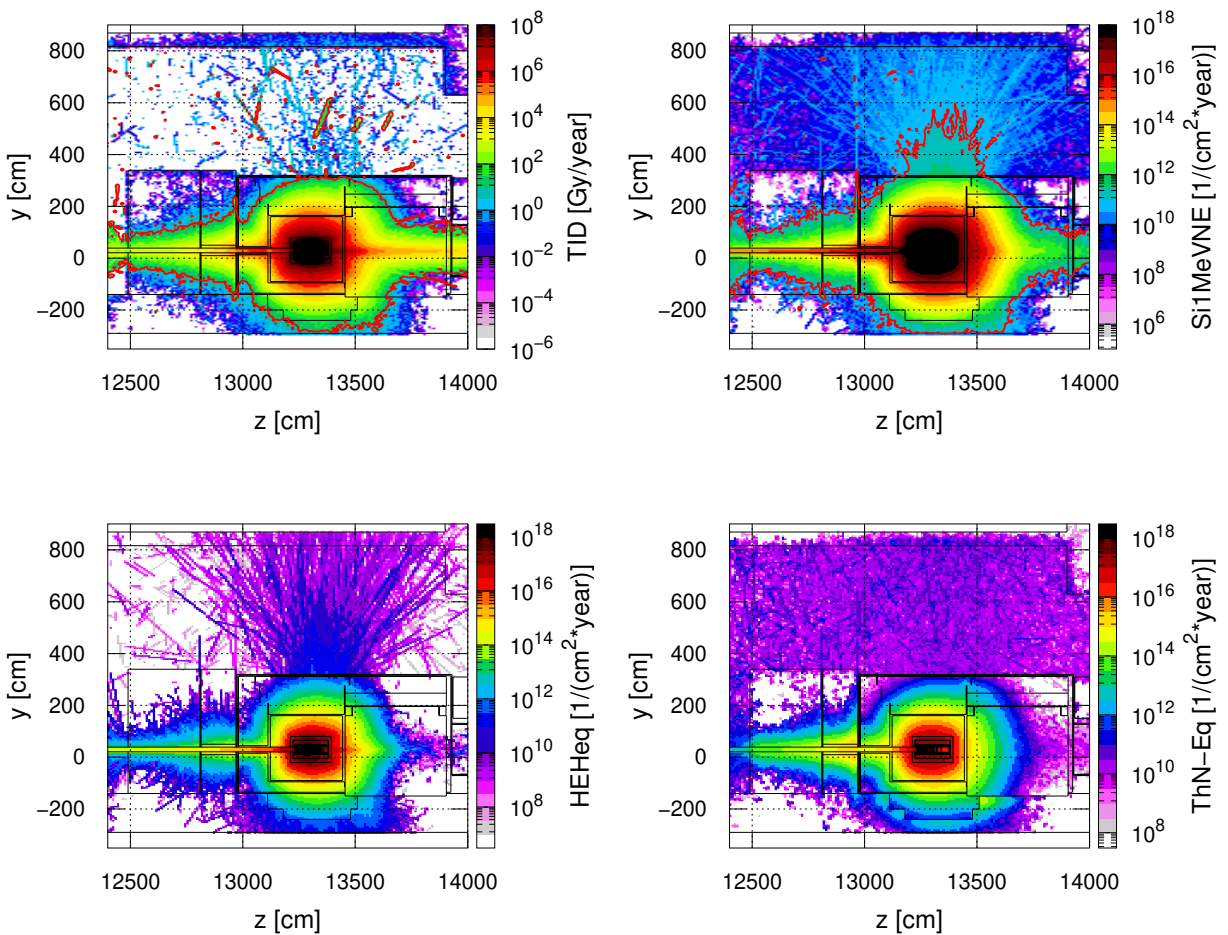


Figure 24: R2E estimation in TCC8 considering nominal BDF operation of 4×10^{19} PoT/year. Values represented in yz -plane, averaging x between 18 cm and 42 cm with beam line at $x = 26$ cm. Design limit for TID and Si 1MeV NE described by red contour, for HEHeq and ThN-Eq the requirements are described with the minimum value (white colour) of the palette.

shield and the side of ECN3 along the stream of muons. In any case, there is no need for development or application of radiation tolerant electronics.

For TCC8, the target complex is well-optimised and the radiation is well-contained inside the shielding. Further optimisation could be considered against back-scattered radiation coming from the target. It creates a critical environment for possible electronics installed close to the beam pipe. This region is the most critical area from the R2E point of view. Some precautions might also be necessary for electronics installed in the service room above the target complex, where the environment is mainly dominated by neutrons.

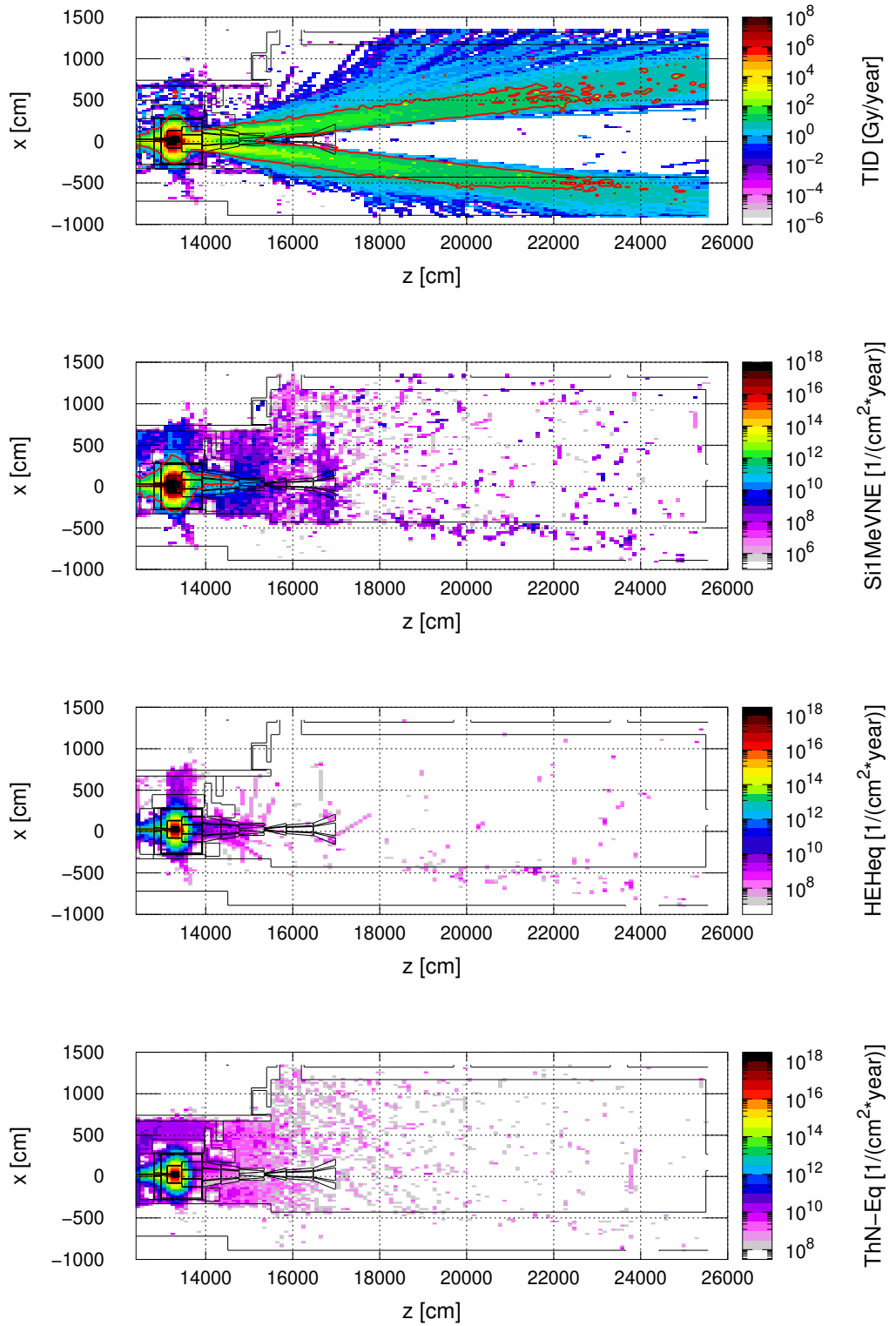


Figure 25: R2E estimation in ECN3 considering nominal BDF operation of 4×10^{19} PoT/year. Values represented in xz -plane averaging y between 25 cm and 50 cm with beam line at $y = 30$ cm. Design limit for TID and Si1MeVNE described by red contour, for HEHeq and ThN-Eq the requirements are described with the minimum value (white colour) of the palette.

3 Detector status and R&D

3.1 SND

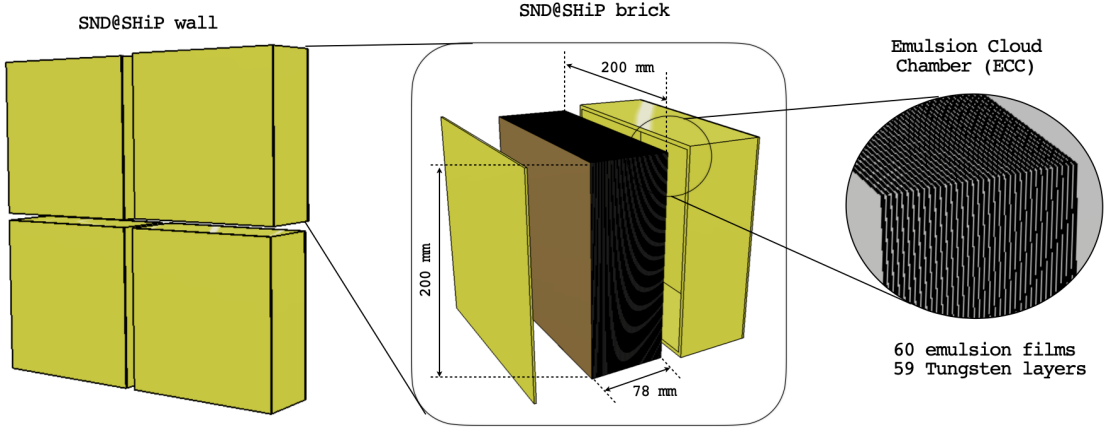


Figure 26: Layout of a single brick wall made of four emulsion cloud chambers (ECC).

3.1.1 Emulsion target

The LDM/neutrino detector target has a modular structure consisting of walls of emulsion cloud chambers (ECC) interleaved by target tracker planes that provide time stamping of the interactions occurring in the target and additional information for the energy measurement in the emulsion target.

The ECC technology makes use of nuclear emulsion films interleaved with passive absorber layers to build up a tracking device with sub-micrometric position and milli-radian angular resolution, as demonstrated by the OPERA [124] and the SND@LHC [125] experiments. The ECC is capable of detecting τ leptons [50] and charmed hadrons [51] by resolving their production and decay vertices. It is also suited for LDM detection through the direct observation of the scattering off the atomic electrons and nuclei in the absorber plates. The high spatial resolution of nuclear emulsion films allows measuring the momentum of charged particles through the detection of multiple Coulomb scattering in the passive material [53]. ECC is also a fine sampling calorimeter with more than three sensitive layers per X_0 . Electrons are identified by observing electromagnetic showers in the brick [52].

An ECC brick is composed of 60 emulsion films with a transverse size of $20 \times 20 \text{ cm}^2$, interleaved with 1 mm thick plates of tungsten. The resulting brick has a total thickness of $\sim 7.8 \text{ cm}$, corresponding to $\sim 17X_0$, and a total weight of $\sim 45 \text{ kg}$. The thickness of the wall has been optimised to have a sufficient number of tungsten plates in order to perform the momentum measurement exploiting the multiple Coulomb scattering (MCS) technique [126, 127]. As shown in Figure 26, each emulsion target wall is composed of 2×2 ECC bricks.

In the current baseline for ECN3, the LDM/neutrino target is made of 17 emulsion walls and 18 target tracker planes (Figure 27). In total, the target is instrumented with $\sim 160 \text{ m}^2$ of emulsion film. The overall target weight of the 17 walls is about 3 tonnes. The project profits

from the R&D on the tungsten plates that was performed by the SND@LHC experiment to select the best product in terms of composition and mechanical specifications.

According to the current estimate of the background flux, the emulsion films must be replaced a few times a year in order to keep the integrated number of tracks to a level $< 10^6$ particles/cm², and not to degrade the reconstruction performance. The films are analysed by fully automated optical microscopes [128, 129, 130]. SHiP is aiming at having a sufficient number of scanning stations to be able to scan each set of $\sim 160\text{ m}^2$ double-sided emulsion films in about one month. The scanning speed, measured in terms of film surface per unit time, has been improved in recent years [131, 132, 133]. The Japanese scanning system Hyper Track Selector (HTS) has been running at about 5000 cm² per hour for several years. For SHiP, this would correspond to an effective scanning time of about one month.

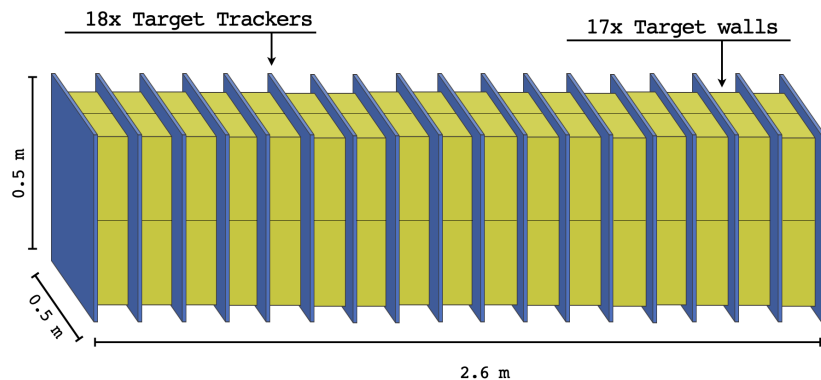


Figure 27: Layout of the SND LDM/neutrino detector target, made of 17 walls interleaved with 18 target tracker planes.

3.1.2 Target tracker

The baseline option for the SND target tracker system (TT) consists of 18 scintillating fibre tracker (SciFi) planes. The SciFi technology is well suited to cover large surfaces in a low track density environment, where $\sim 100\text{ }\mu\text{m}$ spatial resolution is required, as demonstrated by the SND@LHC experiment.

The TT has the role of predicting the location of the neutrino interaction in the emulsion brick and complementing the emulsion for the calorimetric measurement of electromagnetic showers. The TT also connects the emulsion track with the muon candidate track identified by the SND muon spectrometer, thus allowing identification of muon neutrino charge-current interactions.

The SciFi modules are closely following the design of the modules built for SND@LHC. The double-cladded polystyrene scintillating fibres from Kuraray (SCSF-78MJ), with a diameter of 250 μm , are blue-emitting fibres with a decay time of 2.8 ns. The fibres are arranged in six densely-packed staggered layers, forming fibre mats of 1.35 mm thickness. The readout consists of the photo-detector (S13552 SiPM multichannel arrays by Hamamatsu) at the end of the fibre module, a short Kapton flex PCB holding the photo-detector and signal connectors, and the front-end electronics board.

The active area of each plane is $500 \times 500 \text{ mm}^2$. The dimensions exceed those of the ECC in order to track particles emitted at large angles in several consecutive walls downstream of the ECC in which the interaction occurred. Additionally, a signal cluster shape analysis allows a modest single hit angular resolution which helps to resolve possible combinatorial ambiguities.

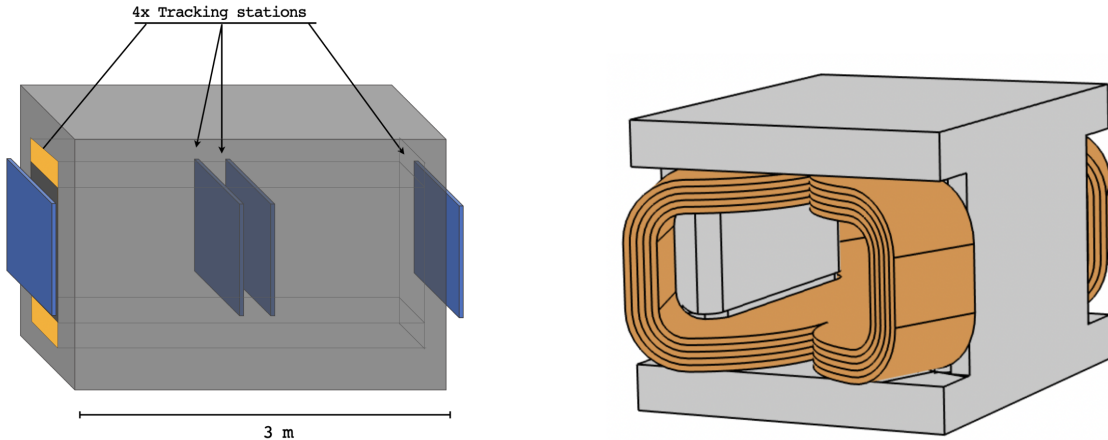


Figure 28: Layout of the SND muon spectrometer.

3.1.3 Muon spectrometer

The muon spectrometer is meant to measure the charge and momentum of the muons produced in muon-neutrino interactions and in short-lived particle decays, in combination with the HSDS muon spectrometer. Given the correlation between the emission angle and momentum, muons with high momentum can be reconstructed in the HSDS spectrometer. The SND spectrometer mainly focuses on those with lower momentum, thus reducing the requirements on the length and the bending power.

As shown in Figure 28, the spectrometer consists of an air core dipole magnet providing a 1 T horizontal field and four tracking station: one upstream, one downstream and two in the centre of the magnetised volume. The magnet provides the 1 T field over a length of about 3 m. It consists of two trapezoidal resistive coils bent at 45° on the two transverse sides, arranged inside an iron yoke of window-frame configuration. The magnet gap is wedge shaped in both vertical and horizontal direction to follow the detector acceptance, providing the required space for the frames of the tracking chambers positioned inside the magnet.

The four tracking stations allow for the reconstruction of muon momentum through the sagitta method. The sagitta is determined by the two stations in front and behind the magnet, measuring the track coordinates at the entrance and the exit of the magnetised region, and the two stations in the middle of the magnet, measuring the track coordinates in the centre of their trajectory. A position resolution of $100 \mu\text{m}$ is required for the measurement of the coordinate that undergoes deflection. The baseline option for the tracking stations are drift tubes [134].

3.2 HSDS

3.2.1 Decay volume

The decay volume for the FIP decay search is located immediately downstream of the SND at ~ 33 m from the centre of the proton target. The geometry and dimensions of the detector volume that define the decay acceptance have been obtained by an optimisation based on a wide range of FIP physics models and particle masses, the performance of the muon shield, and the aperture of SHiP’s spectrometer [135]. The resulting fiducial decay volume delineates a pyramidal frustum with a length of 50 m and upstream dimensions of $1.0 \times 2.7 \text{ m}^2$ and downstream $4 \times 6 \text{ m}^2$.

In order to suppress the background from neutrinos interacting with air in the fiducial volume, the volume is maintained at a pressure of $< 10^{-2}$ bar by means of a vacuum vessel. In this configuration, neutrino interactions only occur in the vessel walls. For this reason the wall structure should be optimised to be as light as possible, and should be instrumented all around with a background tagger that is capable of detecting muon and neutrino interactions in the wall, as well as residual muons entering the decay volume from outside.

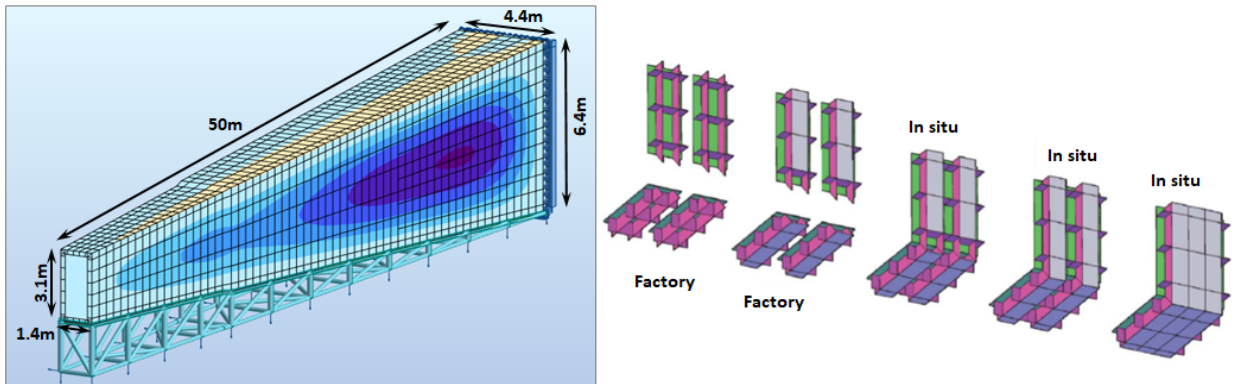


Figure 29: Left: layout of the decay vacuum vessel as simulated in the FEM analysis using "Robot Structural Analysis Professional" from Autodesk. Right: illustration of the components that will be assembled in factory and the assembly strategy in situ.

The combined requirement of the light wall structure and the need for a highly efficient background tagger system with both good timing and spatial resolution has been implemented in the form of a double-wall structure that incorporates compartments with a liquid scintillator-based detector system (SBT, see Section 3.2.3). The vessel double-wall structure consists of an inner wall of 20 mm, azimuthal and longitudinal strengthening members of 200 mm height and 15 mm thickness, and an outer wall of 20 mm, all parts constructed from S355JO(J2/K2)W Corten steel. This leads to the outer dimensions shown in Figure 29. The average wall material budget has been reduced from the equivalent of $0.75\lambda_I$ in the ECN4 CDS version to $0.5\lambda_I$ in ECN3, including the 200 mm liquid scintillator thickness. As shown in Figure 29, the SBT cells resulting from the wall structure vary in size along the length of the decay volume from $0.80 \times 0.5 - 0.9 \text{ m}^2$. In total the decay volume weighs 300 t (without liquid scintillator), has an inner surface of $\sim 690 \text{ m}^2$ and a vacuum volume of $\sim 580 \text{ m}^3$. The wall structure incorporates 1788 compartments (same as original CDS design) that make

up the SBT cells with a total volume of $\sim 145 \text{ m}^3$. Given the significant reduction in size, optimisation of the SBT cell size could reduce the number of cells to ~ 1400 without affecting the structural validity of the decay volume.

In order to avoid material between the decay volume and the spectrometer straw tracker (Section 3.2.5), the decay volume is directly connected via a bolted flange to the vacuum tank that runs through the spectrometer magnet and that hosts the 2 + 2 tracker stations, upstream and downstream of the magnet.

An upstream and a downstream end-cap close off the ends of the vacuum vessel, both attached to the vessel with the help of bolted flanges. To ensure that signal candidates are not produced by neutrino or muon interactions in the upstream SND, the upstream end-cap is covered by a high-efficiency upstream background tagger (UBT) (Section 3.2.2). The downstream end-cap is located just behind the last tracker station upstream of the timing detector and the particle identification detectors. The baseline design of both the upstream and downstream end-caps is based on flat panels, weld from a vertical stack of extruded profiles of aluminium alloy of type 6060. The material budget is equivalent to $0.18\lambda_I/0.8X_0$ in order to minimise the risk of neutrino and muon interactions in the upstream end-cap and not degrade the calorimeter performance after the downstream end-cap. Given the significant reduction in size of the upstream end-cap between the CDS design and ECN3, it appears possible to further reduce its material budget.

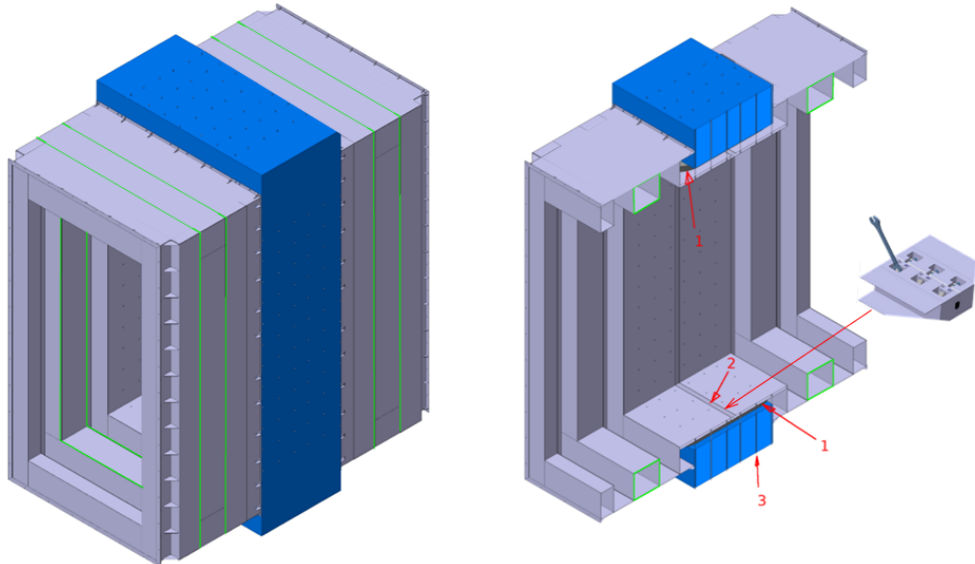


Figure 30: Left: layout of the spectrometer section vacuum tank, which is supported by the spectrometer magnet and which holds the main tracker stations. Right: the magnetic coils (1) are enclosed within the double wall structure. The vacuum tank consists of two sections joined together in the centre of the magnet (2). The vacuum tank wall running through the magnet is anchored by rods (3) through the magnet yoke.

The spectrometer section of the vacuum volume, Figure 30, is constructed from austenitic stainless steel and is mechanically supported by the magnet yoke. This section is also responsible for channeling the axial compressive vacuum forces resulting from the plug effect of the atmospheric pressure on the decay volume, and arrest them on the magnet yoke. For

this reason the external wall of the spectrometer section envelopes completely the magnet coils and services. In the CDS design, the tracker was inserted into the vacuum by a top-loader system including a flange and cover. ECN3 instead requires a side-loader system that, in addition to the flange and cover, must incorporate a slider support system.

A complete structural model of the decay volume for stress verification has been built and simulated with boundary conditions corresponding to the front-cap and the interface with the spectrometer section. This has also included an elaborate study of seismic effects. The norms to be applied have been discussed in detail with the CERN HSE unit. The work has been performed in close collaboration with a structural engineering company (CASTALDO S.p.A., Italy) specialised in large and complex metallic structures. A first iteration of mechanical engineering has been done including an elaborate evaluation of the welding and construction technique in factory, transport and assembly sequence in-situ. A conceptual design also exists for the vacuum vessel support structure.

The vacuum system [136] has been conceptually developed considering the need for large volume pump-down, the operational requirement on the vacuum of $< 10^{-2}$ bar which is capable of coping with the surface load and straw permeation load, and the leak testing. For regular operation, pump down time should be of the order of two-three days. Conservative assumptions have been taken for the surface load from the steel of the decay volume and the stainless steel of the spectrometer section. The pump-down scenario has been evaluated considering an unpainted internal wall of the entire vacuum tank. The load from permeation of drift chamber gas through the tubes of the straw tracker is known from NA62. With these assumptions, the surface out-gassing turns out to be at the same level as the straw permeation load. The permeation through the elastomer seals of the vessel's assembly introduces a negligible pumping load in operational conditions, but has been taken into account for the conditions required for leak testing.

The TDR phase will focus on finalising the mechanical design and the integration of the SBT and the vacuum system, as well as the vessel assembly technique and welding procedures. The proof of the executive design requires the construction of a large-scale prototype in the form of a complete ring of the decay volume. It will serve both for testing structural aspects in structural engineering test benches and for testing the performance of the SBT system.

A conceptual design of the spectrometer vessel section has been developed during the CDS study. It requires an update with the reduced dimensions in ECN3. The main challenge with the spectrometer section is the precision and tolerance management required during manufacturing and assembly, which will require close collaboration with a survey team during the construction. The many interfaces and links to adjacent components mean that the executive design and assembly procedure must be iterated together with the survey strategy.

For the end-caps, the TDR needs focus on the need for electron welding under vacuum. Efforts are currently concentrating on identifying companies which are capable of performing the welding operation of such large dimensions.

The vacuum system is not expected to present any challenges but need to be consolidated as the design of the vacuum vessel and its interfaces are refined during the TDR phase. The method for leak testing will require further studies in parallel.

If future detailed background studies confirm the possibility of operating the decay volume under one atmosphere of helium (see Section 4.2.3), it will result in significant design

simplifications. In particular, the need for the vacuum vessel through the spectrometer section would be eliminated, and instead be replaced with a thin end-cap fitted to the end of the decay volume, leaving the tracker stations in air. Structurally, the decay volume vessel would be similar to the current design in order to contain the helium volume and support the SBT, but the lack of vacuum forces will lead to a significantly reduced material budget.

3.2.2 Upstream background tagger

The UBT covers the front-cap window of the vacuum vessel. It is designed to suppress backgrounds for FIP signal events by tagging the time and position of muons passing the muon shield, and charged particles produced in neutrino and muon interactions in the passive material of the SND detector. An excellent time resolution, $\mathcal{O}(50\text{ ps})$, is aimed to maximise the UBT veto efficiency. Having a position resolution of the order of a few millimeters, the UBT also provides position information for muon tracks, complementing the SND muon spectrometer.

The envisaged technology is based on multi-gap resistive plate chambers (MRPC) with six gas gaps defined by seven 1 mm thick glass¹⁰ electrodes of about $1500 \times 1200\text{ mm}^2$, separated by 0.3 mm nylon mono-filaments. The HV electrodes are made up of a resistive layer¹¹ applied to the outer surface of the outermost glasses with airbrush techniques. The structure is permanently sealed inside of a plastic gas tight box with a 1 mm thickness equipped with feed-throughs for gas and HV connections. An UBT module is composed of two identical MRPCs structures. It is read out by 32 pickup electrode strips of copper with dimensions $1600 \times 37.5\text{ mm}^2$, located between them. The ensemble is enclosed in an aluminum case to guarantee electromagnetic isolation from the environment and sufficient mechanical rigidity. Each UBT MRPC is operated at $\pm 9000\text{ V}$. The HV system is based on CAEN commercial modules A1526 [137] and main frame SYS4527 [138].

A single layer of the UBT is made of three MRPC modules, arranged vertically, in order to cover the area of the vacuum vessel entrance. The active areas of the modules are overlapped by $\sim 20\text{ cm}$ in order to create a complete layer without dead regions, and to enable alignment between the modules.

The MRPCs are operated with 98% $\text{C}_2\text{H}_2\text{F}_4$ and 2% SF_6 in flow mode. The tightness of the system, provided by a novel approach in the detector design, allows operating each MRPC structure at a very low gas flow of around $5\text{ cm}^3/\text{min.m}^2$. An alternative possibility is the sealed RPC technology, a novel and emerging solution for the operation of MRPC without gas flow. This technology is still in the very early stages but will be taken into consideration.

A $1500 \times 1200\text{ mm}^2$ prototype was tested at the CERN test beam facility (see Figure 31(a)). Figures 31(b-e) summarise the timing accuracy and efficiency for all positions with average values of 54 ps and 98%, respectively [139]. In addition, this prototype has been put into operation as the time-of-flight (TOF) wall for the measurement of protons ($\sim 1\text{-}2\text{ GeV}/c$) time-of-flight in the experiment R3B S522 at GSI/FAIR (Darmstadt). The detector has been in operation for several months demonstrating reliability and robustness [140].

¹⁰Bulk resistivity of approximately $10^{13}\text{ }\Omega\text{cm}$ at 25°C .

¹¹Based on an artistic acrylic paint with around $100\text{ M}\Omega/\square$.

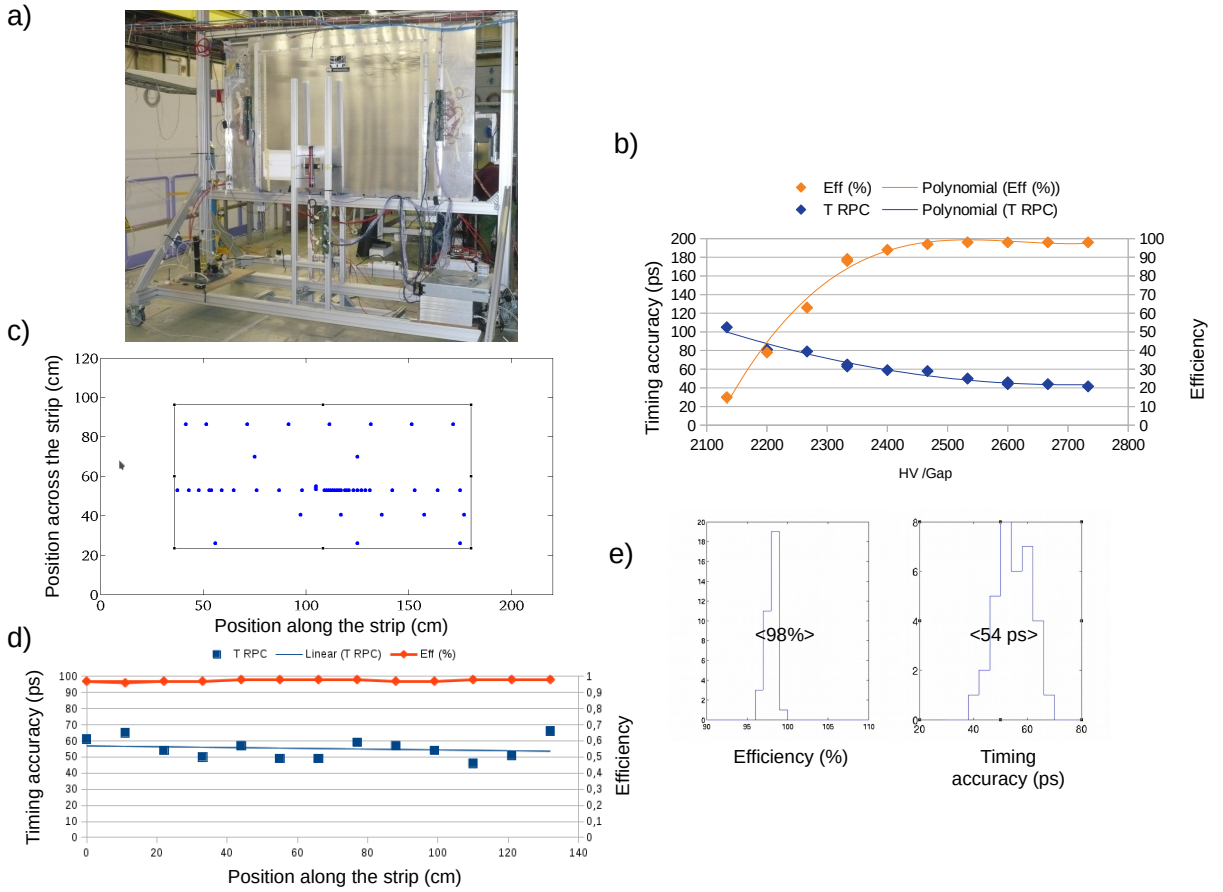


Figure 31: a) Prototype of the UBT tested at CERN. b) Efficiency and timing accuracy as a function of HV per gap for an arbitrary point on the surface of the module. c) Location of the different measured positions. d) Efficiency and timing accuracy along one of the strips of the module. e) Average values of efficiency and timing accuracy in different locations.

Need for further developments of the UBT will be decided depending on the results of the performance of the detector at the R3B S522 experiment.

3.2.3 Surrounding background tagger

The SBT must be capable of detecting charged particles either entering the vacuum vessel side walls from outside, or produced in the interactions of muons and neutrinos in the vessel walls. A time resolution of ~ 1 ns and spatial resolution of ~ 10 cm are essential to guarantee the SBT veto efficiency. The baseline option to cover the top-, the bottom-, and the side-walls of the vacuum vessel is using a state-of-the-art liquid scintillator (LS-SBT) consisting of linear alkylbenzene (LAB) together with 2.0 g/l diphenyl-oxazole (PPO) as the fluorescent. This technology provides a high detection efficiency and good time and spatial resolution at a reasonable cost.

The LS-SBT is sub-divided into individual cells integrated into the wall structure of the vacuum vessel, described in Section 3.2.1. Since the muon flux around the detector is sizeable, it is desirable to keep the distance between the outer and the inner decay vessel walls as small as possible. As the primary scintillation light yield scales with the LS thickness, this creates a trade-off between detection efficiency and hit rate in the LS-SBT. The SBT R&D originally started with a LS layer thickness of 30 cm. The latest prototype use 25 cm LS thickness, whilst the final aim is to achieve an LS thickness of 20 cm, which would result in the total LS volume of ~ 145 m³.

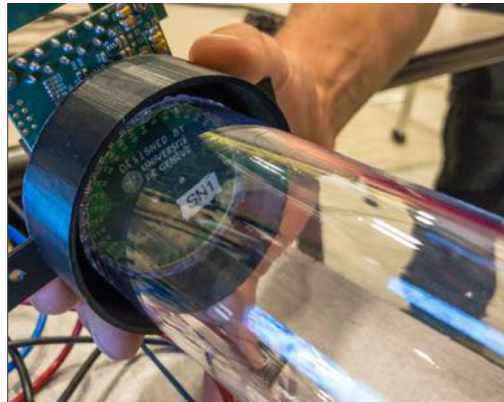


Figure 32: Coupling of the SBT wavelength-shifting optical module (WOM) tube to the 40-SiPM ring-array printed circuit board.

Each cell of the SBT is read out by two wavelength-shifting optical modules (WOM) made from PMMA tubes (diameter 6 cm, wall thickness 3 mm) that are dip-coated with a wavelength-shifting dye (77.31% toluene, 22.29% paraloid B723, 0.13% bis-MSB and 0.27% p-terphenyl [141]). WOMs absorb scintillation light in the range of 340 nm – 400 nm. To enable light transport of the secondary photons, emitted in the WLS layer with wavelengths above 400 nm, to the WOM end via a total internal reflection, the WOM tube is placed inside a PMMA vessel which separates it from the LS, thus creating a layer of air around the WOM. The secondary photons reaching the outer end of the WOM tube are detected by a ring-shaped array of SiPMs that is optically coupled to WOM. The SiPM array is made of

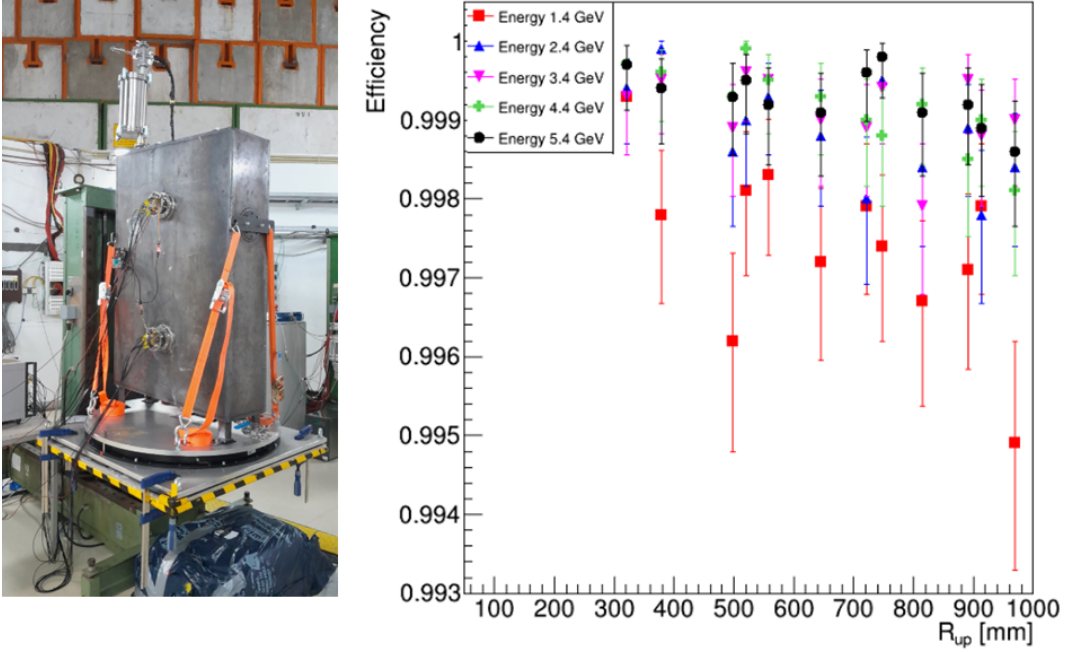


Figure 33: Left: SBT detector prototype equipped with two WOMs in the DESY testbeam area (fall 2022). Right: measured detection efficiency as a function of the distance between the particle beam position (with zero degrees incident angle) at the detector cell and the upper WOM tube in the detector prototype.

40 Hamamatsu S14160-3050, arranged in eight groups of five SiPMs (see Figure 32). With the current number of SBT cells, there are in total $\mathcal{O}(4000)$ WOMs for the whole SBT.

Beam test measurements in 2017 demonstrated the SBT proof-of-principle with a small-scale prototype of a WOM-equipped LS cell [142]. Combining two WOM signals, a time resolution of 1 ns and a homogeneity of the detector response over the detector volume within 20% were demonstrated. Further beam tests in 2018 - 2022 with prototypes of $120 \times 80 \times 30 \text{ cm}^3$ (see Figure 33(left)) achieved a detection efficiency for charged particles depositing at least 45 MeV (which corresponds to a minimum-ionising particle passing about 30 cm of liquid scintillator) $>99.3\%$ for distances between the passing particle and the WOM up to about 95 cm (see Figure 33(right)).

The time and spatial resolution of the detector cell were determined as well. Figure 34 shows the distributions of the average signal arrival time for the lower and upper WOMs. The corresponding particle beam positions at the detector cell are indicated by different colors for zero degree incidence angle. The standard deviations of the average WOM arrival times are well below 1 ns. The average between the two WOM signal arrival times varies within about 2 ns depending on the particle crossing point.

Detailed studies of the reconstruction of the spatial coordinates of the particle intersection point are ongoing using machine-learning techniques. Taking into account the signal yields and arrival times of the individual SiPMs in the two WOMs, preliminary results are very promising, showing a spatial resolution of $\sim(10)$ cm. Figure 35(right) shows the residuals of the x - y reconstruction for the two selected particle beam positions shown in Figure 35(left). The non-zero offset seen in the figure results from a left-right ambiguity

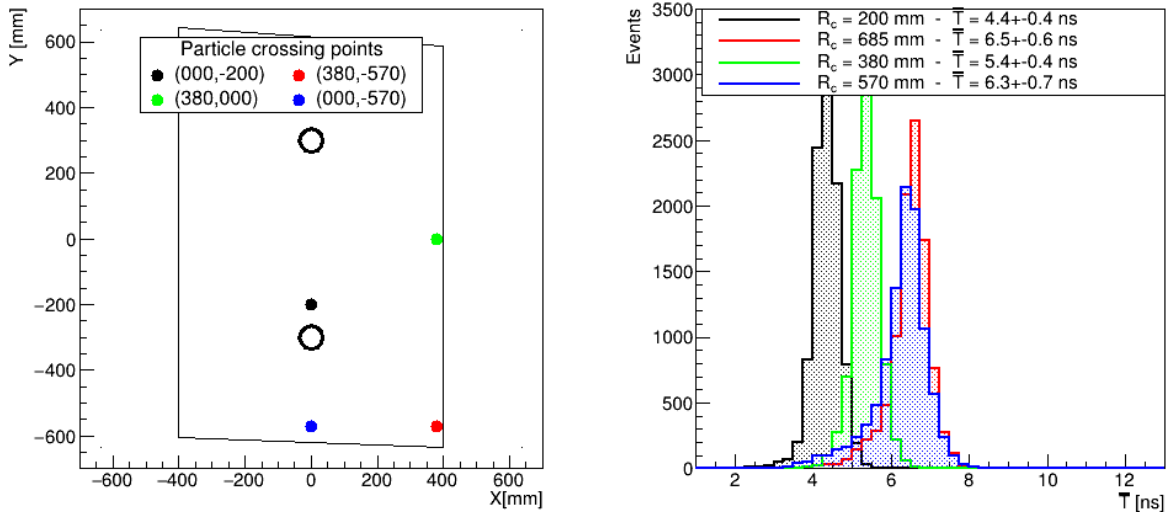


Figure 34: SBT signal arrival time distributions for different particle crossing points on the detector cell indicated by different colors. Left: Selected beam positions (x and y values quoted in the legend) on the detector box resulting in the largest time variation observed. Right: signal arrival time for the average of the arrival times at the two WOMs. The legend quotes the mean of the four different distributions and the standard deviation of the distributions.

in the track reconstruction by two WOMs having the same x -coordinate. The ambiguity is non-trivial to resolve given the loss of correlation between the particle scintillating light and the WLS light re-emitted in WOM. At SHiP, particles are expected to have mainly non-zero incidence angle and hence, cross more than one cell, leading to further improvement of the spatial resolution.

Tests with a liquid scintillator purified by Al_2O_3 columns, as described in [143], were also performed. It shows an increase of 20% in light yield compared to the measurements with an unpurified liquid scintillator. Moreover, the GEANT4-based photon-transport simulations show that covering the cell walls with acrylic BaSO_4 -coating is expected to increase the detected light yield by a factor of about five as compared to stainless steel walls. As a result, the detection technique is well-suited to achieve 99.9% detection efficiency over large-area liquid-scintillator filled cells for energy depositions even below 45 MeV.

Further developments and key engineering studies required during the TDR phase include:

- Prototyping of various WOM/PMMA, geometries, development of the dip-coating setup and a test stand for the quality control measurements during a large scale WOM-tube production. Production of $O(100)$ WOM tubes for the performance tests and quality control of the dip-coating procedure for future mass production. This includes the WOM production (and their assembly with SiPM arrays) to instrument the large-scale two-ring detector prototype.
- Definition of the optimal liquid scintillator, comparing different vendors and qualities

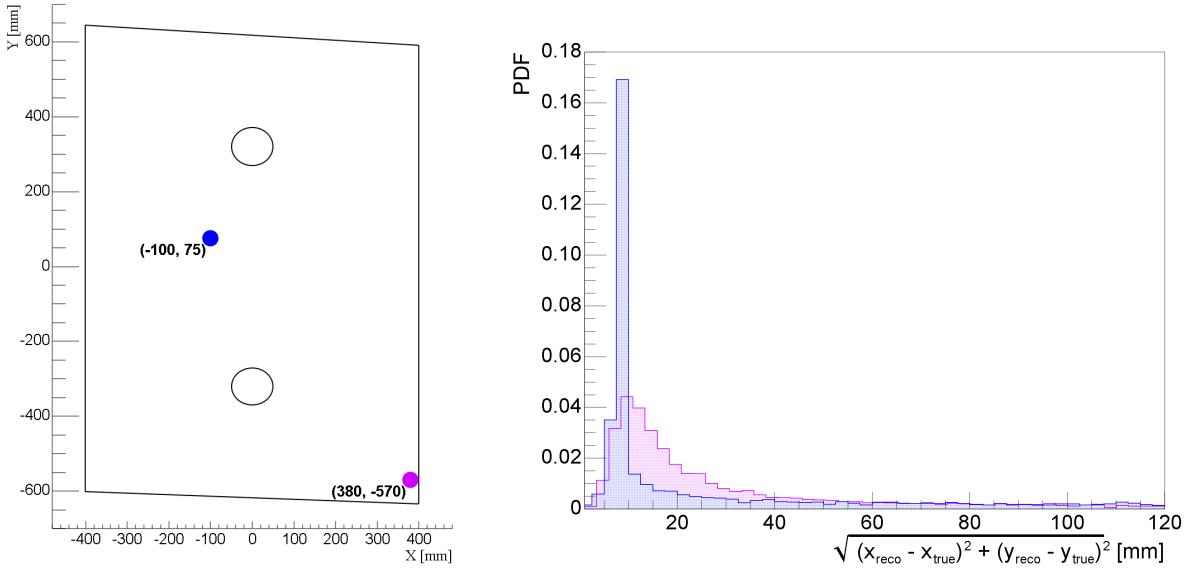


Figure 35: The root-mean-square distribution of the NN-based reconstructed x - y position with respect to the true particle beam position for two selected beam positions shown on the left.

of LAB, and clarification of the necessity of the LAB purification. In case of a need for purification, design of a large-scale purification facility at CERN. Ageing tests of all components with respect to 15 years of operation.

- Design and construction of a two-ring vacuum vessel prototype LS-SBT with dimensions corresponding to the decay vessel entrance in order to address all integration-related aspects. Tests with cosmics and beam will be performed to develop the time and energy calibration methods, and to emulate the system response to electromagnetic showers generated upstream of the prototype.

These studies require significant test beam activities during the TDR phase such as:

- 2023 – 2024: Test of a 4-cell prototype at CERN PS with 20 cm LS thickness and improved inner-wall reflectivity. Test should be repeated after at least six months to check for possible aging of the coating.
- 2025: Production of the two-ring vacuum vessel prototype, followed by the test beam exposure.

3.2.4 Spectrometer magnet

The main spectrometer magnet is required to have a physics aperture of $4 \times 6 \text{ m}^2$ and provide a vertical bending power of about $\sim 0.65 \text{ Tm}$ over the distance between the upstream and the downstream tracking stations. As the magnet aperture is limited in the horizontal plane by the region cleared from the beam-induced muon flux, the choice of the horizontal field orientation is motivated by the shorter field gap.

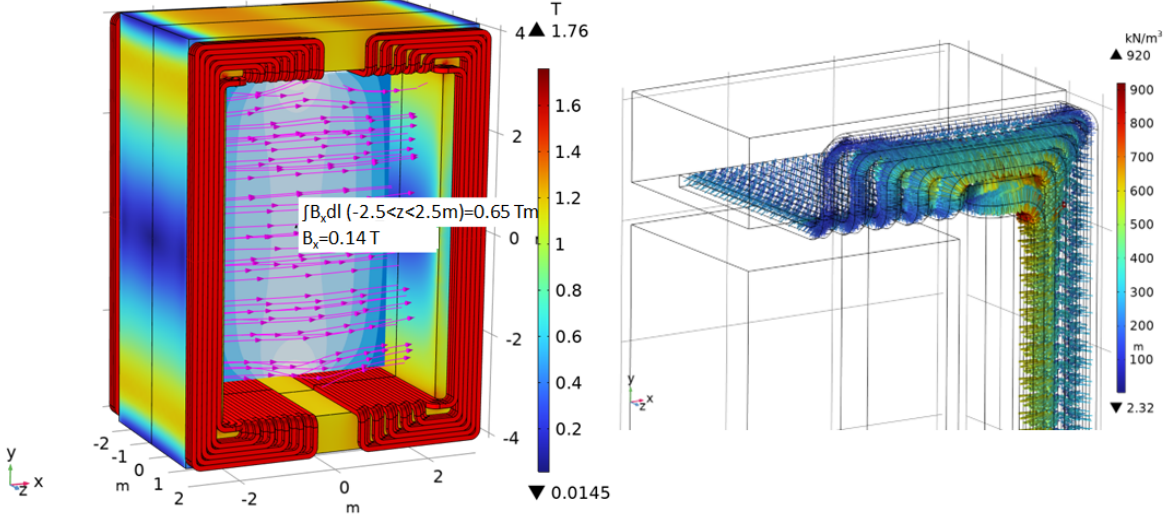


Figure 36: Preliminary simulation of the $4 \times 6 \text{ m}^2$ -aperture spectrometer magnet for ECN3 showing the field map (left) and the Lorentz forces on the coils (right).

The design of the main spectrometer magnet was initially based on normal-conducting technology [144, 145]. In this option, the coils are made from a square-shape hollow aluminum conductor with transverse dimensions of $50 \times 50 \text{ mm}^2$ and a bore hole of 25 mm for water cooling. The yoke is built from packs of 50 mm thick sheets of AISI 1010 steel. The pack is assembled in a brick-laying fashion around the corners. In terms of aperture, 100 mm has been reserved all around the physics aperture to accommodate the vacuum vessel and its anchoring within the yoke. The original CDS magnet design has undergone two iterations of studies, including numerical simulations. A three-dimensional magneto-static finite element model has been constructed, in parallel to modelling by the CERN TE/MSC group with OPERA 3D. A preliminary update of the model (Figure 36) has been done with the dimensions for ECN3 in order to provide the physics simulation with realistic full-3D field maps. The result is a ~ 700 -tonne yoke with two vertical coil packs of ~ 25 tonnes each. The simulations show that the required magnetic performance can be obtained with a current density of 1.5 A/mm^2 , which with the updated magnet dimensions in ECN3 results in an excitation current of $\sim 2000 - 2500 \text{ A}$, resulting in a total power consumption of $\sim 0.5\text{-}0.6 \text{ MW}$.

During the CDS phase, superconducting alternatives were investigated [145] in order to identify a competitive option in terms of power consumption and material cost. The investigation explored different solutions with coils made of either Nb-Ti, Nb₃Sn, MgB₂ or ReBCO superconductors. The strategy adopted for the protection of the magnet relies on an external dump resistor as energy extraction system, with the superconductor itself stabilised with enough copper to allow this operation in case of quench (Figure 37). The study focused on the operating margins of the different options and the cost of the coils. Figure 38(left) compares the options in terms of quench current margin. All materials can work with conformable margin of more than 40%. The right-side figure compares the options in terms of temperature margin. The MgB₂ and the ReBCO conductors offer large stability against thermal disturbances with a margin of more than 5 K to quench. From these first considerations, it is expected that the cryogenics needs could be satisfied by conduction

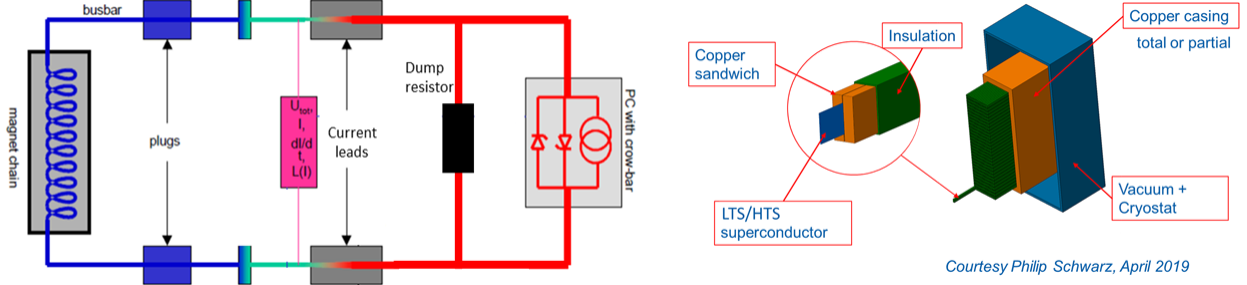


Figure 37: Left: Electrical circuit featuring the power converter in series with the spectrometer magnet through current leads and bus bar. The dump resistor is set in parallel to the magnet (reproduced from [145]). Right: conceptual layout of the spectrometer magnet coil in the superconducting option.

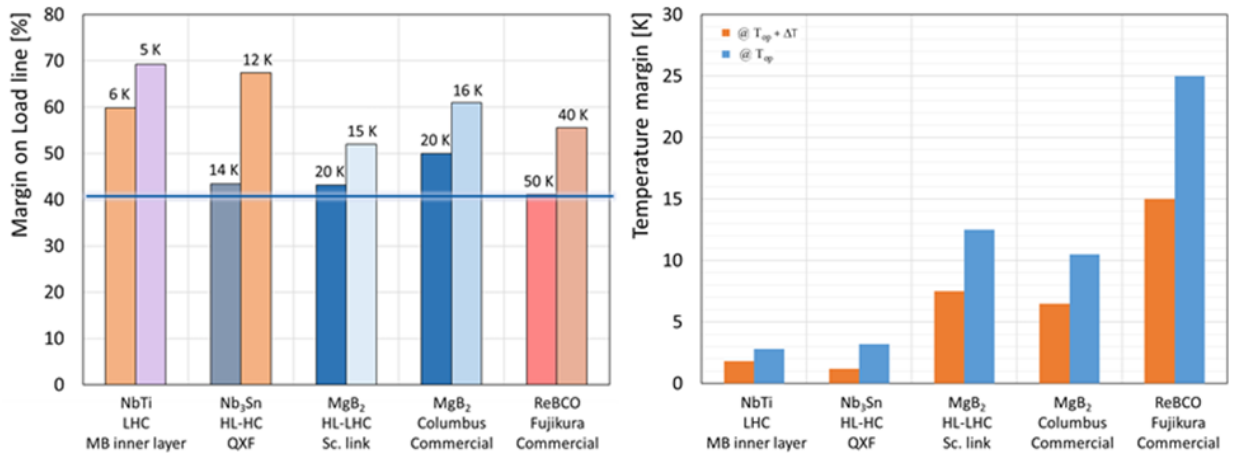


Figure 38: Left: Comparison of the margin for Nb-Ti, Nb₃Sn, MgB₂ and ReBCO conductors. The operating temperatures with or without margin are given for each case. Right: Comparison of the temperature margin for Nb-Ti, Nb₃Sn, MgB₂ and ReBCO conductors. The operating temperatures with or without margin are given for each case.

cooling or gas cooling, which would significantly simplify the complexity of the coils as compared to low-temperature liquid cooling. It is also expected that the overall power consumption would be reduced by a factor of ten, as compared to a resistive magnet, if the cooling is provided by cryocoolers. This could be potentially even less if the more costly option of a cryogenic line from a liquefactor would be made available. All superconducting options were found to be technically feasible. In particular, considering the relatively low peak field induction, the MgB₂ option was considered promising as the first candidate for a demonstrator. Further R&D towards a demonstrator is currently ongoing im TE-MSC with a SHiP institute contributing under a collaboration agreement. While SHiP is the use case for this study, the actual technology would be a valid candidate for any future experiment magnets, and could also be used to retrofit already existing magnets, in order to significantly reduce their power consumption.

3.2.5 Main tracker

The spectrometer straw tracker (SST) is designed to reconstruct signal candidates by measuring precisely the trajectories and momenta of charged particles, and to reconstruct the decay vertices and the impact parameters at the proton target.

To reach the required spatial resolution of $120\text{ }\mu\text{m}$ across the aperture of $4 \times 6\text{ m}^2$, a detector with a low material budget operable in vacuum has to be used. Ultralight straw tubes fulfill these requirements and are chosen for the tracking detector in vacuum.

The spectrometer consists of a total of four tracking stations, two each up- and downstream of the spectrometer magnet. The two stations on either side of the magnet are separated by 2 m. A 5 m gap, with the magnet in the centre, separates the upstream and the downstream pair of stations. Each tracking station is equipped with horizontal straw tubes of 4 m length and 2 cm diameter, and consists of four views with two layers each in a $Y-U-V-Y$ configuration, where the U and Y -views are inclined by a stereo angle of approximately $\pm 5^\circ$. To cover the acceptance region of $4 \times 6\text{ m}^2$, this results in $\sim 10\,000$ channels altogether.

The straw design is inspired by the experience of NA62, using ultralight ultrasonically welded BoPET straws [146], fabricated from $36\text{ }\mu\text{m}$ thin Cu/Au-coated Mylar foil. The large aperture and low hit rates suggests using straws with larger diameter compared to NA62. First prototype straws with a diameter of 2 cm and lengths of up to 5 m have been produced and successfully tested in small prototypes and test-beam measurements [147, 148]. The straw-tubes are operated with an Ar/CO₂-mixture ($\sim 70/30$) at one bar and a high voltage of $\sim 2\text{ kV}$ to achieve the foreseen spatial resolution of $120\text{ }\mu\text{m}$ with a hit efficiency of $> 99\%$.

The main challenge is the mechanical properties of the straw tubes, as the cathode straw-material relaxes over time, whereas the anode wire does not. This results in a slow but continuous increase of sagging to be counteracted. For this, three concepts have been developed in the past: the use of constant force springs in an expanding frame [149], building a cemented pack of straws [150], and the use of thin carbon cables as support [151]. In each option, the tracker stations are assembled in support frames which can be inserted into the spectrometer vacuum vessel from the side.

The first option involves the concept of pulling on the straws with an adjustable traction over time, while decoupling the wire via a custom-made constant-force spring [149]. An expanding frame increases the traction on the straw over time to counter the change in sagging of the cathode material [152].

The second option is inspired by the PANDA self-supporting straw tracker. The stiffness of the straw modules is radically boosted by gluing together a number of straws into a cemented pack [150]. First prototyping has started with shorter straws, depicted in Figure 39.

The third option explored, uses thin carbon cables for horizontal straw support. The concept foresees a modular design with common end-plates shared by 64 straws, to be mounted in a larger frame [151]. Figure 40 shows a prototype using four straws, that has been set up and operated successfully in Hamburg.

Analog readout and digitisation should be done directly on the front-end board. The ZEA-2 group from Forschungszentrum Jülich is working on a general purpose readout chip to be used by both the SBT and SST. First tests have been performed with the TIGER and VMM3 ASIC as a front-end alternative.

The technology of longitudinally, ultrasonically welded straws has been proven to be



Figure 39: Prototype of the cemented pack design option with partly metalised tubes.



Figure 40: Four-straw prototype with carbon fibre suspension under test in Hamburg.

a suitable technique for the SHiP spectrometer straw tracker under vacuum. Originally designed for the NA62 experiment, it is a relatively new and attractive straw-tube technology, allowing for the gas-tight use under over-pressure in vacuum. Several other current and future projects are now planning to use this technology, including e.g. NA64, SAND—one of the DUNE near detectors, but also SHADOWS. Originally produced by JINR Dubna, the technology is currently being disseminated to other institutes, including a cooperation of ZEA-1 at Forschungszentrum Jülich with Hamburg University to build a straw production line for SHiP. A future transfer to industry is also possible and has already been done successfully by NA62.

A first design of the spectrometer straw tracker was presented in the SHiP Technical Proposal in 2015 [10]. While the main features of the concept remain unchanged, several details have been updated since. Key differences are the increase of the straw diameter from 1 cm to 2 cm, the reduction of the straw pitch, the reduction of the number of tubes per layer from four to two and most recently, the significant reduction of size from a $5 \times 10 \text{ m}^2$ top-loader to a $4 \times 6 \text{ m}^2$ side-loader in the scope of the re-design for ECN3.

Prototype tubes of 2 cm diameter and 5 m length have already been produced and used in different tests and prototypes at CERN and at Hamburg University.

In 2017, test beam measurements were performed at CERN, using a 2 m long tube of 2 cm diameter. In particular, the effect of offsets from the anode wire to the centre were tested and it could be shown that the straw hit resolution of $<120 \mu\text{m}$ is achievable with high hit efficiency over most of the straw diameter, independently of the wire eccentricity (see Figures 41 and 42).

In 2019, first small prototypes were built to test two of the suggested mechanical concepts. A small number of shorter tubes were glued together to a cemented pack at CERN while the carbon fiber suspension was tested in a 5 m long setup in Hamburg. The latter is now

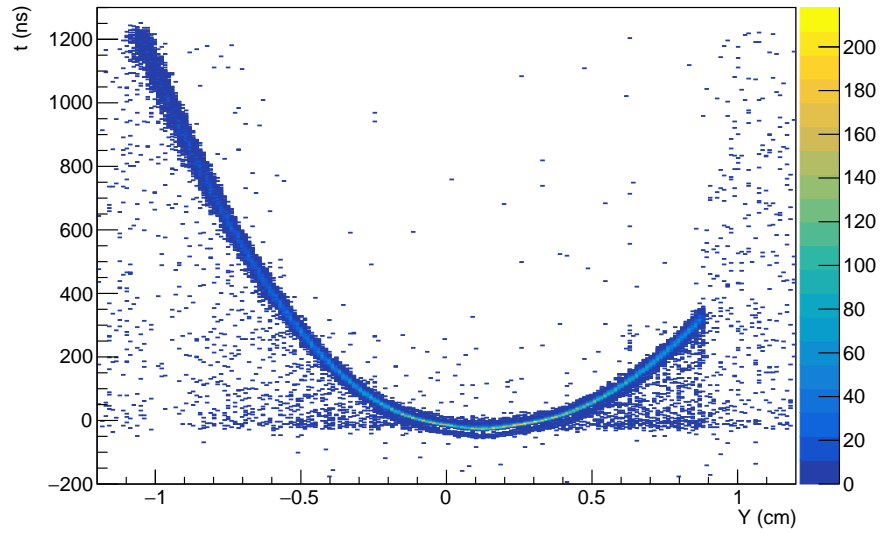


Figure 41: Measured drift time versus Y position of the reconstructed particle trajectory with the 20 mm diameter straw-tube prototype with a large wire eccentricity (2.05 mm). The Y axis is vertical, perpendicular to the wire axis X and to the particle beam axis Z.

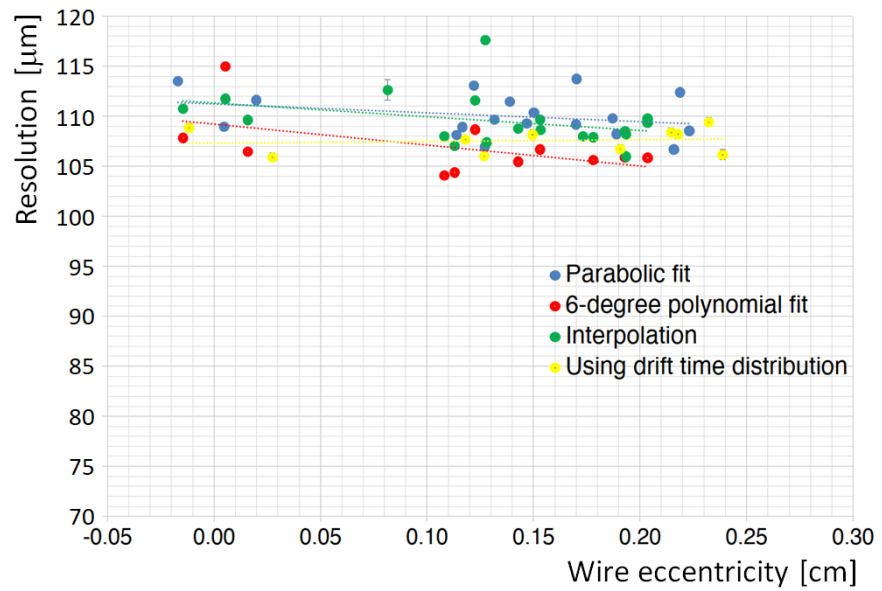


Figure 42: Measured spatial resolution for the 20 mm diameter straw-tube prototype as a function of the artificially induced wire eccentricity. Four different analysis methods of the spatial resolution are compared (see CERN-THESIS-2020-218). The lines are the results of linear fits.

again in operation and is currently used to study the impact of relaxation over time after four years since construction.

The next important step in developing the SST is to converge on a single design option. Once an independent straw production line has been established, a prototype module of $\mathcal{O}(100)$ tubes will be built and intensively tested for mechanical properties as well as for physics performance. For the latter, further test beam measurements are needed. The readout will then be done with a first version of the front-end chip currently designed by FZJ. Alternatively, a possible use of the VMM3 and TIGER readout chips for readout is currently being tested. Depending on the chosen concept, a corresponding frame needs to be designed. Further open issues are the cooling system for operation in vacuum, vacuum feed-throughs as well as the design of a dedicated gas system.

3.2.6 Timing detector

The spectrometer timing detector is located outside of the vacuum vessel right after the aluminum end-cap and in front of the particle identification system. It covers an area of $\sim 4 \times 6 \text{ m}^2$. Its primary role is to reduce the combinatorial background by a measurement of the time coincidence of particles. It also provides time information for the straw tracker, and can enhance particle identification by measuring time-of-flight of particles with momenta up to $10 \text{ GeV}/c$.

In order to reduce combinatorial di-muon background to an acceptable level, a time resolution of $\leq 100 \text{ ps}$ is necessary.

The detector comprises three vertically staggered columns of EJ200 scintillator bars with dimensions of $144 \text{ cm} \times 6 \text{ cm} \times 1 \text{ cm}$. Each bar is read out on both ends by an array of eight SiPMs attached to custom pre-amplifier PCBs, and subsequently read out by a DAQ based on SAMPIC. The bars are arranged in three columns and 110 rows. There is a 5 mm overlap between bars in the vertical direction and $\sim 10 \text{ cm}$ overlap in the horizontal direction. In total there are 330 bars corresponding to 5280 SiPMs grouped into 660 readout channels.

The material for the scintillator plastic was chosen by the requirement on the time resolution. EJ200 is found to have the right combination of light output with $\mathcal{O}(10^4)$ photons generated per minimum-ionising particle crossing 1 cm, attenuation length of 3.8 m, and fast response with signal rise time of 0.9 ns and decay time of 2.1 ns. The wavelength emission spectrum peaks at 425 nm, closely matching the SiPMs spectral response. The bars are wrapped in an aluminum foil and a black plastic stretch film on top to ensure opacity.

Several test beam measurements have been carried out at the CERN PS on single bars of various lengths, scintillator types, and SiPM array configurations. The original result comes from June and October 2017 where a single bar of EJ200 scintillator with dimensions $150 \text{ cm} \times 6 \text{ cm} \times 1 \text{ cm}$ was measured at the T9 beamline of the East Hall of the CERN PS. An array of eight Hamamatsu S13360-6050PE SiPMs on both ends of the bar was used to collect the scintillating light. Each array was read out by a custom ASIC called MUSIC (Multiple Use SiPM IC), developed by the University of Barcelona, which provides an analog sum of all eight SiPM channels with pole-zero cancelation and individual control for the bias voltage offset and gain of each SiPM. The waveforms were recorded by a 16-channel waveform digitiser, WAVECATCHER, running with a sampling frequency of 3.2 GS/s. The time resolution of the bar was determined by placing two reference counters upstream and

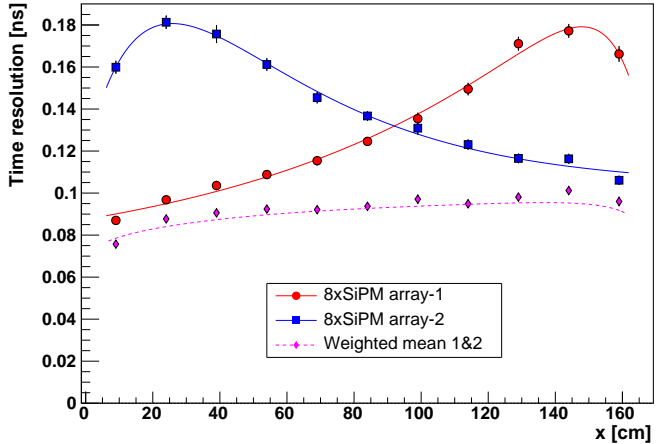
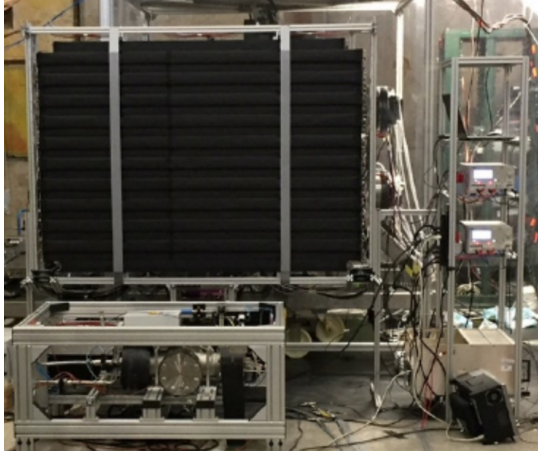


Figure 43: Left: picture of the timing detector prototype comprising 22 bars, placed in front of a high-pressure TPC and exposed to test beams at the CERN PS in summer 2018. Right: time resolution as measured by the SiPM arrays at both ends of a 168 cm bar as a function of the beam impact position along the bar [154].

downstream of the bar and subtracting their measurements from the time detected by the SiPM arrays of the bar under test. The resulting time resolution along the bar was found to be 80 ps [153].

In July 2018 a 22-bar prototype, shown in Figure 43(left), consisting of a single column of vertically staggered bars covering an active area of $168 \times 120 \text{ cm}^2$ was constructed [154]. Each bar had dimensions of $168 \text{ cm} \times 6 \text{ cm} \times 1 \text{ cm}$, with the exception of the top and bottom bar which had the same cross-section but were 18 cm shorter in length. Again, the light on each bar was collected by an array of eight Hamamatsu S13360-6050PE SiPMs biased to an over voltage of 5 V. Each array was mounted onto a custom PCB which was read out by an eMUSIC chip. A modified version of the original MUSIC board was employed in the readout. Signals from each channel were digitised using a 64-channel SAMPIC module. The prototype was tested in August and September of 2018 at the T10 beamline of the CERN PS.

The time resolution along a single bar is shown in Figure 43 (right). It ranges from 80 ps for the interaction point located near the sensor, to 180 ps for the interaction point located at the opposite end of the bar to that of the sensor. This deterioration in accuracy is due to the smearing of the signal leading edge during its propagation along the length of the bar. The resolution calculated as a weighted mean between SiPM-arrays located at two ends of the bar, makes the distribution more constant, equal to an average of 85 ps. As a proof of maturity, the technology developed for the SHiP timing detector was recently implemented for the large time-of-flight system of the T2K near detector.

During the TDR phase the following items need to be addressed:

- Finalisation of the calibration procedure to demonstrate the time resolution across the entire detector.
- Validation of the readout electronics at the test beam with the scintillating bar of the correct dimension. Measurement of the detection efficiency and the time resolution

with the final readout electronics.

3.2.7 Particle identification detectors and photon detection

Particle identification (PID) in SHiP was thoroughly studied with the FairShip simulation during the TP and the CDS phases [155, 156, 157, 84] in various detector configurations, which included electromagnetic and hadronic calorimeters, and dedicated detectors for muon identification.

In the SHiP CDS configuration [84], the detector is not equipped with a hadron calorimeter. The electromagnetic calorimeter has a lead absorber with a total thickness of $17.8 X_0$, i.e. about one nuclear interaction length. This segmentation and the total thickness guarantee optimal electron/pion separation, but is not sufficient for muon/pion separation, given that only about 67% of the pions would start a shower in the calorimeter. Hence, in this configuration, muon/pion separation is based on muon reconstruction in a muon detector with digital readout and four stations of active layers interleaved by four absorbers, one immediately downstream of the calorimeter to reduce occupancy from electromagnetic shower tails and to absorb low energy pions, followed by three 60 cm thick iron walls corresponding to 3.4 interaction lengths (λ_I). One additional thin (~ 10 cm) layer of iron located downstream of the last station shield the system from background scattered in the cavern walls. This leads to an identification of muons with an efficiency of $> 95\%$ in the momentum range of between 5 and 100 GeV/c with a mis-identification rate of 1 to 2%.

The ongoing PID optimisation studies a possible merging of the calorimeter and the muon detector technologies, naturally leading to an integrated PID detector with a dedicated electromagnetic calorimeter section and a compact sampling hadron calorimeter with a depth of about $6 \lambda_I$, with $\sim 1 \lambda_I$ thick absorber layers. Scintillating bars and scintillating tiles with direct SiPM readout were already investigated as technological options for the active layers [157].

Apart from providing electron and photon reconstruction and identification and discriminating between hadrons and muons, the electromagnetic calorimeter should be capable of measuring the electromagnetic shower energy and, in particular, the shower angle with a resolution of ~ 5 mrad to reconstruct two-photon final states, such as $\text{ALP} \rightarrow \gamma\gamma$.

The electromagnetic calorimeter is based on the *SplitCal* concept, first proposed in Ref. [155]. It consists of a longitudinally segmented lead sampling calorimeter with a total sampling depth of $20 X_0$. The lead absorber plates are $0.5 X_0$ thick, i.e. 0.28 cm, thus leaving space for 40 sampling layers. Most sampling layers are equipped with scintillating plastic bars read out by WLS fibres with a modest spatial segmentation. The scintillator planes are 0.56 cm thick.

Three sampling layers, each with a thickness of 1.12 cm, are equipped with high resolution detectors providing a spatial segmentation of ~ 200 μm . They are located at a depth of $3 X_0$ and at the shower maximum in order to accurately measure the barycentres of the transverse shower profile. The shower direction is determined from the three measurements of the barycentres. For the high-resolution layers, it is foreseen to use micro-pattern detectors, such as micro-megas.

To increase the lever arm for the angular measurement, the calorimeter is mechanically split in two parts in the longitudinal direction with an air gap of 1 m between the first

$3 X_0$ and the remaining $17 X_0$. With a few mm transverse shower-position resolution in the high-precision layers, the target angular resolution is of the order of a few mrad.

The principal challenge in achieving a good angular resolution, along with high efficiency for the photon reconstruction, is the presence of shower satellites due to long tails in the transverse shower shape. The shower profiles were measured with a prototype at an electron beam test at CERN in order to tune the simulation and optimise the layout.

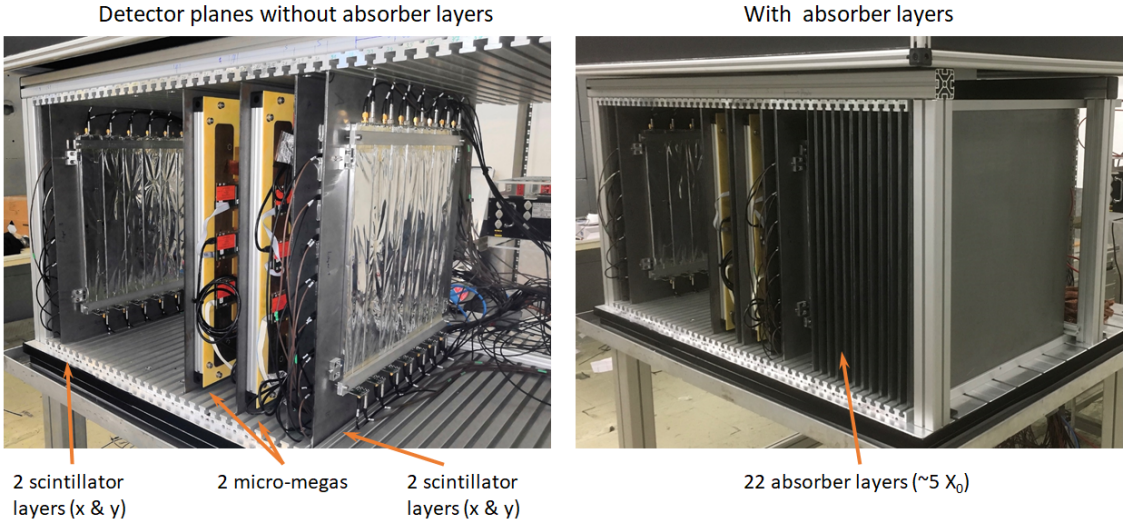


Figure 44: Test beam setup for the electromagnetic calorimeter measurements of the shower profiles.

The test setup is shown in Figure 44, and the experimental results, comparing data and simulation at different shower depths, are shown in Figure 45.

The fractional energy resolution of the calorimeter is around $15\%/\sqrt{E}$. As such, its contribution to the mass resolution is largely sub-dominant compared to the angular resolution.

By appropriate readout of the scintillator planes, a very good time resolution could be achieved for showers of a few GeV, which would help the rejection of combinatorial background. It was already demonstrated in the framework of R&D on the LHCb upgrade II, that a time resolution better than 50 ps can be achieved with plastic scintillator calorimeters.

A new prototype is currently being built. It will be made of 192 channels of SiPMs over 32 layers, each with six scintillator strips of $36 \times 6 \text{ cm}^2$ area. The readout is done through 6×6 SiPMs (S14160-6050HS from Hamamatsu) on both sides of the strips but only half of the layers will include WLS fibres traversing the strips. The SiPMs are mounted on PCBs which include a small changeable circuit to accommodate the different readouts, but no pre-amplification. There are therefore two PCBs per strip, one per SiPM, analogous to the previous prototype.

The study of the readout electronics will focus on the KLauS chip from Heidelberg with other options available, such as the Weeroc CITIROC and perhaps the TOPFET from EPFL.

Future R&D will focus on new fast readout electronics, scintillator tile uniformity, optimal SiPM-tile coupling and the possibility of reading out tiles without WLS fibres. This effort will culminate in the construction and test of a large scale prototype.

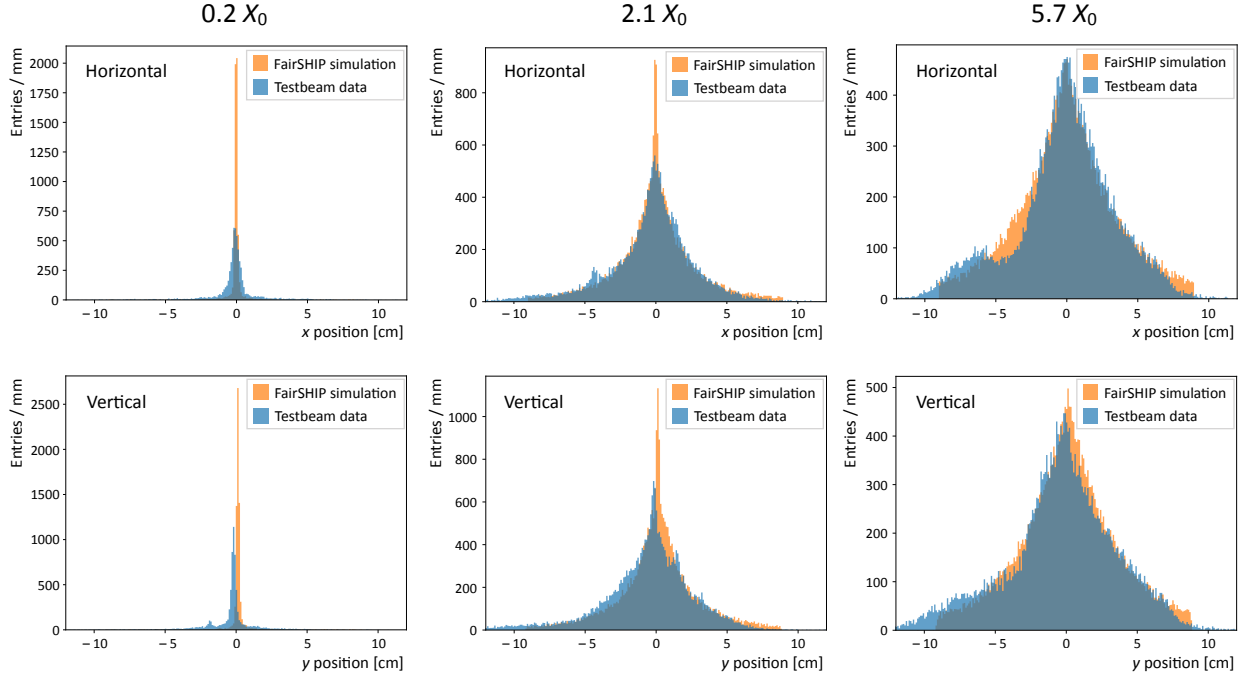


Figure 45: Measured and simulated transverse electromagnetic-shower distribution with 5 GeV/c electrons from the CERN PS at different calorimeter depths. The small discrepancies between simulation and data are mostly due to known issues of the prototype read-out.

3.3 Common detector electronics and online system

The design of the SHiP front-end electronics and readout system is characterised by a relatively small data throughput, no radiation to the electronics, and mostly trivial powering and cooling. The complexity lies in the collection of data from a relatively high number of channels spread out over a very large detector, and in the event building with a very wide range of times-of-flight.

Figure 46 shows an overview of the electronics and readout system. The system has two main subsystems: the control distribution, data transport and concentration (CTC) system; and the timing and fast control (TFC) system. Downstream of the front-end (FE) electronics, the system is composed of cascaded FE concentrators which fan-in and fan-out the CTC and the TFC networks. The FE links are based on 4 LVDS copper pairs carrying physics data at 400 Mbits/s, 40 MHz clock, fast commands and slow control at 40 Mbits/s, and status monitoring at 40 Mbits/s, respectively. Fig. 47 shows a photo of a prototype of the FE concentrator. Downstream of the FE concentrator chain of each subsystem (called partition), the last concentrator is interfaced with a front-end host (FEH) computer for data readout, slow control and monitoring, and with the TFC master for the clock and synchronous commands, as shown in Fig. 46. The design strategy is to base the system as much as possible on FPGAs, including the FE electronics.

The architecture does not comprise a hardware trigger. The FEH computers format the data and forward them to the event filter farm (EFF). For every SPS cycle, a computer in the EFF is assigned to collect the partition data, to extract the physics events candidates and to build the events. The EFF performs reconstruction and event triggering after the

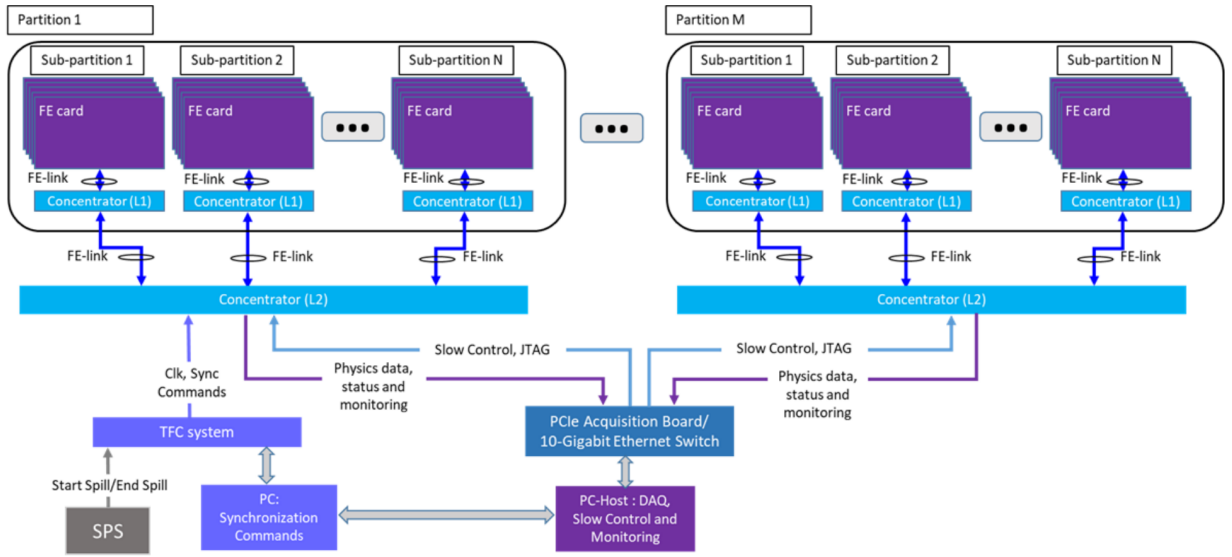


Figure 46: Global scheme of the SHiP electronics and readout system.



Figure 47: Prototype of the SHiP FE concentrator board.

final event building with data from complete SPS cycles. The FEH and EFF computers are based on commodity PCs.

From the study during the CDS phase, it was estimated that about 300 concentrator boards will be required together with a total of 25 DAQ links, 12 FEH and 42 EFF computers. Due to the reduction in size of the detector in ECN3, this is expected to be slightly less but it will only be updated in the early phase of the TDR studies.

4 Physics performance

4.1 FIP decay search performance

Given that SHiP is designed as a discovery experiment with the goal of detecting hidden sector particles in the low invariant mass region, the selection strategy implemented is characterised by a set of broad and loose criteria, outlined in Table 3.

It is crucial to differentiate between fully and partially reconstructed signals. Fully reconstructed signals are those in which all decay products are entirely reconstructed, exemplified by $N \rightarrow \pi^\pm \mu^\mp$ or $A', S \rightarrow \mu\mu$. Partially reconstructed signals involve cases where some decay products are not fully reconstructed, as in $N \rightarrow \mu\mu\nu$.

Criterion	Requirement
Track momentum	$> 1.0 \text{ GeV}/c$
Track pair distance of closest approach	$< 1 \text{ cm}$
Track pair vertex position in decay volume	$> 5 \text{ cm from inner wall}$ $> 100 \text{ cm from entrance (partially)}$
Impact parameter w.r.t. target (fully reconstructed)	$< 10 \text{ cm}$
Impact parameter w.r.t. target (partially reconstructed)	$< 250 \text{ cm}$

Table 3: Pre-selection criteria used for the background rejection and the sensitivity estimates in the analysis of FIP decays.

These two signal categories exhibit experimental differences, most notably in terms of the directionality of the reconstructed vertex towards the target. This characteristics is illustrated in Figure 48, which presents the impact parameter distributions for both signal types, as well as for the muon and neutrino-induced backgrounds. The broader impact parameter distribution of the partially reconstructed signals necessitates the different cuts outlined in Table 3.

Even though purely focusing on fully reconstructed signals would have negligible impact on the sensitivity to the benchmark models, attention was primarily put on the partially reconstructed modes when studying the selection. This is because partially reconstructed signals provide a reliable representation of general models with demanding experimental signatures. In other words, demonstrating that the experiment is efficiently coping with partially reconstructed signals means that it is capable of handling a wider array of signatures.

Another notable aspect of partially reconstructed signals is their utility in model differentiation. Recognising as many decay possibilities of a model as possible is crucial for distinguishing between models, and subsequently increasing confidence in the event of a discovery. For instance, in the case of HNLs, detecting a small number of events with partially and fully reconstructed modes would suffice to distinguish them from other models. This principle of discrimination, using a small number of events, is not exclusive to HNLs. It can also be applied to dark photons and dark scalars. This is because their respective branching ratios to SM particles are determined by a singular parameter: the mixing angle with the corresponding SM boson. This ability to draw on a limited number of events to discern different entities significantly expands the detection and differentiation capacities of the SHiP experiment, ensuring a broader and more nuanced exploration of dark sector particles.

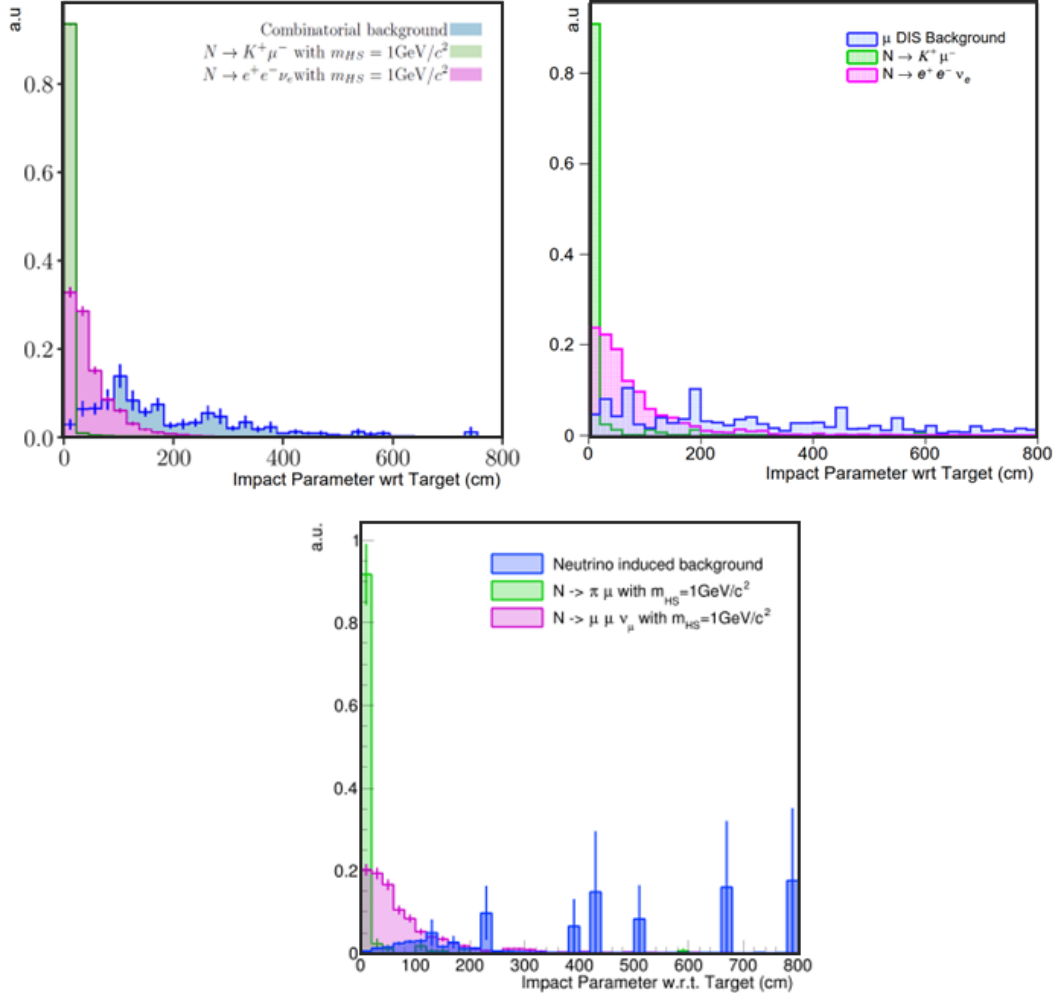


Figure 48: Distribution of the impact parameter at the target for fully and partially reconstructed signal, compared to combinatorial (left), muon DIS (right) and neutrino DIS (bottom) backgrounds.

Some areas of the phase space of certain models can only be explored using partially reconstructed signals. A notable example is HNLs with strong mixing to tau neutrinos.

Moreover, the selection criteria are purposefully loose. While a signal-based selection training could significantly enhance background rejection for any particular signal, the current approach offers safety margin.

Veto detectors are particularly vital for background suppression, as they ensure sensitivity to partially reconstructed signals. They are essential for redundancy in the selection criteria and for directly measuring the level of background in the experiment, since the veto cuts factorise with most kinematic cuts. This is critical for asserting a discovery in the case the experiment only observes a few events.

The muon-induced hit rate in the SBT, composed of both muons and electromagnetic debris, is substantial, reaching approximately half a GHz. Employing a simplistic global veto would have an important impact on the signal efficiency. However, implementing a cut on the energy deposit in individual SBT cells of 90 MeV reduces the rate to approximately

3 MHz (see Figure 49(top)). When vetoing with the full SBT detector, this approach results in a 26% inefficiency for the partially reconstructed signal rate(Figure 49(bottom)). Aiming at increasing the efficiency for the partially reconstructed signals, alternative veto criteria were explored that yield higher efficiency with this signal type. The studies indicate that exploiting the time and spatial resolution of the SBT, and the correlation with the reconstructed signal candidate, all backgrounds can be vetoed with a few percent inefficiencies for partially reconstructed signals.

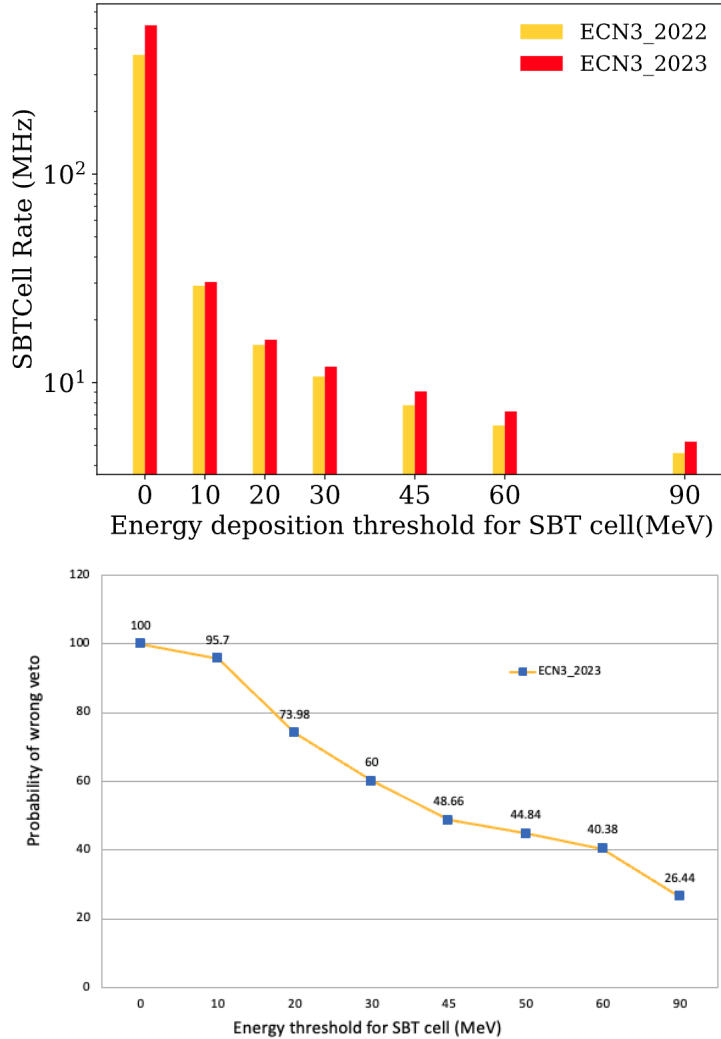


Figure 49: Energy deposit as a function of the energy threshold in the SBT (top), signal inefficiency as a function of the energy threshold in the SBT (bottom).

The background studies are described in detail in Section 4.2.1 and 4.2.2, but an overview of the anticipated background for 6×10^{20} PoT, equivalent to 15 years of nominal running, is presented in Table 4. The fact that such a low background level can be achieved with the inclusive selection gives confidence that the background can be kept at a negligible level even up to $\sim 10^{21}$ PoT.

The above-outlined selection not only enables an effective exclusion of the backgrounds,

Background source	Expected events
Neutrino DIS	< 0.1 (fully) / < 0.3 (partially)
Muon DIS (factorisation)	$< 5 \times 10^{-3}$ (fully) / < 0.2 (partially)
Muon combinatorial	$(1.3 \pm 2.1) \times 10^{-4}$

Table 4: Expected background for 6×10^{20} PoT, equivalent to 15 years of nominal operation.

but also ensures a broad inclusivity with respect to different forms of long-lived particle decays in the fiducial volume. This broad inclusivity safeguards maximum sensitivity in the FIP searches, without compromising on the possibility of accommodating novel models that could be proposed in future scenarios.

Underpinning the studies of SHiP's sensitivity are six benchmark models [175], which have been calculated to provide a representation of generic FIP models: heavy neutral leptons (HNLs), dark scalars mixing with the Higgs boson, dark photons, and ALPs coupled to photons, fermions, or gluons (see also [158] for the description of the phenomenology of these models used in the calculations). The 90% CL sensitivities for the up-to-date ECN3 design are showcased in Figure 50. The sensitivities have been computed for $N_{\text{PoT}} = 6 \cdot 10^{20}$, and using the selection parameters provided in Table 3, with the help of the tool SensCalc [158], which is based on a semi-analytic method for the calculations of the number of events. The comparison of the sensitivities obtained using this tool with FairShip simulations for the models of heavy neutral leptons and dark photons shows an excellent agreement.

Given that, at the lower bound of the sensitivity, the signal yield scales with g^4 , where g is the coupling of feebly interacting particles to the SM particles, and that SHiP operates as a < 1 -event background experiment, the anticipated upper limit for 90% confidence level (CL) is close to the 3σ sensitivity.

Compared to the ECN3 design considered in the LoI [85], the current decay volume and spectrometer have smaller transverse dimensions ($S_{\text{spectrometer}} = 4 \times 6 \text{ m}^2$ vs $4 \times 8 \text{ m}^2$). The decrease of the transverse size is partially compensated by the smaller distance from the target to the decay volume ($l_{\min} = 33 \text{ m}$ vs 38 m). As a result, for the new configuration, the decrease in the geometric acceptance, and hence the event yields, is limited by the decrease of the solid angle covered by the detector $\Omega_{\text{det}} = S/l_{\min}^2$ and does not exceed a factor of 0.8. The decrease is smaller if the FIPs are predominantly produced in the far-forward direction, such as dark photons. The shorter distance to the decay volume slightly improves the sensitivity to short-lived FIPs. Namely, the upper bound of the sensitivity scales as $g_{\text{upper}}^2 \propto l_{\min}^{-1}$, and hence the new configuration may probe 1.2 times larger couplings of short-lived FIPs.

Figure 50a shows the sensitivity curve for HNLs, assuming the benchmark ratio between the three HNL mixing angles to be $|U_e|^2 : |U_\mu|^2 : |U_\tau|^2 = 1 : 0 : 0$. HNL signal events were generated over a range of masses and mixing parameters, $|U_{e,\mu,\tau}|^2$, using the SM electron, muon, and tau neutrinos as inputs. The main production channels of HNLs above the kaon threshold are two- and three-body decays of D, B mesons. HNL decays into various final states, many of each contain at least two charged particles, were modeled using the HNL branching fractions from [81].

Figure 50b shows the sensitivity to dark scalars mixing with the SM Higgs. The scalars may be produced by decays of B mesons and sequentially decay into pairs of charged or neutral particles. For the description of the dark scalar production we consider exclusive

decays $B \rightarrow S + X_{s/d}$ from [23], where $X_{s/d}$ are resonances including an s/d quark.

Three distinct production mechanisms of dark photons were examined to gauge sensitivity, focusing solely on the primary proton interactions. Dark photons of masses below $0.9\text{ GeV}/c^2$ can mix with photons from decays of neutral mesons π^0, η, η' . Proton interactions can also lead to the emission of a dark photon via a bremsstrahlung process, which dominates for dark photon masses in the range $0.4\text{--}2\text{ GeV}/c^2$. Above $2\text{ GeV}/c^2$, quark-antiquark annihilation becomes the main production mechanism of dark photons. The combined sensitivity from these three production modes is presented in Figure 50c, accounting for decays to both leptons and hadrons.

SHiP has also explored the sensitivity to axion-like particles (ALPs) using models with exclusive coupling to photons, fermions, and gluons as benchmarks, as seen in Figure 50d, e, and f, respectively. Depending on the coupling, these particles may be produced by the Primakoff scattering of secondary photons, mixing with pseudoscalar mesons, or decays of B mesons in a similar way to dark scalars. The decay palette consists of a pair of SM fermions, photons, or hadrons. For the ALPs decaying solely into photons, the sensitivity requires the ECAL's ambitious angular resolution to reconstruct the vertex and manage backgrounds from electromagnetic processes and neutrino interactions in the ECAL itself.

Beyond the benchmark models utilised for the experiment's optimisation and sensitivity evaluation, SHiP embodies a versatile platform for investigating the dark sector in the $\text{MeV}/c^2\text{--GeV}/c^2$ range. As such, it is sensitive to other models, such as the HNLs coupled predominantly to the muon or tau flavours, $B - L$ mediators [17], and dark scalars with non-zero trilinear couplings, see Figure 51.

One of the unique strengths of the SHiP experiment is its capacity to make signal measurements in the event of a discovery, which aids in model discrimination. For some models, it can even yield insights in cosmology. For example, in Ref. [15], it was demonstrated that for a region of parameter space (see Figure 52(top-left)), which is roughly an order of magnitude below current limits, SHiP could amass sufficient events to ascertain the nature (Dirac or Majorana) of HNLs and measure the mass splitting between HNLs (see Figure 52(top-right)). This latter parameter is crucial for cosmology, as it may allow inferences about the compatibility with models that explain the baryon-antibaryon asymmetry in the Universe. Figure 52 (bottom) shows that SHiP has the potential to test the compatibility of HNLs with the active neutrino oscillation pattern. Notice that this region of parameter space is far below the limits that any proposed experiment can explore.

Currently lepton identification is not used in the signal selection, but provides an additional handle with partially reconstructed signals if necessary. To date, hadron identification has not been foreseen. Hadron identification can only prove beneficial in the event of a discovery, where it can assist in distinguishing between similar signal models. Moreover, in vast portions of the parameter space not accessible to any proposed experiment, and where SHiP is projected to observe more than 100 events, the invariant mass itself becomes a valuable tool for differentiating between different modes. This concept is illustrated in Figure 53, which displays the invariant mass of $S \rightarrow \pi\pi$ for a variety of mass hypotheses.

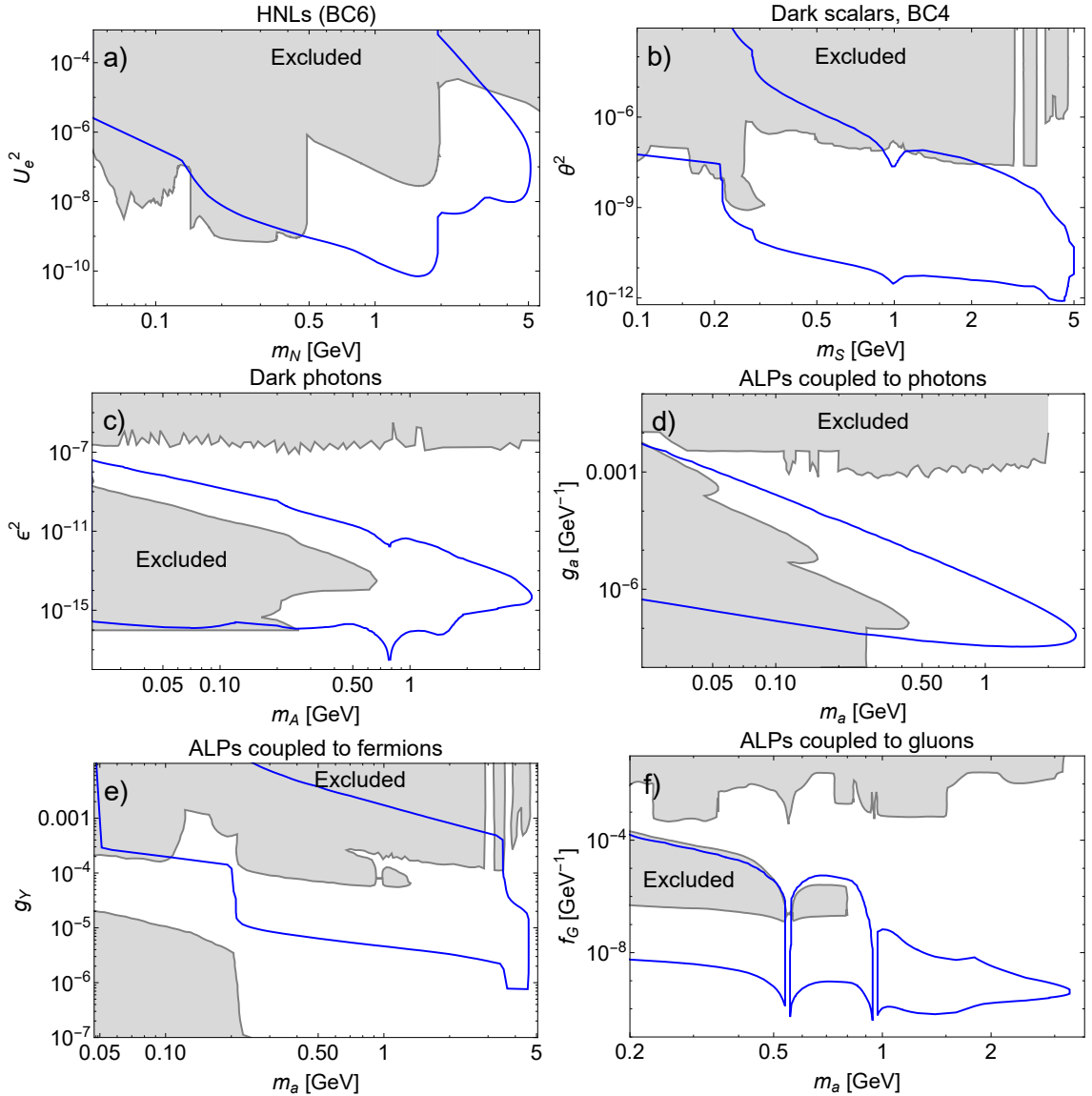


Figure 50: SHiP’s sensitivity in ECN3 for different FIPs: a) HNLs coupled to the electron neutrino flavour, b) dark scalars mixing with the Higgs boson and with $\text{Br}(H \rightarrow SS) = 0$ (BC4), c) dark photons, and axion-like particles coupled to d) photons, e) fermions, and f) gluons. All plots are based on 6×10^{20} PoT, and limits correspond to 90% CL, translating to 2.3 events in the absence of background. Regions shaded in grey are excluded by past and current experiments. See text and Refs. [158, 1] for the description of the phenomenology of the FIPs and details of the sensitivity calculations. The dark scalar production is computed by considering exclusive decays $B \rightarrow S + X_{s/d}$ from [23], where $X_{s/d}$ are resonances including an s/d quark.

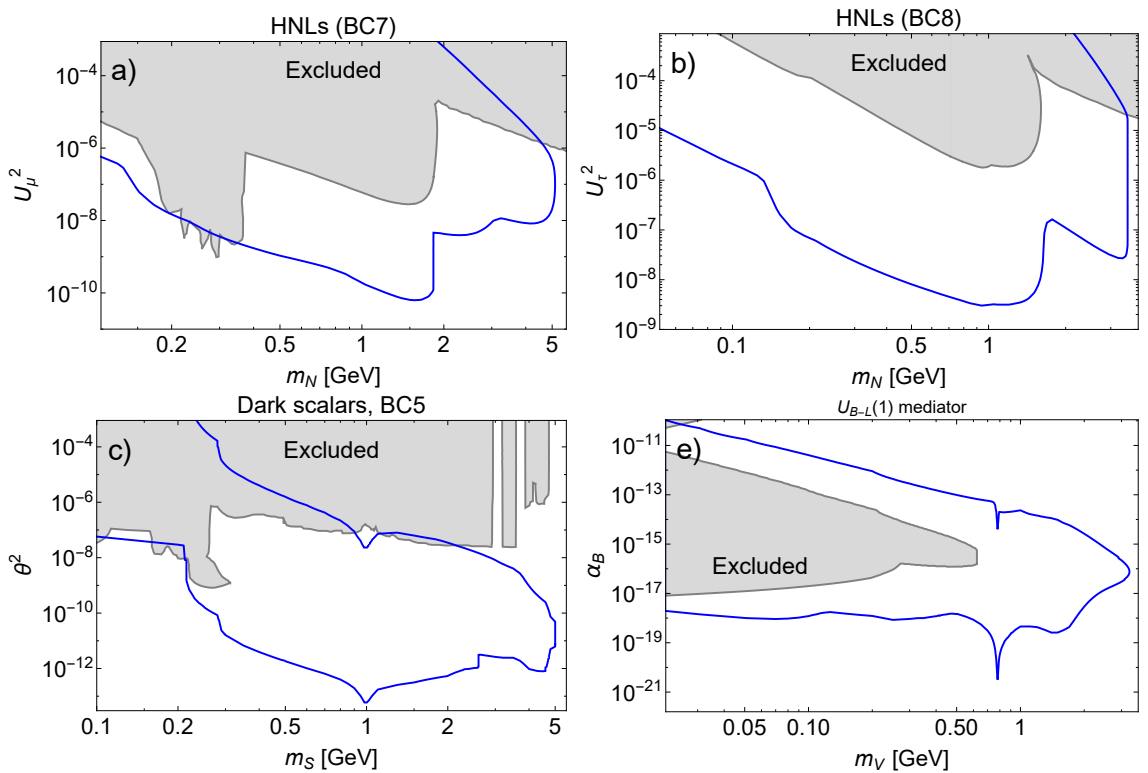


Figure 51: SHiP's sensitivity in ECN3 for different FIPs: HNLs coupled to the muon a) or tau b) neutrino flavour, c) dark scalars mixing with the Higgs boson and with $\text{Br}(H \rightarrow SS) = 0.01$ (BC5), d) and $U(1)$ mediator coupled to the anomaly-free combination of the baryon and lepton currents $B - L$. The description of the figure is the same as in Figure 50,

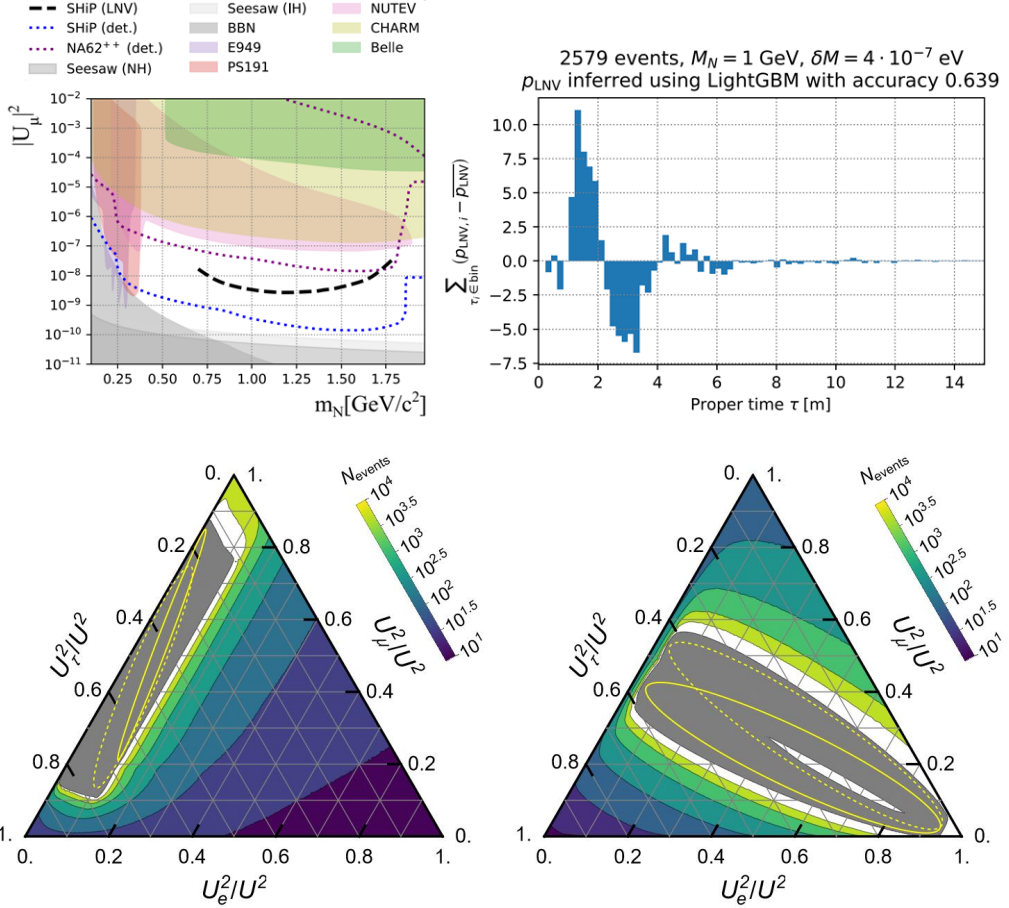


Figure 52: The figure showcases SHiP’s ability to accumulate data on HNL properties, considering models with two quasi-degenerate HNLs that may be responsible for neutrino oscillations. The top-left plot highlights the area where SHiP can concurrently differentiate between Dirac and Majorana nature HNLs and measure the mass splitting through the HNL oscillations. The oscillation of HNLs is represented in the top-right image. The bottom graphs illustrate the potential of using HNL event data to cross-check their compatibility with active neutrino oscillation patterns. For an HNL with a specific mixing pattern, the plots show the number of events sufficient to conclude that the HNL cannot explain the normal (left) and inverted (right) hierarchy of neutrino masses. The gray areas are regions in the U_{α}^2/U^2 parameter space, consistent with the assumption of two quasi-degenerate HNLs with mass $\sim 1.5 \text{ GeV}/c^2$ that provide the correct values of the active neutrino oscillation parameters, including the experimental uncertainties from [159]. The two yellow ellipses correspond to the two likelihood minima in the $(\theta_{23}, \delta_{\text{CP}})$ -plane, while the active neutrino Majorana phase was varied in the $[0, 2\pi]$ range.

4.2 FIP decay search background analysis

4.2.1 Muon-induced background

The muon-induced background can be separated into two primary categories:

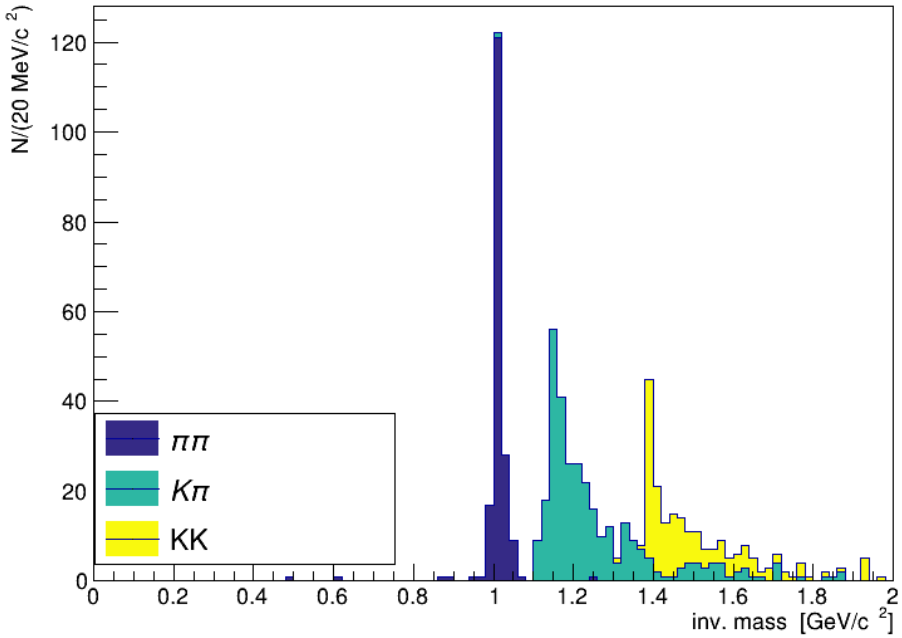


Figure 53: Invariant mass distribution of $S \rightarrow \pi\pi$ for the correct mass hypothesis and for $\pi \rightarrow K$ mis-identification.

Muon deep inelastic scattering background

In this case, muons interact inelastically with the material of the detector or the surrounding infrastructure. These DIS interactions yield V^0 's but also, more importantly, generate false V^0 's due to random track combinations originating from the same DIS interaction. Usually, these interactions produce around ten particles. Because the energy transfer involved is small, DIS interactions result in energetic products that align with the direction of the incoming muon. Consequently, the muon DIS background is primarily dominated by interactions occurring close to the fiducial volume.

For 6×10^{20} protons on target, approximately 2×10^{10} muon DIS interactions are expected near the fiducial volume. After pre-selection, about 6000 background events are expected for fully reconstructed signals and 2.7×10^5 for partially reconstructed signal.

The combined implementation of the UBT and SBT vetoes significantly curtails the muon DIS background to a virtually negligible level. To enhance our statistics, we apply factorisation between the probability of the veto implementation and the probability of rejecting a reconstructed candidate. Given the limited statistics generated specifically for the latest SHiP configuration, we calculate a conservative upper limit for the combined veto suppression factor of 8×10^{-7} . This leads to upper limits of 5×10^{-3} events for fully reconstructed signals and 0.2 events for partially reconstructed signals per 6×10^{20} protons on target as worst-case estimates.

Muon combinatorial background

This background arises when two opposite-sign muons within the same proton spill appear to form a vertex and point back to the target.

The total expected rate of muons in the spectrometer with momentum $p > 1 \text{ GeV}/c$, either directly entering the HSDS fiducial volume or via back-scattering in the cavern, and satisfying the basic track quality (sum of hits in all tracking stations $ndof > 25$, and track fit $\chi^2/ndof < 5$), is $\sim 12 \text{ kHz}$. This results in 1.08×10^{15} possible track pairs within the 1 s spill windows in 6×10^{20} protons on target, not considering opposite-charge pairing.

The pre-selection cuts yield a rejection power of 3.6×10^{-3} . Assuming a flat time structure for the 1 s proton spills, the time coincidence of the pairs of muons in a time window of 340 ps, corresponding to over 2.5 times the time resolution of the HSDS timing detector, provides a rejection of 3.4×10^{-10} .

Implementing the veto from the SBT and UBT suppresses the background by a factor 9.8×10^{-7} . Consequently, the muon combinatorial background is anticipated at a level of 1.3×10^{-3} events for 6×10^{20} protons on target.

4.2.2 Neutrino-induced background

Just like muon DIS background, the primary source of neutrino-induced background arises from neutrino DIS interactions in the vicinity of the fiducial volume. To mitigate irreducible background resulting from neutrinos interacting with air molecules inside the fiducial volume, the decay vessel is maintained at a vacuum level below 10^{-2} bar . The major remaining contributors to neutrino-induced background stem from interactions with the decay volume's wall (about 50%), the liquid scintillator (around 25%), and the SND (approximately 10%).

In this study, a large sample of neutrino interactions were generated. In total, around 5×10^7 interactions are predicted for 6×10^{20} protons on target.

By applying the pre-selection and the veto criteria in tandem with the UBT and SBT, fewer than 0.1 background events are expected for fully reconstructed signals, and around 21 background events for partially reconstructed signals for 6×10^{20} PoT. As shown in the CDS, these events originate from γ conversion, and can be safely reduced to a negligible level, < 0.3 events in 6×10^{20} , by applying an invariant mass cut of $m > 0.15 \text{ GeV}/c^2$. Alternatively, these events can be removed by having tighter cuts on the fiducial volume.

4.2.3 Studies with He-filled decay volume

To mitigate irreducible backgrounds resulting from neutrino scattering in the air, the experiment is engineered to function with an approximate vacuum of 10^{-2} bar in the decay volume. Running the experiment at atmospheric pressure could lower its construction cost and simplify the operation of the detector. In particular, it would allow using of a lighter structure for the decay volume, thereby reducing muon and neutrino interactions. A significant advantage would come from avoiding the need to keep the main tracking system in vacuum, dramatically simplifying the design of the spectrometer section.

Owing to these considerations, the feasibility of operating with helium at atmospheric pressure was explored. A sizable sample of neutrino interactions in helium (1.6×10^6) was produced. Figure 54 shows the region of the decay volume where neutrino interactions

have been generated. From this sample, 25 100 signal candidates were derived. An updated selection process, incorporating particle identification (PID) requirements and vetoes allow decreasing the background to 0.6 expected events for fully reconstructed signals, and ~ 1 background events for partially reconstructed signals per 6×10^{20} PoT.

These preliminary findings indicate that the 1 atm helium option could be a viable choice. However, further investigations are necessary. An extensive examination of the background and the implementation of this option fall beyond the scope of this proposal. It will be addressed in the first phase of the work towards TDR, pending the approval of the experiment.

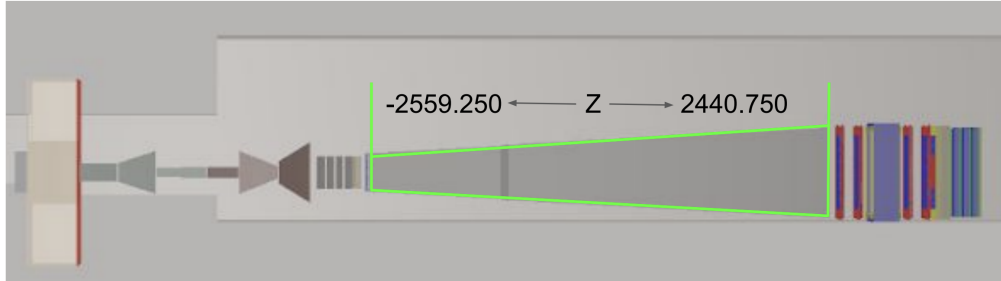


Figure 54: Schematic view of the location where neutrino interactions were generated in order to study the background with the decay volume under helium at 1 atm.

4.3 Scattering-signature search performance

The Scattering and Neutrino Detector (SND) at SHiP offers a powerful opportunity to detect sub-GeV light dark matter (LDM) signatures produced in a variety of dark portals coupled to the SM. Examples include LDM production from mediators coupled to anomaly-free currents – EM, and different combinations of the lepton and baryon currents. In Ref. [44] the sensitivity of the SHiP experiment to LDM χ , coupled to the SM via dark photons A' , was calculated in the ECN4 configuration. In the following section we report the updated sensitivity study based on the ECN3 configuration and the associated changes in the LDM signal and background estimates.

Following the analysis strategy described in Ref. [44], the explored signatures are focused on the LDM elastic scattering off electrons. Elastic and deep-inelastic signatures off nucleons are not considered here. Hence, the sensitivity estimates can be assumed conservative, leaving room for future studies to further extend the discovery potential of the experiment.

The SHiP experiment probes the existence of LDM particles by detecting the electromagnetic shower developing from its elastic scattering on the electrons of the SND LDM/neutrino target. The SND detector, consisting of an alternation between emulsion cloud chamber (ECC) bricks and electronic detector planes (Section 3.1), acts as a sampling calorimeter together with tracking capability at micro-metric position accuracy and milli-radian angular resolution. This configuration allows crucial topological discrimination between the LDM signal and the neutrino background.

Neutrino events with only one reconstructed outgoing electron at the primary vertex constitute the background in the searches for $\chi e^- \rightarrow \chi e^-$ processes. The GENIE Monte Carlo generator, interfaced with FairShip and with the updated SHiP configuration in ECN3,

	ν_e	$\bar{\nu}_e$	ν_μ	$\bar{\nu}_\mu$	all
Elastic scattering on e^-	52	27	64	42	185
Quasi - elastic scattering	-	9			9
Resonant scattering	-	-			-
Deep inelastic scattering	-	-			-
Total	52	36	64	42	194

Table 5: Estimate of the neutrino backgrounds in the search for LDM scattering off electrons with the SND detector at ECN3, for an integrated proton yield of 2×10^{20} PoT for comparison with the original proposal at ECN4.

was used to produce full simulation and to provide an estimate of the expected background for 2×10^{20} PoT, for comparison with the CDS study.

The neutrino background can be suppressed by exploiting the difference in the kinematics. Following Ref. [44], events with electron energy $E_e \in [1, 5]$ GeV and electron scattering polar angle in the lab frame $\theta_e \in [10, 30]$ mrad were selected. The resulting background estimates for the different categories of neutrino interactions for 2×10^{20} PoT are reported in Table 5. Background contributions arise exclusively from topologically irreducible sources, *i.e.* $\nu_e(\bar{\nu}_e)$ elastic and $\bar{\nu}_e$ quasi-elastic scattering ($\bar{\nu}_e p \rightarrow e^+ n$).

Setup	$\frac{z_{\text{to_det}}}{m}$	$\frac{\Delta x \times \Delta y}{m^2}$	$\frac{\Delta z_{\text{tg}}}{m}$	$\frac{m_{\text{det}}}{t}$	$\frac{A_{\text{tg}}}{Z_{\text{tg}}}$	N_{bg}
ECN4	38	0.9×0.75	1.	8	2.53	230
ECN3	25	0.4×0.4	1.	3	2.5	194

Table 6: Comparison of the relevant parameters of the SND configurations at ECN4 and ECN3: the distance from the dump to the beginning of the detector, the transverse dimensions of the detector, the effective length of the LDM/neutrino target inside the detector, the overall detector mass, the mass number/charge ratio of the target, respectively. The last column shows the expected mean number of neutrino background events for 2×10^{20} PoT for comparison with the original proposal at ECN4.

The SND configuration at ECN3 has smaller dimensions and the LDM/neutrino target is based on tungsten instead of lead. The comparison between the configurations is shown in Table 6.

With the re-analysed background levels, the ECN3 sensitivity can be obtained from the ECN4 sensitivity by simple rescaling. In the plane $Y - m_\chi$, where $Y = \epsilon^2(m_\chi/m_V)^4 \alpha_D$ with ϵ, α_D being the couplings of the dark photon to the SM and χ particles to dark photons, the lower bound of the sensitivity scales as $Y_{\min} \propto \sqrt{\frac{A_{\text{tg}}}{Z_{\text{tg}}} \frac{z_{\text{to_det}}^2}{m_{\text{det}}} \sqrt{N_{\text{bg}}}}$, where the meaning of the parameters is explained in Table 6. Based on this scaling, the ECN3 sensitivity is increased by 30% with respect to ECN4, mainly thanks to the three times larger number of the protons on target. The ECN3 sensitivity for 6×10^{20} PoT is shown in Figure 55(left).

Similarly, the sensitivity to millicharged particles can be obtained. However, unlike the case of the LDM, rescaling is not possible since there is no sensitivity computed for the configuration at ECN4. Therefore, full signal yield calculations and background analysis are

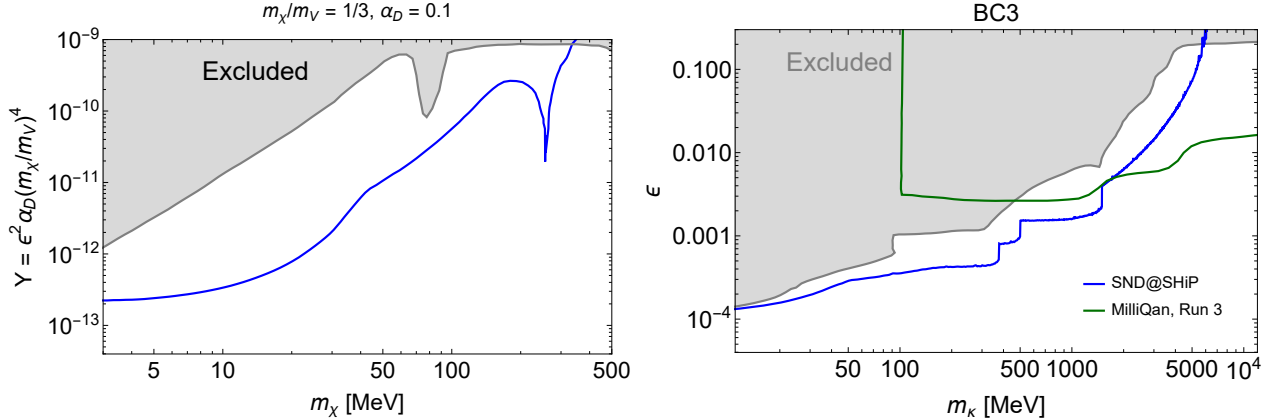


Figure 55: The performance of the SND in exploring various FIPs via the signature of elastic scattering off electrons for $6 \cdot 10^{20}$ PoT. Left: 90% CL sensitivity to scalar LDM χ coupled to dark photons A' assuming the mass ratio $m_\chi/m_{A'} = 1/3$ and the coupling $\alpha_D = g_{\chi A'}^2/4\pi = 0.1$. The sensitivity has been obtained by determining the background in the ECN3 setup with full simulation and then rescaling the sensitivity of the old SND configuration at ECN4 (see text for details). Right: 90% CL sensitivity to millicharged particles.

needed. The background analysis has been performed in a way similar to the LDM case [44] by finding the optimal selection of the electron energy recoil and the χ -LDM scattering angle, minimising the background and simultaneously keeping the signal yield maximal. Details of the signal yield calculations and background estimates are given in an upcoming paper [160].

4.4 Neutrino physics performance

The nuclear emulsion technology combined with electronic detectors and the information provided by the SND muon spectrometer and the HSDS spectrometer makes it possible to identify the three different neutrino flavours in the SND detector. The neutrino flavour is determined through the flavour of the primary charged lepton produced in neutrino charged-current interactions. The muon identification is also used to distinguish between muons and hadrons produced in the τ decay and, therefore, to identify the τ decay channel. In addition, tracking in the SND muon spectrometer and in the HS spectrometer will allow for the first time to distinguish between ν_τ and $\bar{\nu}_\tau$ by measuring the charge of the muon in the $\tau \rightarrow \mu\nu\bar{\nu}$ decay channel.

The neutrino fluxes produced at the proton target have been estimated with FairShip, including the contribution from cascade production in the target. The energy spectra of different neutrino flavours are shown in Figure 56(top left), and the integrated yields at the beam dump for 6×10^{20} PoT are shown in the left column of Table 7. The distance of SND from the downstream end of the proton target, together with the compact transverse area of the LDM/neutrino target, reduce the flux within the detector to about 3% for electron and muon neutrinos. The acceptance for the ν_τ component amounts to $\sim 4\%$. The energy spectra of different neutrino flavours within the LDM/neutrino target acceptance are shown in Figure 56(top right), and the corresponding yields are shown in the central column of

Table 7. The number of charged-current deep-inelastic scattering (CC DIS) events in the neutrino target is evaluated by convoluting the generated neutrino spectrum with the cross section provided by GENIE. The expected number of CC DIS in the LDM/neutrino target of the SND detector is reported in the right column of Table 7, and the corresponding energy spectra in Figure 56(bottom).

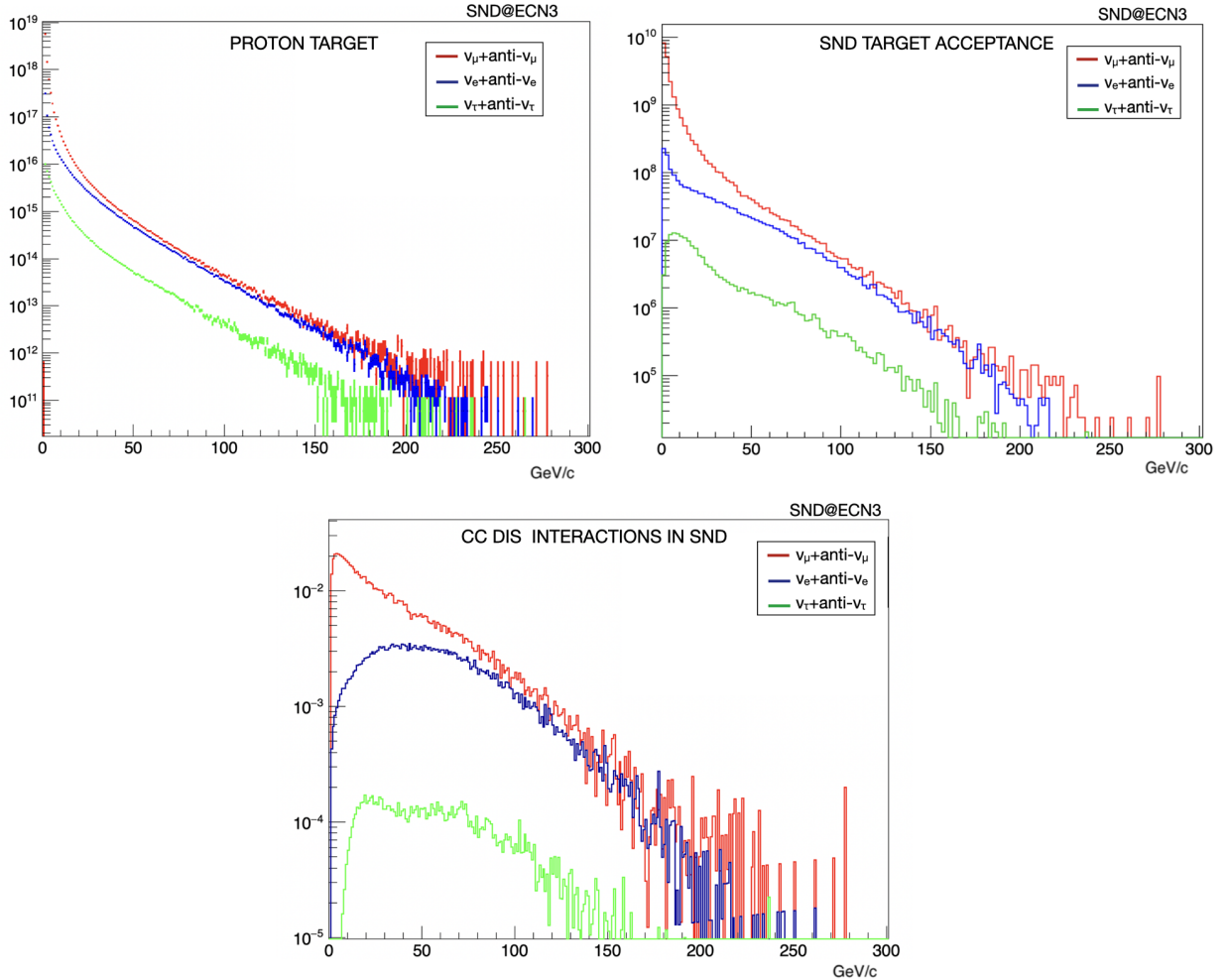


Figure 56: Energy spectra of muon (red), electron (blue) and tau (green) neutrinos at the proton target (top left), in the SND target acceptance (top right) and after their deep inelastic interactions in the SND LDM/neutrino target (bottom). Units are arbitrary.

4.4.1 Muon identification

The muon identification, momentum, and charge measurement is performed by combining the response of the SND with the HDS spectrometer. The left plot of Figure 57 shows the muon momentum spectrum. The portion that reaches the HDS spectrometer ($\sim 24\%$) is highlighted in red, and corresponds to the high energy and low angle muons. The component at lower energy and larger angle is detected by measuring the sagitta in the four tracking

	$\langle E \rangle$ [GeV]	beam dump	$\langle E \rangle$ [GeV]	SND target acceptance	$\langle E \rangle$ [GeV]	CC DIS interactions
N_{ν_μ}	2.6	5.4×10^{18}	8.4	1.5×10^{17}	40	8.0×10^6
$N_{\bar{\nu}_\mu}$	2.8	3.4×10^{18}	6.8	1.2×10^{17}	33	1.8×10^6
N_{ν_e}	6.3	4.1×10^{17}	30	1.3×10^{16}	63	2.8×10^6
$N_{\bar{\nu}_e}$	6.6	3.6×10^{17}	22	9.3×10^{15}	49	5.9×10^5
N_{ν_τ}	9.0	2.6×10^{16}	22	1.0×10^{15}	54	8.8×10^4
$N_{\bar{\nu}_\tau}$	9.6	2.7×10^{16}	32	1.0×10^{15}	74	6.1×10^4

Table 7: Expected neutrino flux for different neutrino flavours at the proton target (left), in the SND target acceptance (middle) and charged-current deep-inelastic interactions in the SND (right), assuming 6×10^{20} PoT.

stations of the SND muon spectrometer. The overall fraction of muons measured with either spectrometers amounts to about 75%.

A schematic drawing of the sagitta measurement is shown in Figure 57(right). After traversing a magnet of length l , the track has a sagitta s

$$s = \frac{l^2}{8r} = \frac{eBl^2}{8p}$$

r being the curvature radius, B the intensity of magnetic field and p the momentum of the particle. The sagitta is determined by two tracking stations before and behind the magnet, measuring the track coordinates x_1 and x_4 and two tracking stations in the middle of the magnet, measuring the track coordinates x_2 and x_3 . From the track coordinates the sagitta is obtained as

$$s = \frac{x_2 + x_3}{2} - \frac{x_1 + x_4}{2}$$

Using the features of the SND muon spectrometer, which has a magnetic field of 1 T over a total length of 3 m and a position resolution of $100 \mu\text{m}$ for the tracking stations, a momentum resolution of better than 10% is obtained for muons in the detector acceptance.

4.4.2 Hadronic energy measurement

The high spatial resolution of the nuclear emulsion allows measuring the momentum of charged particles through the detection of multiple Coulomb scattering in the passive material. The momentum resolution depends on the momentum of the charged particle and the number of emulsion films recording the track in the brick downstream of the neutrino interaction vertex [53]. The left plot of Figure 58 shows the momentum resolution as a function of the momentum p and the number of films npl . A resolution better than 40% can be achieved for the measurement of the charged hadronic component of neutrino interactions for neutrino energies up to 60 GeV/c, as shown in the right plot of Figure 58.

The energy of neutral pions can be evaluated by measuring the energy of the electromagnetic showers produced in the two-photon decays. A resolution of about 40% can be achieved [161].

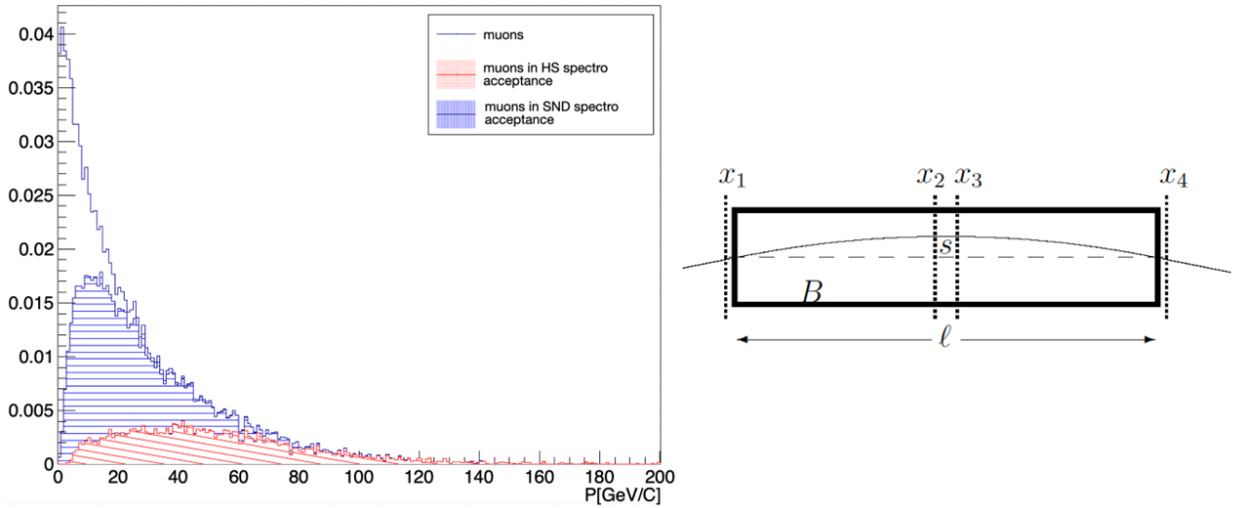


Figure 57: Left: muon momentum distribution at SND, highlighting the portion of the spectrum measured by the HSDS spectrometer (red) and by the SND muon spectrometer (blue). Right: measurement of the sagitta in the SND spectrometer, based of the track coordinates measured in the four tracking stations (x_1, x_2, x_3, x_4).

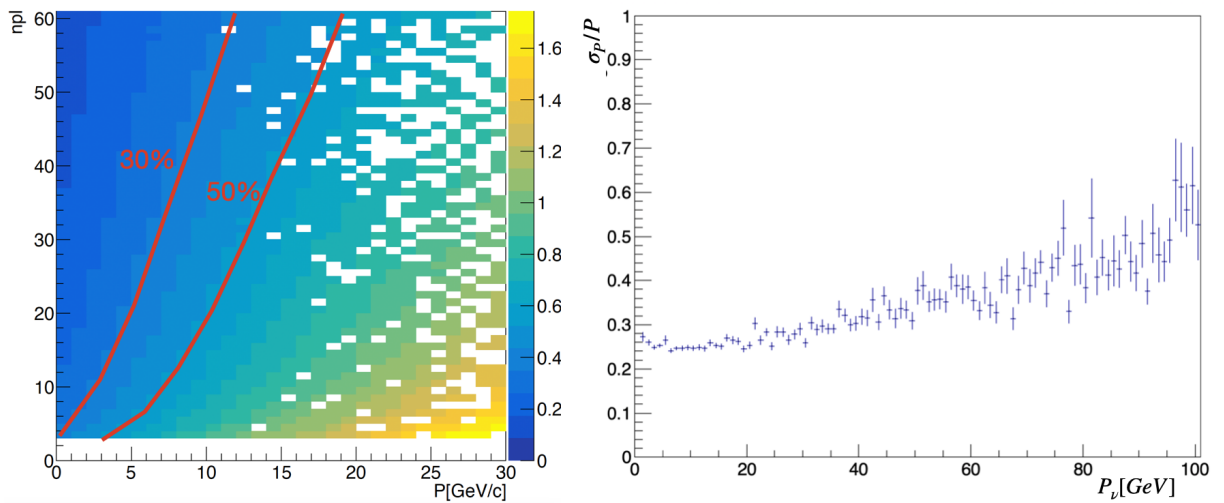


Figure 58: Left: momentum resolution of charged particles as a function of the momentum and the number of emulsion films recording the track, npl , as measured through the MCS in the emulsion brick. Right: momentum resolution of the charged hadronic component of neutrino DIS interactions as a function of the neutrino energy.

4.4.3 Tau neutrino detection

The identification of ν_τ and $\bar{\nu}_\tau$ interactions requires, as a first step, the detection of both the neutrino interaction and the τ lepton decay vertices. Two procedures for the event location and decay search are applied. Neutrino interactions are searched for in the brick within a fiducial volume excluding the regions within 1 mm from the transverse edges of the brick and within 4 mm from the downstream edge of the brick. This results in a geometrical efficiency of approximately 90%.

The location search for neutrino interactions consists of reconstructing a vertex and its three-dimensional position with micrometric accuracy. To identify a neutrino interaction vertex, the presence of at least two tracks with a momentum above 1 GeV/c and a slope $\tan \theta < 1$, having an impact parameter lower than $10 \mu\text{m}$, is required. Tracks having an impact parameter larger than $10 \mu\text{m}$ from the reconstructed neutrino vertex are considered as an indication of a secondary vertex.

The first step in the identification of ν_τ candidates is based on purely topological criteria. Once the primary neutrino interaction vertex has been defined, possible secondary vertices induced by short-lived particles decays are searched for. This is done by a decay search procedure: tracks are defined as belonging to a secondary vertex if the kink angle and the impact parameter of the daughter track with respect to the primary vertex are larger than 20 mrad and $10 \mu\text{m}$, respectively.

The identification of the neutrino flavour is performed through the identification of the charged lepton produced in the charged current interaction with the passive material of the brick. The lepton flavour identification is also important to classify the daughter tracks produced by the τ decay, thus identifying the decay channel, as well as to identify charmed hadrons induced by neutrino interactions. Muon neutrinos are identified through the identification of the muon at the primary vertex.

The efficiencies at the different steps, as well as the overall identification efficiency, are shown in Table 8.

Efficiency	$\tau \rightarrow \mu$	$\tau \rightarrow h$	$\tau \rightarrow 3h$	$\tau \rightarrow e$
Geometrical		0.89		
Location		0.71		
Decay search	0.38	0.37	0.51	0.35
PID	0.32	0.37	0.51	0.31
Charge	0.30	-	-	-

Table 8: ν_τ and $\bar{\nu}_\tau$ efficiencies for different τ decay channels at different steps of the selection.

By combining the overall neutrino CC DIS interaction yield in the LDM/neutrino target and the detection efficiencies shown in Table 8, it is possible to estimate the expected number of ν_τ and $\bar{\nu}_\tau$ interactions observed in the different τ decay channels. For the electronic and hadronic τ decay modes, only inclusive measurements are possible since SND cannot discriminate between ν_τ and $\bar{\nu}_\tau$.

An unprecedented sample of about 53×10^3 detected tau neutrino and anti-neutrino interactions is expected for 6×10^{20} PoT, as reported in Table 9. The separation between ν_τ

and $\bar{\nu}_\tau$ can be performed for about 4000 and 3000 of these interactions, respectively.

Decay channel	ν_τ	$\bar{\nu}_\tau$
$\tau \rightarrow \mu$	4×10^3	3×10^3
$\tau \rightarrow h$	27×10^3	
$\tau \rightarrow 3h$	11×10^3	
$\tau \rightarrow e$	8×10^3	
total	53×10^3	

Table 9: Expected number of ν_τ and $\bar{\nu}_\tau$ signal events observed in different τ decay channels, assuming 6×10^{20} PoT.

4.4.4 Neutrino-induced charm production

The expected charm yield in the neutrino charged current interactions ($\sigma_{charm}/\sigma_{CC}$) was estimated using the GENIE generator. The charm fractions are reported in the right column of Table 10 for electron and muon neutrinos, separately.

In 6×10^{20} protons on target, more than $\sim 6 \times 10^5$ neutrino-induced charmed hadrons are expected, as shown in Table 10. The total charm yield exceeds the statistics available in previous experiments by more than one order of magnitude.

Therefore all the studies on charm physics performed with neutrino interactions can be improved, including studies of channels inaccessible in the past, such as measurement of the double charm production cross-section [162, 163], and the search for pentaquarks with charm-quark content [164]. Charmed hadrons produced in neutrino interactions are also important for investigating the strange-quark content of the nucleon [3]. Figure 59 shows the number of muon neutrino CC DIS events in each bin of the probed 2D region in x and Q^2 for 6×10^{20} PoT.

	$\langle E \rangle$ (GeV)	CC DIS with charm prod	Charm fractions (%)
N_{ν_μ}	57	3.5×10^5	4.4
N_{ν_e}	71	1.7×10^5	6.0
$N_{\bar{\nu}_\mu}$	50	0.7×10^5	3.8
$N_{\bar{\nu}_e}$	60	0.3×10^5	5.3
total		6.2×10^5	

Table 10: Expected CC DIS neutrino interactions with charm production for 6×10^{20} protons on target, and relative charm production yield per electron and muon neutrinos CC DIS interaction.

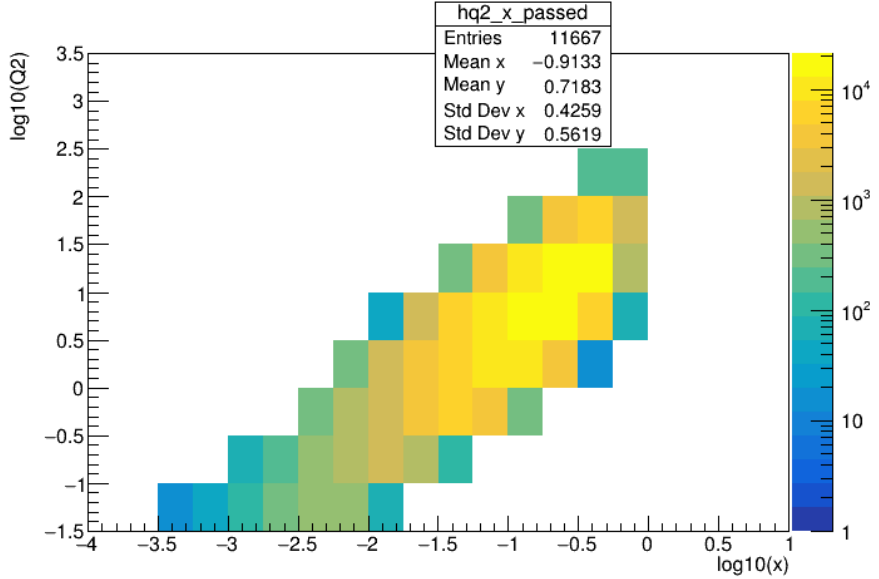


Figure 59: Number of muon neutrino events with charm production reconstructed in SND detector in different bins of x and Q^2 .

4.4.5 Tau neutrino magnetic moment

With more than 50 000 ν_τ CC interactions in the SND, SHiP can significantly constrain the ν_τ magnetic moment.

The presence of a non-zero magnetic moment adds an extra-component to the elastic cross-section for the process $\nu + e^- \rightarrow \nu + e^-$ due to photon exchange, leading to an anomalous increment of the measured value of this cross-section. In this process, the scattering angle in the laboratory frame of the outgoing electron with respect to the direction of the incoming neutrino is limited by kinematic constraints [165]:

$$\theta_{\nu-e}^2 < \frac{2m_e}{E_e}. \quad (1)$$

Therefore, for an electron energy above 1 GeV, $\theta_{\nu-e}$ must be below 30 mrad. This can help suppressing the background formed by events showing the same topology.

The main background sources for this measurement are: (i) neutrino elastic scattering (ES) with electrons of the detector target, (ii) electron neutrino and anti-neutrino quasi elastic scattering (QE) with nucleons of the detector target with non detected outgoing nucleons, (iii) charged current deep-inelastic interactions (CC DIS) of electron neutrinos and anti-neutrinos with nucleons in the detector target with no revealed hadrons in the final state, and (iv) electron neutrino and anti-neutrino resonant processes. In order to take into account the uncertainty on the neutrino interaction position in the detector target, a smearing of the electron angle by 1 mrad was introduced. The GENIE generator was used to estimate the number of expected background events surviving the following selection criteria: only the electron reconstructed in the final state, $E_e > 1$ GeV, $\theta_{\nu-e} < 30$ mrad. The overall contribution from the different background sources amounts to 3×10^4 events, mainly from QE processes.

Denoting the incoming tau-neutrino flux on the detector by Φ_{ν_τ} , N the number of nucleons in the neutrino target, σ^μ the contribution of the non-zero magnetic moment to the cross-section, and the Bohr magneton with $\mu_B = 5.8 \times 10^5 eV T^{-1}$, the number of expected events for a magnetic moment μ_ν is given by:

$$n_{evt} = \frac{\mu_\nu^2}{\mu_B^2} \times \int \Phi_{\nu_\tau} \sigma^\mu N dE$$

Assuming a 5% systematic uncertainty on the neutrino flux, the evidence for a tau neutrino anomalous magnetic moment with a significance of 3σ requires the observation of an excess of about 4000 events over the background. Hence, a region down to a magnetic moment of $9 \times 10^{-8} \mu_B$ can be explored.

4.5 Measurement of charm production with the BDF/SHiP prototype target

The leading systematic error in several of the neutrino measurements comes from the uncertainty on the neutrino flux. This is particularly true for tau neutrinos which are produced in D_s decays. Charm production in proton-proton collisions at 400 GeV was measured with an accuracy better than 10% by the NA27 experiment [166]. A dedicated measurement of the D_s production with the identification of the subsequent $D_s \rightarrow \tau$ decay is being carried out by the NA65 experiment [167]. NA65 expects to reconstruct about 1000 $D_s \rightarrow \tau$ decays in 2.3×10^8 proton interactions with a tungsten target [167]. The data which will become available in the coming years, will narrow down the uncertainty on the tau neutrino flux.

In the long proton target of BDF/SHiP, charmed hadrons are also produced in the hadron cascade in which the most relevant process is proton elastic scattering followed downstream by a deep inelastic scattering with charm production. Simulation studies show that this effect increases the charm yield by more than a factor of two.

In 2018, the SHiP Collaboration successfully carried out a feasibility run aiming at measuring the charm cross-section, including the cascade effect expected at BDF/SHiP. The setup consisted of the 400 GeV/c SPS proton beam impinging on a replica of the BDF/SHiP target, instrumented with nuclear emulsion film. The emulsion films were used for accurate identification of the production and decay vertices of the charmed hadrons. The target was followed immediately downstream by a silicon tracker, providing time stamping of the events reconstructed in the emulsion, and a spectrometer using the CERN Goliath magnet and modules of drift tubes [134]. A muon identification system based on RPCs provided muon identification. In order to limit the track occupancy of the emulsion films, the beam was spread on the emulsion surface ($10 \times 12.5 \text{ cm}^2$) by moving the emulsion detector during the SPS spill. The time stamp of the events reconstructed in the emulsion was relying on the matching between the moving emulsion detector and the silicon tracker [168]. The experiment successfully demonstrated the emulsion reconstruction with track densities up to $4.5 \times 10^4 \text{ cm}^{-2}$ [169].

With the lessons from the feasibility run, the SHiP Collaboration plans to carry on with a full measurement campaign in the future, that would also serve as test bench for the SHiP detectors, and potentially also silicon pixel technology that is being studied as alternative to emulsion in synergy with the ongoing R&D of the SND@LHC experiment. A part of the

campaign will be dedicated to complete the charm-cross section measurement with emulsion and a thin target, and a second part dedicated to accurately determining the factor coming from cascade production by measuring $J/\psi \rightarrow \mu\mu$ production using targets with different depths.

The high statistics accumulated by the experiment will allow defining different control samples such that the detection efficiencies can be evaluated at the level of a percent with data driven procedures. Hence, it is expected that the ongoing and planned measurements should allow narrowing down the uncertainty on the neutrino flux to a few percent, making it comparable with the statistical error of the neutrino measurements at BDF/SHiP.

Precision measurement of the neutrino flux at BDF/SHiP also opens the possibility of precision measurements of the neutrino cross-sections, which is essential for the neutrino oscillation programme worldwide.

5 Road map and detector cost

The work packages for the BDF and the SHiP Technical Design Report (TDR) studies, including the associated resource requirements, were discussed in the CDS reports [84, 83]. The work packages are built on the understanding of the designs developed in the extensive joint studies performed during the six years of the Technical Proposal and CDS phases, which concentrated a large part of the effort on tuning the design of the components to maximise the signal acceptance and minimise the background. The LoI of BDF/SHiP at ECN3 [86] described the initial studies conducted to adopt the experiment to the TCC8/ECN3 experimental area, while this report presents the complete study of the sensitivity at ECN3, including also an option with a superconducting magnet as the first section of the muon shield.

Throughout these phases, all critical components of the facility were studied, analysed and in some cases prototyped. The baseline target system has been through a first validation in a beam test in which the operating conditions of the real target were reproduced [95, 96, 97, 98]. The main challenges are associated with the implementation of the target system and its cooling, and the design and handling of the target complex. Further reduction of the residual dose rate as well as faster thermal dissipation could be achieved through the development of niobium-alloy cladding. An alternative improved target design with increased fraction of tungsten, and less gaps for water cooling, is also under consideration. Three options with helium, nitrogen, or alternatively vacuum have been considered for the target complex vessel that should ensure an inert atmosphere to prevent corrosion and reduce residual gas radio-activation within the target shielding. These need detailed investigations, together with the design of the proximity shielding and services. While the concepts around the handling of the target and the target complex are well developed, the different components involved and the remote handling techniques require detailed design and prototyping.

All of the SHiP detector systems have undergone at least a first level of prototyping and measurements with the prototypes in test beam [117, 84]. A few critical systems have already been in test beam with large-scale prototypes, in particular the SBT, UBT, and the timing detector. The last two are also in operation at other experiments. The performance parameters measured with the prototypes are used in the simulation and background studies to derive the sensitivities of the experiment.

The beam tests have also revealed the main technological challenges to be addressed during the TDR phase. With this information at hand, all major subsystems of the SHiP detector went through conceptual design reviews, with the focus on outlining the work up to TDR, at the end of the CDS phase. The SND@LHC experiment [125], currently installed and operating in TI18 of the LHC, provides further confidence in the SND concept first developed for the OPERA experiment, and then improved within SHiP. Collaboration with SND@LHC is established to pursue the development of the SND detector for BDF/SHiP. Importantly, the synergy between the studies towards an upgraded SND@LHC and towards BDF/SHiP can bring significant innovation to the complementary programmes of both detectors.

The principal technological challenges for the experiment lie in the further development of the muon shield, the decay volume and the spectrometer magnets, and involve mechanics and the full-size production. The new concept of the hybrid muon shield with a superconducting magnet requires a substantial engineering effort, considering options with reduced yoke,

Accelerator schedule	2022	2023	2024	2025	2026	2027	2028	2029	2030	2031	2032	2033
LHC	Run 3				LS3				Run 4			LS4
SPS (North Area)												
BDF / SHiP	Study	Design and prototyping			Production / Construction / Installation			Operation				
Milestones BDF	TDR studies		PRR		CIB							
Milestones SHiP	TDR studies		PRR		CIB							

Figure 60: Implementation timeline for BDF/SHiP in ECN3.

with or without iron core, and a choice between fully enclosing cryostat or a smaller cryostat embedded inside the yoke. It is essential to continue exploring the superconducting option for the spectrometer magnet with the aim to reduce the power consumption and the operational costs. The integration of the SBT and the HSDS spectrometer tracker together with the vacuum vessel is associated with important design challenges that must be addressed early in the TDR phase. With respect to ECN4, the implementation of BDF/SHiP at ECN3 requires reviewing in detail the approach to the detector assembly in the existing halls on the Prevessin site, transport, and the installation of the experiment without the top access that was foreseen in the CDS design.

Considering the options at hand to improve the baseline, the early part of the TDR phase requires addressing major decisions on the strategy for the muon shield, the development path for the spectrometer magnet following the ongoing feasibility studies of the coil concept, the configuration of the PID system, as well as on the helium option, which may potentially lead to a different choice of technology for the HSDS spectrometer tracker technology. This will also reduce the complexity of the spectrometer section and reduce the cost.

In terms of future beam tests, beam time has been allocated at the end of 2023 at the PS for a large scale multi-compartment prototype of the SBT. The plan is to repeat the test in 2024 in order to check for aging effects in the wall reflectivity of the SBT cells. In the coming years before Long Shutdown 3 (LS3, currently scheduled for 2026-2027), the most important beam tests concern the HSDS spectrometer tracker and the particle identification detectors, and the full-ring prototype of the decay volume with the SBT in the final configuration. The physics potential of the neutrino programme at BDF/SHiP can be greatly enhanced by reducing the uncertainties related to the tau neutrino flux, in particular arising from the poor knowledge of the cascade charm production in the long BDF/SHiP target. SHiP plans to continue on the measurement of the charm production, started in 2018 at the SPS with a dedicated setup, and perform a precision measurement of the cascade production with a high-A/Z target of variable thickness and using the J/ψ yield. Depending on scheduling, this setup can also be used to test the pre-production prototypes of some of the detectors.

In the current CERN accelerator schedule, it is likely that certain detector beam tests will have to rely on DESY in 2026. Apart from the charm measurement campaign, there may also be interest in performing a validation run of the final prototype of the muon shield magnets after LS3.

The implementation timeline for BDF/SHiP at ECN3, shown in Figure 60, draws on the findings in the CDS phase and the recent studies related to ECN3, and has been drawn up to make maximum use of the SPS in parallel to the HL-LHC. At the same time, it aims at respecting the technical and resource constraints, and the operating schedule of the CERN beam facilities during the construction. The timeline assumes that the project is approved for

TDR by end of 2023. Given the extensive studies performed during the Technical Proposal and the Comprehensive Design Study phases, followed by the work under the MoU for the continued BDF R&D with focus on ECN3 in 2021-2023, it is expected that Technical Design Reports could be delivered within two and half years for the BDF components, and within three to four years for the SHiP detector, depending on the subsystem. This is compatible with commencing the implementation of BDF/SHiP during LS3. The funding initiatives will be an important driving factor in the ramp-up of the work towards TDRs.

The LS3 for the injectors is a critical ingredient in the timeline since it allows carrying out the work in the beam lines for the upgraded intensity, including the necessary cool-down, before the North Area is expected to be operational for Run 4. It is assumed that decommissioning of the current installations in TCC8 and ECN3 can be done during 2026 and 2027 such that the modifications to the infrastructure can start by the second half of 2027. It is estimated that the detector production and construction will require three to four years. The schedule aims at a short commissioning phase of the facility in 2030, and first year of data taking in 2031.

The LS4, currently scheduled for 2033, presents an opportunity for consolidation, if necessary. As demonstrated in this paper, the facility and the detector are able to continue probing the parameter space of FIPs up to 6×10^{20} PoT which can be achieved in 15 years of nominal operation, and potentially also beyond that towards 10^{21} PoT. This relies on that the SPS is expected to be delivering beams for fixed target physics at CERN after the stop of the HL-LHC, and that, with a proper maintenance and upgrade campaign, it remains available for physics and beam tests also during the preparation of CERN's future large-scale collider. The operational schedule over 15 years offers in this way several unique opportunities for extensions and upgrades of BDF/SHiP, as discussed in Section 6.

5.1 Detector cost

BDF/SHiP's study phases have allowed all subsystems to develop models which specify the requirements in terms of technologies, mechanics, electronics, services and infrastructure. Based on breakdowns of the sub-components of each subsystems, material cost estimates for the TDR phase and the production have been elaborated. The cost of the detector includes the free-standing muon shield, the SND and the HSDS detectors, the magnets, and the associated infrastructure. The cost of the magnetisation of the hadron stopper has been included in the cost of the facility. The estimates initially prepared for the CDS report have been revised according to the new detector configuration and dimensions, and have been updated for 2023 by taking into account inflation. No costs for personnel have been included. As shown in Table 11, the total cost amounts to ~ 51 MCHF. The subsystems marked with a * are considered as part of the common fund. The estimate of the total is considered conservative given that SHiP's cost is dominated by infrastructure and upper estimates have been used for material costs, and that the most expensive options have been included everywhere, i.e. muon shield in hybrid version with SC magnet, decay volume with vacuum, SBT with maximum number of compartments, common electronics and readout with number of channels as in the CDS detector.

The uncertainty on the estimate for each sub-components has been estimated from the level of maturity of the design and from the way in which the cost estimates have been

Item	Production material cost [kCHF]
Muon Shield	11 100
Hadron stopper magnetisation	included in facility cost
Muon shield - SC section*	7 000
Muon shield - NC section*	4 100
Scattering and Neutrino Detector	5 300
Emulsion system, inc. facility tooling	2 400
Target tracker	1 500
Muon spectrometer magnet	1 200
Muon detector	200
Hidden Sector Decay Spectrometer	30 300
Decay volume vacuum vessel + caps*	4 700
Spectrometer vacuum vessel*	3 900
Spectrometer magnet*	6 400
Upstream background tagger	200
Surrounding background tagger	4 700
Spectrometer tracker	4 400
Timing detector	700
Particle identification detectors	5 300
Infrastructure	2 000
Online + offline	2 200
Common electronics and online ^(*)	1 200
Computing	1 000
Total	50 900

Table 11: Breakdown of the updated cost of the SHiP detectors and the muon shield in the hybrid SC/NC option, including infrastructure. The subsystems marked with a * are considered as part of the common fund.

derived in terms of direct quote from manufacturer, scaling from existing design or quote, estimate in collaboration with company, estimate in-house, and best estimate. The level of maturity in the design of the different subsystems varies.

The free-standing muon shield, the vacuum vessel, and the HDS spectrometer magnet are critical common infrastructure items presenting major challenges. In addition, significant effort is required to determine the final configuration and design strategy for the SC magnet in the muon shield, and the viability of the SC technology for the spectrometer magnet. For these reasons, these items are attributed with relatively large uncertainties. A detailed design is only available for the vacuum vessel.

The SND emulsion target system is a well-known concept from the OPERA experiment. All additional features required by the SHiP SND detector, including operating and analysing emulsion with high occupancy, have been tested in the SPS beam test, and more importantly in the SND@LHC experiment. The SND target tracker based on SciFi and the SND muon

spectrometer based on drift tubes are well-known technologies. This significantly reduces the uncertainties for SHiP. With the small dimensions, it is expected that the spectrometer magnet may use normal-conducting coils, or potentially profit from the SC technology under study for the large spectrometer magnet, if that turns out to be sufficiently cost effective.

The UBT based on the MRPC technology has been developed for the R3B S522 experiment at GSI/FAIR (Darmstadt) [140] and is being used in the framework of other projects [170, 171, 172] with similar characteristics, and is therefore attributed with relatively small uncertainties. The LS SBT system is a major system presenting several challenges coming from the performance requirements and the integration in the decay volume. Significant progress has been made recently in the continued R&D, but the system is still endowed with large uncertainties related to the optimal solution for the wall reflectivity and the integration of the liquid scintillator circulation system.

While the spectrometer straw tracker detector is based on technology developed for the NA62 experiment, the large size of the detector presents challenges both with respect to performance, mechanics and integration in vacuum. Consequently, it is attributed relatively large uncertainties. The timing detector is profiting from a concept developed for the BabyMIND experiment. The challenges are mainly associated with the large size, and the required accuracy of the timing calibration. Even though the SplitCal is based on the known technology of scintillating bars and micro-megas, the requirement of di-photon event reconstruction leads to a novel concept which is still in the early R&D phase. The high-precision requirement and the large size introduce important uncertainties. In the revised PID system, the hadron calorimeter active layers are based on the same scintillator technology as the electromagnetic calorimeter, implying that the cost can be evaluated with small uncertainties.

As a result of the considerations above, the final total production cost estimate for the full detector is attributed with a combined uncertainty at the level of $^{+30\%}_{-10\%}$, making it compatible with a Class 3 cost estimate. It is assumed that the uncertainty is at the same level for the TDR material costs.

5.2 Status of the Collaboration

SHiP is currently a collaboration of 33 institutes and 5 associated institutes, in total representing 15 countries, and CERN. A preliminary sharing of responsibilities for the different subsystems of SHiP is indicated in Table 12. The responsibilities cover all key competencies of the projects from R&D and design to the construction and implementation of the equipment, with the exception of the superconducting technologies where SHiP is currently relying on external help. The sharing is primarily based on the interest expressed by the groups, taking into account the expertise, resources and contribution to the ongoing R&D programmes. The assignments cover all sub-tasks that have been required for the optimisation, design and validation of the detector prototypes. Many additional tasks associated with the final design and construction are open to new groups. The final sharing will become subject to negotiation with the corresponding funding agencies after the approval of the experiment. Significant number of groups, not yet part of SHiP, from various countries, including Germany, France, Italy, Netherlands, Sweden, and UK, have expressed interest to join SHiP, pending the approval of the TDR phase. An MoU is expected to be established

during 2024.

The SHiP collaboration considers a significant number of items as "Common Projects", as shown in Table 12, to which all institutes are expected to contribute. However, it is foreseen that each common project is associated with a dedicated group that takes responsibility for leading the project. The relative size and the scheme for contributing to the common fund is currently under discussion.

Sub-projects	Main lead	Involved groups
Muon shield Muon shield*	CERN ³⁰	RAL(UK) ³⁸ , CERN ³⁰ , ++
SND Emulsion system Target tracker Muon spectrometer	Naples(IT) Lausanne(CH) Naples(IT)	LNGS(IT) ¹⁷ , Naples(IT) ^{16,c} , Aichi(JP) ¹⁸ , Kobe(JP) ¹⁹ , Nagoya(JP) ²⁰ , Nihon(JP) ²¹ , Toho(JP) ²² , Gyeongsang(KR) ²³ , Gwangju(KR) ²⁴ , Seoul(KR) ²⁵ , Gyeong Gi-do(KR) ²⁶ , METU(TR) ³³ Lausanne(CH) ³¹ , Siegen(DE) ¹² Bari(IT) ^{13,a} , Naples(IT) ^{16,c}
HSDS Decay vacuum vessel + caps* Spectrometer vacuum vessel* Spectrometer magnet* Upstream background tagger Surrounding background tagger Spectrometer tracker Timing detector Particle identification detectors	Naples(IT) CERN ³⁰ CERN ³⁰ Lisbon(PT) Berlin(DE) Hamburg(DE) Zurich(CH)	Naples(IT) ^c , CERN ³⁰ CERN ³⁰ CERN ³⁰ , ++ Lisbon(PT) ²⁸ Berlin(DE) ⁷ , Freiburg(DE) ⁸ , Juelich(DE) ¹⁰ , Mainz(DE) ¹¹ , Kiev(UA) ³⁹ Hamburg(DE) ⁹ , Juelich(DE) ¹⁰ , Kiev(UA) ³⁹ , CERN ³⁰ Zurich(CH) ³² Mainz(DE) ¹¹ , Bologna(IT) ¹⁴ , Cagliari(IT) ^{15,b} , Bristol(UK) ³⁵ , ICL(UK) ³⁶ , UCL(UK) ³⁷
Online + offline Common electronics and online ^(*) Computing	Orsay(FR)	Orsay(FR) ⁶ , CERN ³⁰ CERN ³⁰ , Copenhagen(DK) ⁵
Subdetector infrastructure, engineering, electronics		Sofia(BG) ¹ , SAPHIR(CL) ² , UNAB-Santiago(CL) ³ , ULS-Serena(CL) ⁴ , Copenhagen(DK) ⁵ , Siegen(DE) ¹² , Leiden(NL) ²⁷ , Belgrade(RS) ²⁹ , Ankara(TR) ³⁴

Table 12: Subsystems and current group responsibilities. The subsystems marked with a * are considered as part of the common fund. For those items, ++ indicates that discussions with new groups are ongoing.

6 Future upgrades and extensions of the facility

The 15-years operational exploitation of ECN3 by BDF/SHiP and the future long shutdowns of the CERN accelerator complex, open opportunities to extend the physics programme of the facility. The sections below outlines a number of possibilities that have been investigated.

6.1 Spill intensity increase

The delivery of 7×10^{13} protons per spill (amounting to 6×10^{19} POT/year) would enable SHiP to collect up to a total of 10^{21} PoT and further extend the physics program, exhausting the experimental potential of all relevant models, as well as probing sterile neutrinos all the way down to see-saw limit, in the MeV/c²-GeV/c² mass range.

Historically, the CERN accelerator complex has already accelerated high-intensity beams in the SPS. The West Area Neutrino Facility (WANF) delivered over 7×10^{19} POT during its 5 years of operation until the end of 1998 via pulsed slow extraction. Most notably, the CERN Neutrinos to Grand Sasso (CNGS) facility operated nominally at close to 4.4×10^{13} ppp, delivering via fast extraction 1.8×10^{20} POT over 5 years of operation until the end of 2012 [82]. A record SPS cycle intensity of 5.3×10^{13} ppp was achieved during a three-week dedicated run for CNGS.

In 2011, a design study was launched for the Long Baseline Neutrino Oscillation (LBNO) experiment. LBNO proposed to exploit the experience gained from CNGS to reach even higher intensity considering a cycle intensity as high as 7×10^{13} ppp. Its conceptual design report [173] comprehensively details the main intensity bottlenecks prior to the LHC Injectors Upgrade (LIU).

Currently, the SPS Fixed Target Proton (SFTPRO) cycle can be operated at close to 4.2×10^{13} ppp for extended periods of time, as was demonstrated during the LHC downtime in the summer of 2022 where an extraction rate of almost 1.2×10^{18} POT/week was established for over four weeks. This extraction rate would extrapolate to over 3×10^{19} POT if maintained for an entire operational year.

A significant increase in intensity to 7×10^{13} ppp would be met by different technical and radiological limits along the entire CERN accelerator chain. Table 13 lists the record and operational cycle intensities and estimated relative beam loss [174] for different stages of acceleration and transfer along the accelerator chain.

In Linac 4 and PSB, there are R&D synergies with other high-intensity requests including from ISOLDE facility where 6×10^{13} ppp is on the horizon. With two PS batches injected into the SPS per cycle, this would be equivalent to pushing the intensity towards 12×10^{13} ppp. In 2022, tests in the PS were already carried out with the successful acceleration and extraction of 3.2×10^{13} ppp, paving the way for tests in the SPS at over 6×10^{13} ppp in the near future. The impact of the increased intensity on the vertical beam quality still needs to be quantified to understand if sufficiently small vertical emittances can be produced and conserved along the accelerator chain to fit inside the limited vertical acceptance of the SPS. Recent developments with the implementation of the barrier-bucket technique [175] has shown promising beam loss reduction on the PS extraction septa during the Multi-Turn Extraction (MTE) from the PS from 4 % to below 1 %. Transmission losses increase significantly during PS-to-SPS transfer at an intensity over 2×10^{13} ppp/batch delivered from the

Accelerator (process)	Record	Operational	Operational	Known limitations
	Intensity [$\times 10^{13}$ ppp]	Intensity [$\times 10^{13}$ ppp]	Beam Loss [%]	
PSB	3.6	2.3	2.4	low vertical emittance
PS (inj. + acc.)	3.2	2.3	0.9	-
PS (extr.)	3.2	2.2	~ 4 (1*)	*with barrier bucket
PS-to-SPS (inj.)	3.0	2.2	~ 5	vertical scraping
SPS (acc.)	5.7	~ 4.0	~ 5	RF & TFB power
SPS (slow extr.)	4.1	~ 4.0	~ 3 (1.5*)	*with prototype crystal
SPS (fast extr.)	5.3	-	-	shadowing technique

Table 13: SFTPRO record and operational cycle intensity (ppp) and beam loss along the accelerator chain [174]. Note that two batches are injected into the SPS from the PS for a single SPS cycle.)

PS. The transmission losses are likely caused by different sources, including the vertical aperture limit of the SPS and RF capture in the SPS. The RF upgrades performed for LIU [176] will help increase historical limits on the maximum intensity that could be accelerated in the SPS, with the record standing at 5.7×10^{13} ppp accelerated through transition but not extracted [177]. In principle, the new RF system is specified to accelerate 7×10^{13} ppp, contingent on a detailed stability analysis. The SPS internal dump can withstand a load of 7×10^{13} ppp if the integrated flux is monitored to not exceed a given limit. Other technical aspects to study in the SPS in the coming years include the limits of the transverse-feedback system to mitigate collective instabilities and the impact of the increased intensity and horizontal emittance on the slow extraction beam loss and the different beam-loss mitigation techniques being implemented [178, 179].

It should be pointed out that an intensity increase on the SFTPRO cycle would also ease the throughput and sharing of protons across the CERN accelerator complex. In particular, the ability to switch the North Area destination of protons, within the same SPS cycle and on the same flat-top between the High Intensity facility in ECN3 and the other North Area targets destinations, could help proton sharing constraints.

6.2 Opportunities with BDF irradiation stations

The high-energy, high-intensity proton beam from the SPS impacting on BDF’s high-A/Z production target produces a unique particle spectrum, fluences and total dose of radiation in the region around the target. This presents an opportunity to synergetically exploit the target complex for other purposes, without perturbing the main physics goals of BDF/SHiP. The target complex could house additional infrastructure required to implement a lateral radiation port that would allow using the significant neutron fluence emerging from the production target for physics or for mixed-field neutron irradiations [153] for accelerator and material science applications.

A similar field of radiation is present at ‘standard’ spallation neutron sources but it is not easily exploited owing to the specific physics and engineering criteria that apply at

those facilities, including closely coupled cryogenic moderators and reflectors. These deplete significantly the high-energy components of the particle spectra.

The availability of the extremely intense neutron flux at BDF offers a singular opportunity to study neutron-induced reactions on short-lived isotopes, of interest to, for instance, nuclear astrophysics. Preliminary Monte Carlo simulations indicate that a flux of around 10^{13} – 10^{14} neutrons/cm 2 /pulse could be available in the proximity of the BDF target, with a spectrum covering the range from thermal energy to 100 MeV, with a peak around 1 MeV.

Since the long duration of the proton pulse (\sim 1 s) does not allow using time-of-flight techniques for neutron energy determination, only integral cross-section measurements can be performed. For this, the neutron spectrum has to be suitably tailored to the needs of the study. In particular, for studies related to nuclear astrophysics, it is desirable to rely on a Maxwellian-like neutron spectrum, with kT between 10 and 100 keV. Such a spectrum can be obtained with an additional, small, moderation of the BDF neutron flux, so as to lower the average neutron energy, and with the use of suitable filters or absorbers, to suppress the thermal and epithermal component. Studies in this direction are already ongoing in the n_TOF Collaboration. Hence, a BDF neutron facility would benefit from the experience that will be gained in the next few years at the n_TOF near-target irradiation facility. The huge neutron flux available at the BDF would surpass all facilities now being constructed and planned for the near future. Even assuming a reduction due to the moderation and filtering process of two orders of magnitude, a flux of 10^{12} neutrons/cm 2 /pulse would be available for the measurements. This is three orders of magnitude higher than expected, for example, at the near-target irradiation station at n_TOF, and two orders of magnitude higher than at the most intense Maxwellian neutron source currently available, at SARAF, which is characterised by an average neutron flux of 1.2×10^{10} neutrons/cm 2 /s. More details are reported in [83].

The BDF infrastructure and operation also provide a unique opportunity for hosting irradiation test facilities for materials and electronics. The unparalleled mixed-field radiation levels expected near the target, reaching integral annual levels of roughly 400 MGy and 10^{18} 1 MeV-neutron equivalent per square centimetre, would allow accelerated testing in a highly representative environment for future accelerator applications, including for instance the components linked to the HE-LHC, FCC-hh, and potentially FCC-ee.

With the proposed design of the target and target complex, described in Section 2.3, two zones have been identified where equipment could be installed to profit from the mixed secondary radiation field generated in the target, shown in Figure 61.

The innermost irradiation zone ("internal" in Figure 61) would feature - depending on the exact location - around 100–400 MGy/y of mixed field irradiation per year, dominated by high-energy neutrons. This zone would be adapted for irradiation of multiple "small" volumes, each in the order of 20–40 cm 3 . The levels attained are sufficient to both study the effect of the total ionising dose (TID), mainly affecting insulating, polymeric materials, and the effect of displacement per atom, mainly affecting the mechanical and thermo-physical properties of metals [180, 181]. Electronics can be tested in a similar way in order to perform passive, unbiased displacement damage studies, or active (i.e. biased) studies of TID effects [182]. In both cases, lifetime levels compatible with those expected in the most exposed detector areas in the FCC-hh would be attained, providing an excellent opportunity to evaluate the radiation tolerance of electronics, well beyond the limit of what present

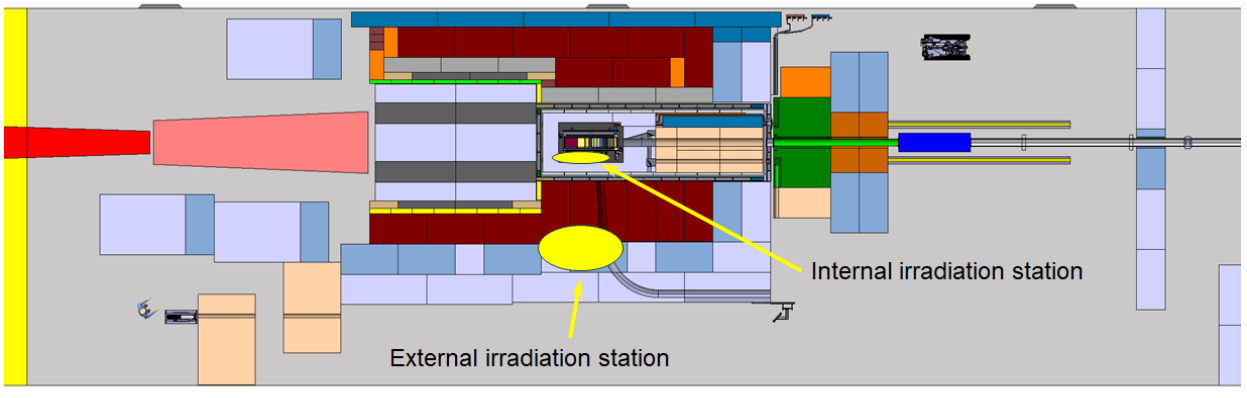


Figure 61: Potential locations identified for irradiation stations around the target complex of BDF/SHiP.

silicon-based technologies can withstand. Access to the irradiation zone would either be implemented with a pneumatic actuated ("rabbit") system, or by opening the target assembly during the year-end technical stops of the accelerator complex.

In addition to the near-target irradiation station, providing the broad range of dose rates and fluxes for ultra-high dose and ultra-high fluence sample irradiation, a more accessible zone with a lower radiation level could be constructed for testing electronic components, boards, and systems. Such a zone would require neutron fluxes (>10 MeV) in the 10^4 – 10^8 neutrons/cm 2 /s range, and would allow qualification of electronic equipment to be operated in accelerator environments. Ideally, an area of several square metres should be available, enabling the radiation qualification of bulky systems, such as power converters. With the increased interest in and need for using commercial off-the-shelf electronic components and systems-on-chip, large-scale irradiation is in principle the only viable solution to ensure adequate radiation tolerance. Such information apply not only to accelerator applications but also to ground-level (e.g. automotive applications and high-reliability servers), avionic, and so-called new space applications. A zone for this purpose could be envisaged at the BDF target complex ("external" in Figure 61), with a dedicated irradiation bunker on the side of the target, without perturbing the main physics aim of the facility.

Another possibility - still to be explored in more detail - involve the extraction of a neutron beam from the target complex, to perform non-destructive activities such as neutron imaging of radioactive samples [183], or to perform neutron activation measurements, similar to what it is done at the NEAR area of the n_TOF facility [184, 181]. This may also include installing a dedicated moderator on the production target.

Implemented as subsidiary to the BDF facility, the irradiation stations can not be operated as a dedicated and independent irradiation facility infrastructure, such as IR-RAD/CHARM at CERN, but rather as a complementary solution to cover use-cases not addressed in current CERN irradiation facilities or external ones. The CERN RADNEXT project is currently evaluating the potentials of an irradiation facility at BDF/SHiP to better satisfy the long-term needs for the future large colliders, such as the FCCee and the FCChh.

For all these options a dedicated study will be launched in the TDR phase, in order to assess the impact on the infrastructure. It is expected that the modifications required will be minimal if taken into account early in the development phase.

6.3 Liquid argon TPC detector for extending searches for FIPs

An interesting detector technology to complement and enhance BDF/SHiP’s capabilities for BSM particle searches is that of a Liquid Argon Time Projection Chamber (LArTPC). LArTPCs are imaging and homogeneous calorimetric devices that are very suitable as detector for rare event searches. The LArTPCs output is bubble-chamber-like images that can be three-dimensionally reconstructed, allowing to distinguish between different interaction processes with high accuracy. Photodetectors using the scintillation light are typically used for triggering the detector.

This LArTPC technology has matured substantially over the last ten years and is now regularly used as the technology for neutrino and dark matter experiments. Most notably, the ICARUS LArTPC of about 500 tonnes was originally one of the far detectors at the LNGS for the CNGS neutrino beam. ICARUS is now exploited as the far detector in the short baseline neutrino oscillation experiment at Fermilab, together with SBND, another LArTPC, as near detector. Four 10 ktonnes active mass LArTPCs will be used as far detectors for the DUNE experiment. These are only few of the examples of the planned usage of LArTPC technologies. Also the Forward Physics Facility, a proposal being prepared for forward physics studies at the LHC, plans to include a large LArTPC. At CERN there is significant experience with building the large 700 tonnes LArTPC detectors that are constructed as prototypes for the large DUNE far detectors.

LArTPCs provides an actual electronic event picture of the signal candidates of interest that are being produced in its fiducial volume. E.g. for an HNL decaying in the detector, the decay vertex and the tracks or showers coming from the decay particles can be imaged. Similarly e.g. light dark matter particles or millicharged particles, produced in the beam dump target, that scatter with the argon of the detector lead to visible signals.

Recently, LArTPCs have been used for searches for millicharged [185] particles, heavy QCD axions [186], HNLs [187, 188] and Higgs portal scalars [188] in ArgoNeuT and Micro-BooNE. MeV-scale energy depositions by low-energy photons produced in neutrino-argon interactions have been identified and reconstructed in ArgoNeuT liquid argon time projection chamber data. Analyses are presently ongoing in ICARUS on (light) Dark Matter searches, and have been reported by dedicated Dark Matter experiments such as DarkSide [189]. Future neutrino experiments such as SBND (starting next year) and the DUNE experiment, in particular via the near detector will have LArTPCs to address BSM searches.

At BDF/SHiP in ECN3, a possible configuration is to install a LArTPC behind the SHiP HSDS spectrometer, as shown in Figure 62, where a \sim 23 m long free space is available. Clearly such a detector will enhance the SHiP physics program with sensitivity to light dark matter scattering and millicharged particles passing the detector, as well as complement the searches for decays of HNLs, axions, dark photons and more. Specific sensitivity studies on these channels are just starting. Clearly, if an excess is observed in any of these channels in SHiP, the visual confirmation of the observation will be of paramount importance to strengthen the case for a discovery.

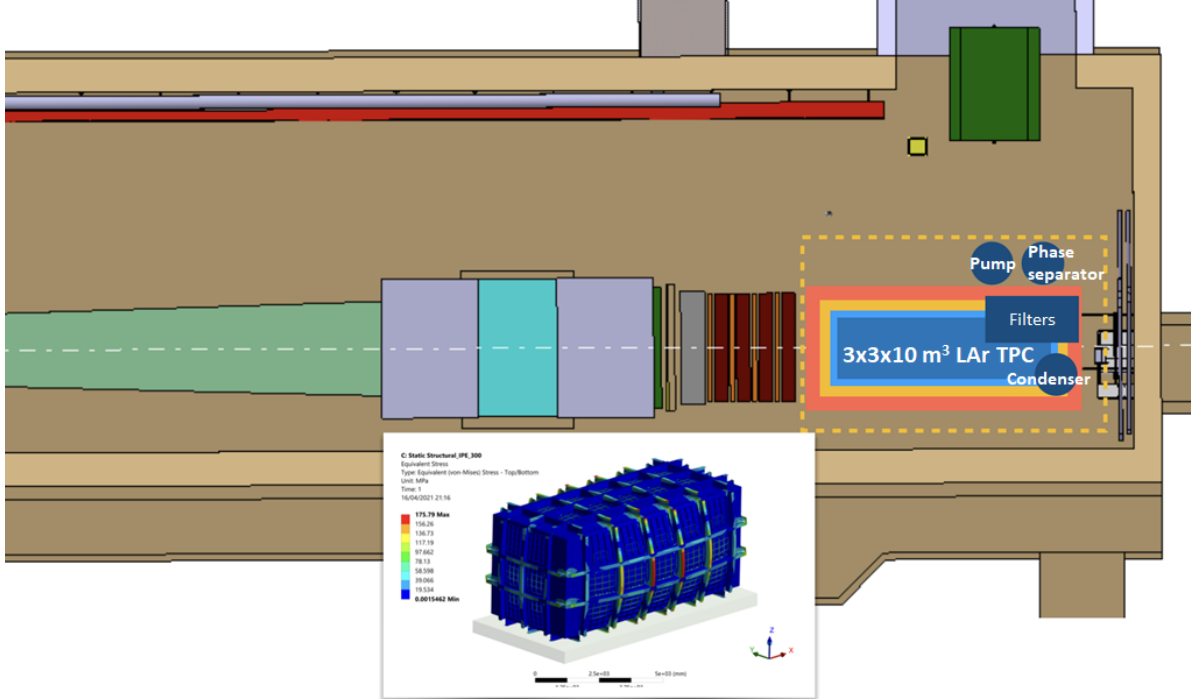


Figure 62: Placement of the LArTPC behind the SHiP detector with approximate $3 \times 3 \times 10$ m 3 active volume. The sketch represents the space occupied by the cryostat and the main cryogenic components. In the box, a preliminary engineering analysis of a cryostat design is shown.

Argon is abundant in the atmosphere, from where it is distilled. Despite being a cryogenic in liquid state, its maintenance is not sophisticated, as it can be cooled with liquid nitrogen. Argon can be easily purified to allow electrons from the ionisation following the particle interaction to drift over long distances. In turn, this allows to instrument uniformly large volumes/masses of argon.

The critical TPC components are 1) the HV system, in charge of creating stable and uniform electric field throughout the active volume, 2) the charge readout modules, for which several technology and geometry (wire, strips, pixels, ...) exist and have been tested in multiple detectors, 3) the photon detector system to record the scintillation light signals, 4) sensitive and low noise electronics for preamplification of the charge signals, and 5) the data acquisition and triggering system.

For what concerns the infrastructure, the LArTPC requires 1) the cryostat that contains the detector components and the liquid argon, and limits the heat input, and 2) the cryogenics system in charge of maintaining stable thermodynamic conditions and achieving sufficient argon purity.

At BDF/SHiP, a LArTPC based on the following configuration could be envisaged. The space available behind SHiP has a footprint of approximately 6×14 m 2 which allows the installation of a TPC with an active volume up to $3 \times 3 \times 10$ m 3 (about 130 tonnes) and its cryogenic system. The volume could be split into two TPCs each one with a drift length of 1.5 m each, and a drift time of approximately 1 ms. Such a layout is shown in Figure 62.

6.3.1 Physics reach with a LAr TPC detector

A LAr detector may serve two purposes. Firstly, it may visualize the events and serve as an event display for FIP decays, which would provide additional information about the event, e.g., the particle multiplicity.

Secondly, given the lower energy threshold than for the emulsion in the SND, it may detect stable particles such as MCPs in a way complementary to the SND – via multiple low-energy scatterings along the trajectory [36]. Indeed, as it was discussed in the introduction, the MCP scattering is mediated by a massless photon, and therefore the recoil electrons would likely have energies sharply peaked at small values $E_e \ll 100$ MeV. The smallness of the MCP charge may be compensated by the largeness of the scattering cross-section at small electron energy. In this case, the signature would be several displaced hits with soft electrons along the trajectory of the MCPs pointing to the target. Such a signature has been used to constrain the parameter space of MCPs at the ArgoNeuT experiment [185], where the energy threshold may be as small as $E_{e,\text{thr}} \simeq 1$ MeV.

To demonstrate the potential of LAr, Figure 63 shows the sensitivity to HNLs coupled to muons and to MCPs. For the baseline configuration of the detector, we consider a box with dimensions $3\text{ m} \times 3\text{ m} \times 10\text{ m}$, located 97 m downstream of the target.

For the decay products of HNLs, following [190], we require the energy cuts $E_{\gamma,e,\mu} > 30$ MeV, $E_\pi > 100$ MeV, and also impose the cut on the angle between the momentum of the two HNL decay products x_1, x_2 and the beam axis $\theta_{x_1 x_2, \text{axis}} > m_N/(E_1 + E_2)$. In the same figure, we also show the sensitivity of SHiP itself. A factor $\simeq 4$ larger number of events with long-lived HNLs would be observed at SHiP, given a larger geometric coverage of the decay volume and a much larger length. This means that one would have the event visualization already if $N_{\text{events,SHiP}} \gtrsim 10$.

For MCPs, we consider the two-hit signature with various electron energy thresholds $\Delta E_{\min} = 1, 10$, and 30 MeV. The sensitivity of the LAr experiment to the MCPs is shown in Figure 63.

6.4 Tau lepton flavour violation experiment

Similarly to the original CDS design, the implementation of BDF/SHiP in TCC8/ECN3 offers a potential opportunity to host and operate in parallel an experiment ("TauFV", described in detail in [191]) to search for lepton flavour violation and rare decays. This is possible by taking advantage of the very large sample of tau leptons and D mesons that could be produced by using an in-line thin target and a detector located on the BDF beam line in the upstream end of the TCC8 target hall. The most suitable location to implement the TauFV experiment is about 100 m upstream of the BDF target. The TauFV target would be situated at the current location of the T10 kaon target. Intercepting $\sim 1\%$ of the intensity delivered to the BDF/SHiP target, the experiment would have access annually to $\mathcal{O}(10^{13})$ tau lepton, $\mathcal{O}(10^{15})$ D meson decays, and $\mathcal{O}(10^{18})$ kaon decays. Assuming a branching ratio of 10^{-10} and a detector acceptance times pre-selection efficiency of 5% for $\tau \rightarrow \mu\mu\mu$, TauFV would have access to > 1000 events, compared to one event in Belle II, 14 events in LHCb Upgrade I, and 84 events in LHCb Upgrade II with their full sets of luminosity.

The very challenging reconstruction of secondary vertices and suppression of background

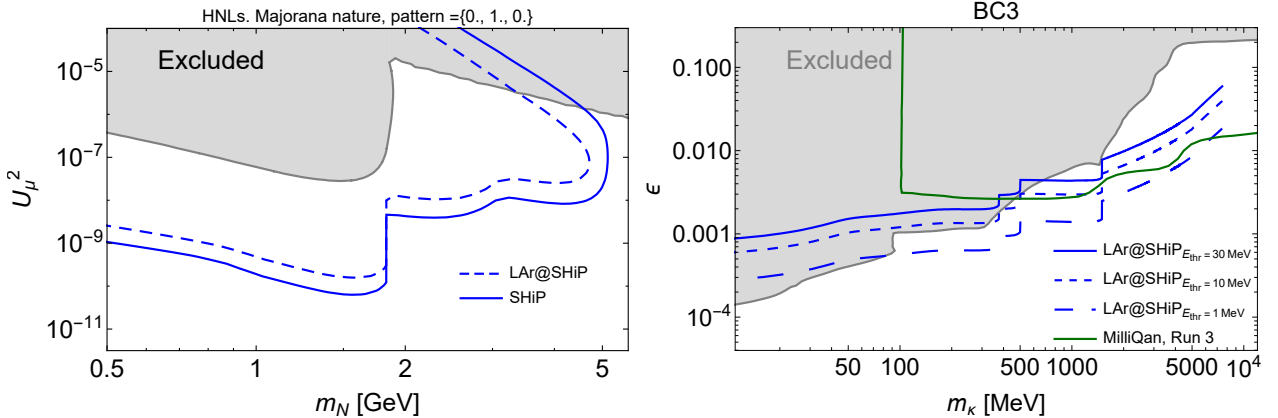


Figure 63: Potential of a LAr detector to be installed behind the decay spectrometer of the SHiP experiment. Left: the sensitivity to HNLs that mix predominantly with muon neutrinos. Right: the 90%CL sensitivity of the LAr detector installed behind the HSDS detector to millicharged particles assuming zero background. Three different options for the electron energy threshold are considered: 1 MeV, 10 MeV, and 30 MeV. The excluded region and the sensitivity of MilliQan is taken from [8]. The sensitivities are computed using `SensCalc` (see text for details) for $N_{\text{PoT}} = 6 \times 10^{20}$.

can be significantly enhanced by using a target made up of a set of narrow pure tungsten blades, located one after the other with a spacing of a few centimetres, in conjunction with a highly elliptic transverse beam profile to dilute the pile-up of interactions along the blade. Preliminary studies indicate that minimal changes to the settings of the existing magnets in the P42 beam line can provide the required beam spot of $\sigma_x \times \sigma_y \sim 0.3 \times 7 \text{ mm}^2$ at the chosen location of the TauFV target, and at the same time produce the desired blow-up of $\sigma_{x,y} \sim 45 \text{ mm}$ at the BDF/SHiP target.

The target system would be integrated together with a movable silicon-pixel vertex detector, similar to LHCb. The target under study is comprised of five blades of 0.4 mm thickness in the beam direction, and 2 mm height and 40 mm length orthogonal to the beam. The energy deposition on the target blades has been estimated with FLUKA Monte Carlo simulations [121, 122], and is expected to be of the order of $\sim 450 \text{ J/cm}^3$ in each blade after one pulse (peak). Due to the high beam power, and the fact that the surrounding vertex detector must be operated under cooling, the target must be actively cooled with an inert gas. The initial studies consider a common assembly in which the target and vertex detector is contained in a closed-loop tank with cooling in the form of forced circulation of helium. Preliminary computational fluid dynamics (CFD) simulations have been carried out in order to calculate the heat transfer coefficient that could be achieved. The studies indicate that a target system conceived in this way is feasible. A helium-cooling apparatus, similar to what was implemented for the T9 target [192], with full helium gas re-circulation, appears to be suitable. The expected flow rate is around $600\text{-}700 \text{ m}^3/\text{h}$, in order to achieve an average helium velocity in contact with the blades of around 50 m/s. The average heat transfer coefficient (HTC) at the surface of the tungsten blades is estimated at around $350 \text{ W}/(\text{m}^2 \cdot \text{K})$ in this way. The HTC value obtained was used as a boundary condition for FEM calculations aimed at validating the target design from a thermo-mechanical point of view. The thermal

simulations shows that the estimated convection through the helium leads to an acceptable temperature in the target blades of around 220 °C after a beam impact. Given that tungsten is a refractory metal with a high melting point, the temperature reached is within the limits for safe operation of the target. The thermal stresses induced by the temperature increase in the target materials have been estimated. The maximum von Mises equivalent stress is equal to the maximum compressive stress, and is around 220 MPa, significantly below the tensile strength of the material at the operational temperatures (550 MPa at 300 °C).

The main challenges in the manufacturing of the target are associated with the production and machining of the thin tungsten blades, due to the brittleness of pure tungsten at room temperature. Alternatively, a tungsten alloy with a NiFe or NiCu content could be considered, allowing a similar density but higher strength and ductility. If necessary, slightly lighter materials with higher ductility, such as tantalum or tantalum alloys, could be potential alternatives.

The target station requires full remote handling due to the high dose rate (see below), similar to the BDF/SHiP target station. The head space available in TCC8 allows adopting similar design principles. A detailed engineering study is required to define the overall design of the target/detector interfaces.

The detector proposed in a dedicated study during the CDS phase consists of a 7.5 m long and 3 m wide spectrometer including the vertex detector, tracker, fast timing detector, electromagnetic calorimeter and muon system. The experimental dipole produces a field of 2.5 Tm over a length of 2 m with the possibility of swapping polarity. In order to correct for the deflection of the primary proton beam of 1.87 mrad by the experimental magnet, compensating magnets are foreseen at the end of the experiment.

The experiment concept has undergone a first radiation protection assessment in order to define the shielding and access requirements. It is based on FLUKA simulations performed in the framework of the BDF CDS [83], for which prompt as well as residual radiation were studied allowing a preliminary shielding design. The design foresees that the detector is implemented within a bunker with a footprint of $\sim 15 \times 5 \text{ m}^2$ and a height of $\sim 5 \text{ m}$, as shown in Figure 64, and that movable shielding and remote handling is used to perform maintenance of the target system and detector components. In view of the larger amount of soil above TCC8 than for the CDS location, the proposed shielding design appears sufficient to reduce dose rates above-ground to be compatible with a Non-designated Area. The shielding is also expected to contain sufficiently well the residual dose rates of the highly activated target and detector. Comparing the expected prompt radiation levels in the soil below TauFV with the ones at the BDF target complex (see Section 2.7), shows that the expected soil activation is compliant with the conservative design limits for the sides and the top of the TCC8 cavern around the TauFV experiment. Additional shielding is only required below the setup, which, similarly to the BDF target complex, could be integrated into the cavern floor. In the next phase of the study, it is planned to perform optimisation of the shielding. The impact of the remnant beam on the activation downstream of TauFV should be evaluated. Also, the environmental impact from releases of radioactive air should also be carefully addressed.

The section of TCC8 around TauFV has a width of 10 m and a height of 5 m below the bridge crane, enabling integration of the TauFV experiment on the BDF/SHiP beam line, as shown in Figure 64. A certain level of civil engineering is expected in order to

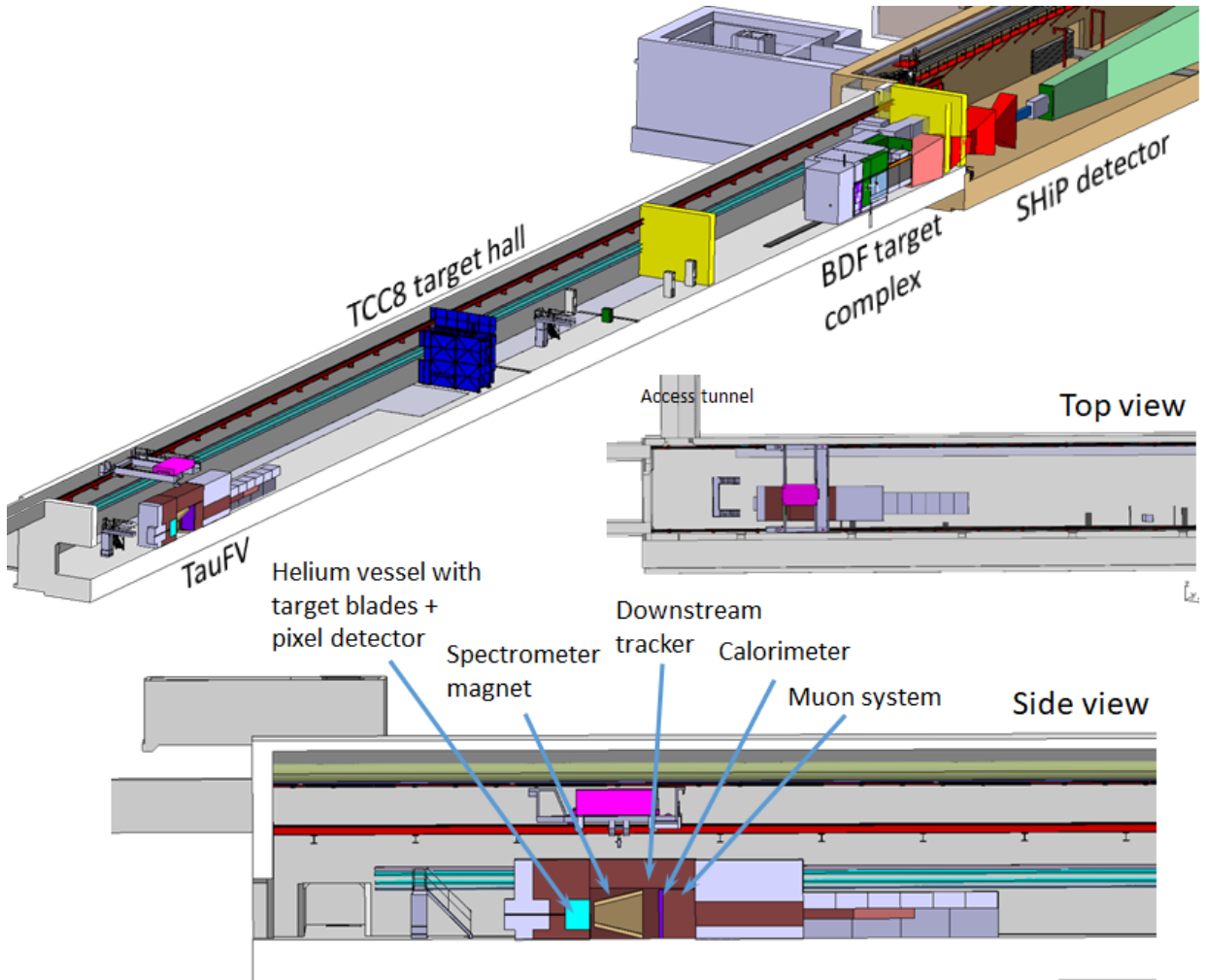


Figure 64: Overview of TauFV integrated into the TCC8 target hall on the BDF/SHiP beam line.

implement shielding in the floor and an air confinement around the experiment. An personnel access point is currently available at this location in TCC8 via the access shaft and tunnel associated with building 912. However, for installation, maintenance and decommissioning, civil engineering will be necessary to complement this with the appropriate material access compatible with the constraints associated with the activated components.

Further simulation studies must also be made to understand the impact of TauFV on the SHiP experiment in terms of background. The flux from intercepting 1–2% of the beam is small but the residual muon flux penetrating the target bunker enters into the SHiP muon shield at a location and angular distribution for which it was not designed. This could potentially lead to capture of a fraction of the muons increasing significantly the flux in the SHiP acceptance. This will be followed up if interest in TauFV builds up in the future.

Acknowledgements

The SHiP Collaboration wishes to thank the Castaldo company (Naples, Italy) for their contribution to the development studies of the decay vessel. The support from the National Research Foundation of Korea with grant numbers of 2018R1A2B2007757, 2018R1D1A3B07050649, 2018R1D1A1B07050701, 2017R1D1A1B03036042, 2017R1A6A3A01075752, 2016R1A2B4012302, and 2016R1A6A3A11930680 is acknowledged. The support from the FCT - Fundação para a Ciencia e a Tecnologia of Portugal with grant number CERN/FIS-PAR/0030/2017 is acknowledged. The support from the TAEK of Turkey are acknowledged.

We are greatly indebted to the support of the Beam Dump Facility Working Group (below).

Outside of the SHiP collaboration and the BDF WG, we acknowledge in particular, for their contribution to:

- magnetisation of hadron stopper: V. Bayliss, J. Boehm, G. Gilley,
- muon shield superconducting magnet: B. Cure, M. Mentink, A. Milanese, E. Todesco,
- superconducting spectrometer magnet: H. Bajas, A. Ballarino, A. Devred, A. Milanese, D. Tommasini,
- BDF irradiation station: S. Danzeca, S. Fiore, G. Lerner, A. Mengoni, N. Pacifico, F. Ravotti, R. Garcia Alia,
- LAr TPC: F. Resnati,
- TauFV: P. Collins, G. Wilkinson,
- and to the development of the SHiP detectors: M. Andreini, H. Danielsson, L. Di Giulio.

BDF Working Group³⁰

O. Aberle, C. Ahdida, P. Arrutia, K. Balazs, M. Calviani, Y. Dutheil, L.S. Esposito, R. Franqueira Ximenes, M. Fraser, F. Galleazzi, S. Gilardoni, J.-L. Grenard, T. Griesemer, R. Jacobsson, V. Kain, L. Krzempek, D. Lafarge, S. Marsh, J.M. Martin Ruiz, G. Mazzola, R.F. Mena Andrade, Y. Muttoni, A. Navascues Cornago, P. Ninin, J. Osborne, R. Ramjiawan, F. Sanchez Galan, P. Santos Diaz, F. Velotti, H. Vincke, P. Vojtyla

References

- [1] J. Beacham et al., *Physics beyond colliders at CERN: beyond the Standard Model working group report*, *Journal of Physics G: Nuclear and Particle Physics* **47** (2019) 010501 [[1901.09966](#)].
- [2] P. Agrawal et al., *Feebly-interacting particles: FIPs 2020 workshop report*, *Eur. Phys. J. C* **81** (2021) 1015 [[2102.12143](#)].
- [3] S. Alekhin et al., *A facility to search for hidden particles at the CERN SPS: the SHiP physics case*, *Reports on Progress in Physics* **79** (2016) 124201.
- [4] CMS collaboration, *Search for long-lived heavy neutral leptons with displaced vertices in proton-proton collisions at $\sqrt{s} = 13$ TeV*, *JHEP* **07** (2022) 081 [[2201.05578](#)].
- [5] I. Boiarska, K. Bondarenko, A. Boyarsky, S. Eijima, M. Ovchynnikov, O. Ruchayskiy and I. Timiryasov, *Probing baryon asymmetry of the Universe at LHC and SHiP*, [1902.04535](#).
- [6] A. Blondel et al., *Searches for long-lived particles at the future FCC-ee*, *Front. in Phys.* **10** (2022) 967881 [[2203.05502](#)].
- [7] A.M. Abdullahi et al., *The Present and Future Status of Heavy Neutral Leptons*, in *2022 Snowmass Summer Study*, 3, 2022 [[2203.08039](#)].
- [8] C. Antel et al., *Feebly Interacting Particles: FIPs 2022 workshop report*, in *Workshop on Feebly-Interacting Particles*, 5, 2023 [[2305.01715](#)].
- [9] W. Bonivento, A. Boyarsky, H. Dijkstra, U. Egede, M. Ferro-Luzzi, B. Goddard, A. Golutvin, D. Gorbunov, R. Jacobsson, J. Panman, M. Patel, O. Ruchayskiy, T. Ruf, N. Serra, M. Shaposhnikov and D. Treille, *Proposal to Search for Heavy Neutral Leptons at the SPS*, Tech. Rep. [CERN-SPSC-2013-024](#), SPSC-EOI-010, SPSC-EOI-010 [[1310.1762](#)], CERN, Geneva (Oct, 2013).
- [10] SHiP collaboration, *A Facility to Search for Hidden Particles (SHiP) at the CERN SPS - Technical Proposal*, Tech. Rep. [CERN-SPSC-2015-016](#), SPSC-P-350, SPSC-P-350, [[1504.04956](#)], CERN, Geneva (Apr, 2015).
- [11] SHiP collaboration, *The experimental facility for the Search for Hidden Particles at the CERN SPS*, *JINST* **14** (2019) P03025.
- [12] SHiP collaboration, *The SHiP experiment at the proposed CERN SPS Beam Dump Facility*, *Eur. Phys. J. C* **82** (2022) 486.
- [13] T. Asaka, S. Blanchet and M. Shaposhnikov, *The nuMSM, dark matter and neutrino masses*, *Phys. Lett. B* **631** (2005) 151 [[hep-ph/0503065](#)].
- [14] T. Asaka and M. Shaposhnikov, *The ν MSM, dark matter and baryon asymmetry of the universe*, *Phys. Lett. B* **620** (2005) 17 [[hep-ph/0505013](#)].

- [15] J.-L. Tastet and I. Timiryasov, *Dirac vs. Majorana HNLs (and their oscillations) at SHiP*, [1912.05520](#).
- [16] O. Mikulenko, *Reconstructing the properties of new particle with beam dump experiments (Preliminary)*, **Expected 2023**.
- [17] P. Ilten, Y. Soreq, M. Williams and W. Xue, *Serendipity in dark photon searches*, *JHEP* **06** (2018) 004 [[1801.04847](#)].
- [18] F. Kling and S. Trojanowski, *Forward experiment sensitivity estimator for the LHC and future hadron colliders*, *Phys. Rev. D* **104** (2021) 035012 [[2105.07077](#)].
- [19] B. Patt and F. Wilczek, *Higgs-field portal into hidden sectors*, [hep-ph/0605188](#).
- [20] L. Visinelli and P. Gondolo, *Dark Matter Axions Revisited*, *Phys. Rev. D* **80** (2009) 035024 [[0903.4377](#)].
- [21] C. Gross, O. Lebedev and T. Toma, *Cancellation Mechanism for Dark-Matter–Nucleon Interaction*, *Phys. Rev. Lett.* **119** (2017) 191801 [[1708.02253](#)].
- [22] H. Davoudiasl, H.-S. Lee and W.J. Marciano, *Dark Side of Higgs Diphoton Decays and Muon g-2*, *Phys. Rev. D* **86** (2012) 095009 [[1208.2973](#)].
- [23] I. Boiarska, K. Bondarenko, A. Boyarsky, V. Gorkavenko, M. Ovchinnikov and A. Sokolenko, *Phenomenology of GeV-scale scalar portal*, *JHEP* **11** (2019) 162 [[1904.10447](#)].
- [24] P. Svrcek and E. Witten, *Axions In String Theory*, *JHEP* **06** (2006) 051 [[hep-th/0605206](#)].
- [25] A. Arvanitaki, S. Dimopoulos, S. Dubovsky, N. Kaloper and J. March-Russell, *String Axiverse*, *Phys. Rev. D* **81** (2010) 123530 [[0905.4720](#)].
- [26] M. Cicoli, M. Goodsell and A. Ringwald, *The type IIB string axiverse and its low-energy phenomenology*, *JHEP* **10** (2012) 146 [[1206.0819](#)].
- [27] M. Bauer, M. Neubert, S. Renner, M. Schnubel and A. Thamm, *The Low-Energy Effective Theory of Axions and ALPs*, *JHEP* **04** (2021) 063 [[2012.12272](#)].
- [28] M. Bauer, M. Neubert, S. Renner, M. Schnubel and A. Thamm, *Flavor probes of axion-like particles*, *JHEP* **09** (2022) 056 [[2110.10698](#)].
- [29] B. Döbrich, J. Jaeckel and T. Spadaro, *Light in the beam dump - ALP production from decay photons in proton beam-dumps*, *JHEP* **05** (2019) 213 [[1904.02091](#)].
- [30] A. Bharucha, F. Brümmer, N. Desai and S. Mutzel, *Axion-like particles as mediators for dark matter: beyond freeze-out*, *JHEP* **02** (2023) 141 [[2209.03932](#)].
- [31] P.J. Fitzpatrick, Y. Hochberg, E. Kuflik, R. Ovadia and Y. Soreq, *Dark Matter Through the Axion-Gluon Portal*, [2306.03128](#).

- [32] K. Kaneta, H.-S. Lee and S. Yun, *Dark photon relic dark matter production through the dark axion portal*, *Phys. Rev. D* **95** (2017) 115032 [[1704.07542](#)].
- [33] B. Holdom, *Two $U(1)$'s and Epsilon Charge Shifts*, *Phys. Lett. B* **166** (1986) 196.
- [34] S. Tulin, H.-B. Yu and K.M. Zurek, *Resonant Dark Forces and Small Scale Structure*, *Phys. Rev. Lett.* **110** (2013) 111301 [[1210.0900](#)].
- [35] H. Liu, N.J. Outmezguine, D. Redigolo and T. Volansky, *Reviving Millicharged Dark Matter for 21-cm Cosmology*, *Phys. Rev. D* **100** (2019) 123011 [[1908.06986](#)].
- [36] R. Harnik, Z. Liu and O. Palamara, *Millicharged Particles in Liquid Argon Neutrino Experiments*, *JHEP* **07** (2019) 170 [[1902.03246](#)].
- [37] J. Preskill, M.B. Wise and F. Wilczek, *Cosmology of the Invisible Axion*, *Phys. Lett. B* **120** (1983) 127.
- [38] L.F. Abbott and P. Sikivie, *A Cosmological Bound on the Invisible Axion*, *Phys. Lett. B* **120** (1983) 133.
- [39] M. Dine and W. Fischler, *The Not So Harmless Axion*, *Phys. Lett. B* **120** (1983) 137.
- [40] P. Arias, D. Cadamuro, M. Goodsell, J. Jaeckel, J. Redondo and A. Ringwald, *WISPy Cold Dark Matter*, *JCAP* **06** (2012) 013 [[1201.5902](#)].
- [41] G. Krnjaic, *Probing Light Thermal Dark-Matter With a Higgs Portal Mediator*, *Phys. Rev. D* **94** (2016) 073009 [[1512.04119](#)].
- [42] A. Berlin and F. Kling, *Inelastic Dark Matter at the LHC Lifetime Frontier: ATLAS, CMS, LHCb, CODEX-b, FASER, and MATHUSLA*, *Phys. Rev. D* **99** (2019) 015021 [[1810.01879](#)].
- [43] B.W. Lee and S. Weinberg, *Cosmological Lower Bound on Heavy Neutrino Masses*, *Phys. Rev. Lett.* **39** (1977) 165.
- [44] SHiP collaboration, *Sensitivity of the SHiP experiment to light dark matter*, *JHEP* **04** (2021) 199 [[2010.11057](#)].
- [45] J.L. Feng et al., *The Forward Physics Facility at the High-Luminosity LHC*, *J. Phys. G* **50** (2023) 030501 [[2203.05090](#)].
- [46] DONUT collaboration, *Observation of tau neutrino interactions*, *Phys. Lett. B* **504** (2001) 218 [[hep-ex/0012035](#)].
- [47] K.K. et al., *Final tau-neutrino results from the DONuT experiment*, *Phys. Rev. D - Particles, Fields, Gravitation and Cosmology* **78**, pp. 1-20 ((2008)) .
- [48] R. Acquafredda et al., *The OPERA experiment in the CERN to Gran Sasso neutrino beam*, *JINST* **4** (2009) P04018.

- [49] OPERA collaboration, *Observation of tau neutrino appearance in the CNGS beam with the OPERA experiment*, *PTEP* **2014** (2014) 101C01 [[1407.3513](#)].
- [50] OPERA collaboration, *Final Results of the OPERA Experiment on ν_τ Appearance in the CNGS Neutrino Beam*, *Phys. Rev. Lett.* **120** (2018) 211801 [[1804.04912](#)].
- [51] OPERA collaboration, *Procedure for short-lived particle detection in the OPERA experiment and its application to charm decays*, *Eur. Phys. J.* **C74** (2014) 2986 [[1404.4357](#)].
- [52] OPERA collaboration, *Final results of the search for $\nu_\mu \rightarrow \nu_e$ oscillations with the OPERA detector in the CNGS beam*, *JHEP* **06** (2018) 151 [[1803.11400](#)].
- [53] OPERA collaboration, *Momentum measurement by the Multiple Coulomb Scattering method in the OPERA lead emulsion target*, *New J. Phys.* **14** (2012) 013026 [[1106.6211](#)].
- [54] C. Albright and C. Jarlskog, *Neutrino production of M+ and E+ heavy leptons (I)*, *Nuc. Phys. B* **84**, pp. **467-492** ((1975)) .
- [55] M. Reno, *Electromagnetic structure functions and neutrino nucleon scattering*, *Phys. Rev.* **D74**, **033001** ((2006)) .
- [56] PARTICLE DATA GROUP collaboration, *Review of Particle Physics*, *Progress of Theoretical and Experimental Physics* **2020** (2020) 083C01 [<https://academic.oup.com/ptep/article-pdf/2020/8/083C01/34673722/ptaa104.pdf>].
- [57] R.S. et al., *A new upper limit for the tau-neutrino magnetic moment*, *Phys. Lett. B* **513** **23-29** ((2001)) .
- [58] A.C. Benvenuti et al., *Observation of New Particle Production by High-Energy Neutrinos and anti-neutrinos*, *Phys. Rev. Lett.* **34** (1975) 419.
- [59] A.K.-T. et al. (CHORUS Collaboration), *Measurement of charm production in neutrino charged-current interactions*, *New Journal of Physics* **13** (2011) 093002.
- [60] NuTeV collaboration, *Precise Measurement of Dimuon Production Cross-Sections in ν_μ Fe and $\bar{\nu}_\mu$ Fe Deep Inelastic Scattering at the Tevatron.*, *Phys. Rev. D* **64** (2001) 112006 [[hep-ex/0102049](#)].
- [61] S. Carrazza, J.M. Cruz-Martinez and R. Stegeman, *A data-based parametrization of parton distribution functions*, *Eur. Phys. J. C* **82** (2022) 163 [[2111.02954](#)].
- [62] PARTICLE DATA GROUP collaboration, *Review of Particle Physics*, *PTEP* **2022** (2022) 083C01.
- [63] G. De Lellis, P. Migliozzi and P. Santorelli, *Charm physics with neutrinos*, *Phys. Rept.* **399** (2004) 227.

- [64] FERMILAB E531 collaboration, *Production Characteristics of Charmed Particles in Neutrino Interactions*, *Phys. Lett. B* **206** (1988) 380.
- [65] T. Bolton, *Determining the CKM parameter $V(cd)$ from neutrino N charm production*, [hep-ex/9708014](#).
- [66] CHORUS collaboration, *Measurement of topological muonic branching ratios of charmed hadrons produced in neutrino-induced charged-current interactions*, *Phys. Lett. B* **626** (2005) 24.
- [67] H. Abramowicz et al., *Experimental Study of Opposite Sign Dimuons Produced in Neutrino and anti-neutrinos Interactions*, *Z. Phys. C* **15** (1982) 19.
- [68] S.A. Rabinowitz et al., *Measurement of the strange sea distribution using neutrino charm production*, *Phys. Rev. Lett.* **70** (1993) 134.
- [69] CCFR collaboration, *Determination of the strange quark content of the nucleon from a next-to-leading order QCD analysis of neutrino charm production*, *Z. Phys. C* **65** (1995) 189 [[hep-ex/9406007](#)].
- [70] CHARM II collaboration, *Leading order QCD analysis of neutrino induced dimuon events*, *Eur. Phys. J. C* **11** (1999) 19.
- [71] M. Al-Turany, D. Bertini, R. Karabowicz, D. Kresan, P. Malzacher, T. Stockmanns and F. Uhlig, *The fairroot framework*, *Journal of Physics: Conference Series* **396** (2012) 022001.
- [72] GEANT4 collaboration, *GEANT4: A Simulation toolkit*, *Nucl. Instrum. Meth. A* **506** (2003) 250.
- [73] J. Allison et al., *Geant4 developments and applications*, *IEEE Trans. on Nucl. Science* **53** (2006) 270.
- [74] T. Sjöstrand, S. Mrenna and P.Z. Skands, *A Brief Introduction to PYTHIA 8.1*, *Comput. Phys. Commun.* **178** (2008) 852 [[0710.3820](#)].
- [75] T. Sjöstrand, *PYTHIA 5.7 and JETSET 7.4: Physics and manual*, [hep-ph/9508391](#).
- [76] T. Sjöstrand, S. Mrenna and P.Z. Skands, *PYTHIA 6.4 Physics and Manual*, *JHEP* **05** (2006) 026 [[hep-ph/0603175](#)].
- [77] H. Dijkstra and T. Ruf, *Heavy Flavour Cascade Production in a Beam Dump*, Tech. Rep. [CERN-SHiP-NOTE-2015-009](#) Dec 2015.
- [78] C. Andreopoulos et al., *The GENIE Neutrino Monte Carlo Generator*, *Nucl. Instrum. Meth. A* **614** (2010) 87 [[0905.2517](#)].
- [79] CHARM COLLABORATION collaboration, *A search for decays of heavy neutrinos in the mass range 0.5 - 2.8 GeV*, *Phys. Lett. B* **166** (1985) 473.

- [80] SHiP collaboration, *Muon flux measurements for SHiP at H4 - proposal*, Tech. Rep. [CERN-SPSC-2017-020](#), [SPSC-EOI-016](#), CERN, Geneva Jun 2017.
- [81] SHiP collaboration, *Measurement of the muon flux from 400 GeV/c protons interacting in a thick molybdenum/tungsten target*, *Eur. Phys. J. C* **80** (2020) 284.
- [82] E. Gschwendtner, K. Cornelis, I. Efthymiopoulos, I. Kratschmer, A. Pardons, H. Vincke and J. Wenninger, *CNGS, CERN Neutrinos to Gran Sasso, Five Years of Running a 500 Kilowatt Neutrino Beam Facility at CERN*, Conf. Proc. **C130512** (2013) MOPEA058.
- [83] C. Ahdida et al., *SPS Beam Dump Facility - Comprehensive Design Study*, CERN Yellow Reports: Monographs, CERN, Geneva (Dec, 2019), [10.23731/CYRM-2020-002](#), [[1912.06356](#)].
- [84] SHiP collaboration, *SHiP Experiment - Comprehensive Design Study report*, Tech. Rep. [CERN-SPSC-2019-049](#), [SPSC-SR-263](#), CERN, Geneva (Dec, 2019).
- [85] O. Aberle, C. Ahdida, P. Arrutia, K. Balazs, J. Bernhard, M. Brugger, M. Calviani, Y. Dutheil, R.F. Ximenes, M. Fraser, F. Galleazzi, S. Gilardoni, J.-L. Grenard, T. Griesemer, R. Jacobsson, V. Kain, D. Lafarge, S. Marsh, J.M. Martin Ruiz, R.F.M. Andrade, Y. Muttoni, A. Navascues Cornago, P. Ninin, J. Osborne, R. Ramjiawan, P. Santos Diaz, F. Sanchez Galan, H. Vincke and P. Vojtyla, *Study of alternative locations for the SPS Beam Dump Facility*, Tech. Rep. [CERN-SPSC-2022-009](#), [SPSC-SR-305](#), CERN, Geneva (2022).
- [86] SHiP collaboration, *BDF/SHiP at the ECN3 high-intensity beam facility*, Tech. Rep. [CERN-SPSC-2022-032](#), [SPSC-I-258](#), CERN, Geneva (2022).
- [87] “<https://indico.cern.ch/event/1284801/>.”
- [88] J. Bernhard, M. Brugger, M. Fraser, R. Jacobsson and Y. Kadi, *Memorandum - Support for Engineering Studies as input to the ECN3 Beam Delivery Task Force*, July, 2022. <https://edms.cern.ch/document/2758293>.
- [89] C. Ahdida et al., *Findings of the Physics Beyond Colliders ECN3 Beam Delivery Task Force*, in *CERN-PBC-REPORT-2023-001*, 2023, <https://cds.cern.ch/record/2847433>.
- [90] SHiP collaboration, *The active muon shield*, .
- [91] SHiP collaboration, *The active muon shield in the SHiP experiment*, *JINST* **12** (2017) P05011 [[1703.03612](#)].
- [92] K. Kershaw, J.-L. Grenard, M. Calviani, C. Ahdida, M. Casolino, S. Delavalle, D. Hounsome, R. Jacobsson, M. Lamont, E.L. Sola, R. Scott, V. Vlachoudis and H. Vincke, *Design Development for the Beam Dump Facility Target Complex at CERN*, *JINST* **13** (2018) P10011.

- [93] S. Pianese et al., *Design of the Future High Energy Beam Dump for the CERN SPS*, in *Proc. 9th International Particle Accelerator Conference (IPAC'18), Vancouver, BC, Canada, April 29-May 4, 2018*, no. 9 in International Particle Accelerator Conference, (Geneva, Switzerland), pp. 2612–2615, JACoW Publishing, June, 2018, DOI.
- [94] E. Lopez Sola, M. Calviani, P. Avigni, M. Battistin, J. Busom Descarrega, J. Canhoto Espadanal, M.A. Fraser, S. Gilardoni, B. Goddard, D. Grenier, R. Jacobsson, K. Kershaw, M. Lamont, A. Perillo-Marcone, M. Pandey, B. Riffaud, S. Sgobba, V. Vlachoudis and L. Zuccalli, *Design of a high power production target for the Beam Dump Facility at CERN*, *Phys. Rev. Accel. Beams* **22** (2019) 113001.
- [95] E. Lopez Sola, M. Calviani, O. Aberle, C. Ahdida, P. Avigni, M. Battistin, L. Bianchi, S. Burger, J. Busom Descarrega, J. Canhoto Espadanal, E. Cano-Pleite, M. Casolino, M.A. Fraser, S. Gilardoni, S. Girod, J.-L. Grenard, D. Grenier, M. Guinchard, C. Hessler, R. Jacobsson, M. Lamont, A. Ortega Rolo, M. Pandey, A. Perillo-Marcone, B. Riffaud, V. Vlachoudis and L. Zuccalli, *Beam impact tests of a prototype target for the Beam Dump Facility at CERN: Experimental setup and preliminary analysis of the online results*, *Phys. Rev. Accel. Beams* **22** (2019) 123001.
- [96] J.B. Descarrega, M. Calviani, T. Hutsch, E. López Sola, A.T.P. Fontenla, A.P. Marcone, S. Sgobba and T. Weißgärber, *Application of hot isostatic pressing (HIP) technology to diffusion bond refractory metals for proton beam targets and absorbers at CERN*, *Mater. Des. Proc. Comm.* **2** (2020) e101.
- [97] R. Ximenes et al., *Post irradiation examination of the prototype production target materials of the beam dump facility (bdf) at cern*, in *International Workshop on Spallation Materials Technology (IWSMT15), Santa Fe, New Mexico, USA, 5-10 March 2023*, no. 15 in International Workshop on Spallation Materials Technology, March, 2023.
- [98] R.F. Ximenes, O. Aberle, C. Ahdida, P. Avigni, M. Battistin, L. Bianchi, L. Buonocore, S. Burger, J. Busom, M. Calviani, J.C. Espadanal, M. Casolino, M.D. Castro, M. Fraser, S. Gilardoni, S. Girod, J. Grenard, D. Grenier, M. Guinchard, R. Jacobsson, M. Lamont, E.L. Sola, A.O. Rolo, A. Perillo-Marcone, Y. Pira, B. Riffaud, V. Vlachoudis and L. Zuccalli, *CERN BDF Prototype Target Operation, Removal and Autopsy Steps*, in *Proc. IPAC'21, Campinas, SP, Brazil*, no. 12 in International Particle Accelerator Conference, pp. 3559–3562, JACoW Publishing, Geneva, Switzerland, 08, 2021, DOI.
- [99] T. Griesemer, *Design development and technological r&d for niobium-cladded beam production targets*, in *Proc. IPAC'23*, no. 14 in IPAC'23 - 14th International Particle Accelerator Conference, pp. 4868–4871, JACoW Publishing, Geneva, Switzerland, 05, 2023, DOI.
- [100] R. Ximenes et al., *Beam dump facility production target at cern and advanced cladding technological r&d*, in *International Workshop on Spallation Materials*

Technology (IWSMT15), Santa Fe, New Mexico, USA, 5-10 March 2023, no. 15 in International Workshop on Spallation Materials Technology, March, 2023.

- [101] R. Andrade et al., *Loss-of-coolant-accident study for the beam dump facility at cern*, in *The 19th International Topical Meeting on Nuclear Reactor Thermal Hydraulics (NURETH-19), Brussels, Belgium, 6-11 March 2022*, no. 19 in International Topical Meeting on Nuclear Reactor Thermal Hydraulics, March, 2022.
- [102] S. Pianese, A. Perillo-Marcone, F.-X. Nuiry, M. Calviani, K.A. Szczurek, G.A. Izquierdo, P. Avigni, S. Bonnin, J. Busom Descarrega, T. Feniet, K. Kershaw, J. Lendaro, A. Perez Fontenla, T. Schubert, S. Sgobba and T. Weissgärber, *Hot isostatic pressing assisted diffusion bonding for application to the Super Proton Synchrotron internal beam dump at CERN. Hot Isostatic Pressing (HIP) assisted diffusion bonding between CuCr1Zr and AISI 316L for application to the Super Proton Synchrotron (SPS) internal beam dump at CERN*, *Phys. Rev. Accel. Beams* **24** (2021) 043001 [[2011.07942](https://arxiv.org/abs/2011.07942)].
- [103] K.G. Andersen, M. Calviani, A. Cherif, T. Coiffet, A. De Macedo, S. Devidal, J.-M. Geisser, S.S. Gilardoni, M. Gillet, E. Grenier-Boley, J. Heredia, A. Majbour, F. Monnet, M. Redondas Monteserín, F.-X. Nuiry, D. Pugnat, G. Romagnoli, Y. Seraphin, J. Somoza and N. Thaus, *Construction and Installation of the New CERN Proton Synchrotron Internal Beam Dumps. CONSTRUCTION AND INSTALLATION OF THE NEW CERN PROTON SYNCHROTRON INTERNAL BEAM DUMPS*, *JACoW IPAC 2021* (2021) 1409.
- [104] R.F. Ximenes et al., *Target systems design for a high intensity facility in the cern's ecn3 area*, in *Proc. IPAC'23*, no. 14 in IPAC'23 - 14th International Particle Accelerator Conference, pp. 3783–3786, JACoW Publishing, Geneva, Switzerland, 05, 2023, DOI.
- [105] O. Lantwin, *Optimisation of the SHiP experimental design*, 2019.
<https://cds.cern.ch/record/2693177>.
- [106] S. Shirobokov, *Optimisation of the SHiP Beam Dump Facility with generative surrogate models*, 2021. <https://spiral.imperial.ac.uk/handle/10044/1/95975>.
- [107] SHiP collaboration, *Optimising the active muon shield for the SHiP experiment at CERN*, *J. Phys. Conf. Ser.* **934** (2017) 012050.
- [108] M. Koratzinos and E. Van Herwijnen, *A possible yokeless superconducting dipole for the SHiP muon shield*, Tech. Rep. [CERN-SHiP-INT-006](#) (2022).
- [109] P. Wertelaers, *Normal-conducting muon shield with standard yoke iron and tuned return yoke ; first performance assessment*, Tech. Rep. [CERN-SHiP-INT-2022-004](#) (2022).
- [110] SHIPCOLLABORATION collaboration, *Full simulation and performance of a standard iron warm muon shield with tuned return yoke*, .

- [111] P. Wertelaers, *Muon shield concept based on superconducting magnet and tuned iron return yoke*, Tech. Rep. [CERN-SHiP-INT-2022-003](#) (2022).
- [112] SHiP collaboration, *BDF/SHiP muon deflection - First ideas about an integrated apparatus with superconducting main magnet*, .
- [113] M. Ferro-Luzzi, *Preliminary exploration of a superconducting muon shield*, Tech. Rep. [CERN-SHiP-INT-2022-005](#) (2022).
- [114] B. Auchmann, T. Baer, M. Bednarek, G. Bellodi, C. Bracco, R. Bruce, F. Cerutti, V. Chetvertkova, B. Dehning, P.P. Granieri, W. Hofle, E.B. Holzer, A. Lechner, E. Nebot Del Busto, A. Priebe, S. Redaelli, B. Salvachua, M. Sapinski, R. Schmidt, N. Shetty, E. Skordis, M. Solfaroli, J. Steckert, D. Valuch, A. Verweij, J. Wenninger, D. Wollmann and M. Zerlauth, *Testing beam-induced quench levels of lhc superconducting magnets*, [Phys. Rev. ST Accel. Beams](#) **18** (2015) 061002.
- [115] T.A. Collaboration, *The atlas experiment at the cern large hadron collider*, [Journal of Instrumentation](#) **3** (2008) S08003.
- [116] T.C. Collaboration, *The cms experiment at the cern lhc*, [Journal of Instrumentation](#) **3** (2008) S08004.
- [117] SHiP collaboration, *SHiP Experiment - Progress Report*, Tech. Rep. [CERN-SPSC-2019-010, SPSC-SR-248](#), CERN, Geneva (Jan, 2019).
- [118] Synaxis AG, *CERN Prevessin Beam Dump Facility ECN3 & TCC8 - Report of Preliminary Study*, Tech. Rep. [EDMS #2815529](#), Lausanne, Switzerland (2023).
- [119] J. K.Pal, *Technical Report - ECN3 Civil Engineering Study*, Tech. Rep. [EDMS #2895923](#), CERN (2023).
- [120] *Radiation Protection Assessment for BDF/SHiP at ECN3*, Tech. Rep. [EDMS #2911154](#), CERN, Geneva (2023).
- [121] C. Ahdida, D. Bozzato, D. Calzolari, F. Cerutti, N. Charitonidis, A. Cimmino, A. Coronetti, G.L. D'Alessandro, A. Donadon Servelle, L.S. Esposito, R. Froeschl, R. García Alía, A. Gerbershagen, S. Gilardoni, D. Horváth, G. Hugo, A. Infantino, V. Kouskoura, A. Lechner, B. Lefebvre, G. Lerner, M. Magistris, A. Manousos, G. Moryc, F. Ogallar Ruiz, F. Pozzi, D. Prelipcean, S. Roesler, R. Rossi, M. Sabaté Gilarte, F. Salvat Pujol, P. Schoofs, V. Stránský, C. Theis, A. Tsinganis, R. Versaci, V. Vlachoudis, A. Waets and M. Widorski, *New capabilities of the fluka multi-purpose code*, [Frontiers in Physics](#) **9** (2022) .
- [122] G. Battistoni, T. Boehlen, F. Cerutti, P.W. Chin, L.S. Esposito, A. Fassò, A. Ferrari, A. Lechner, A. Empl, A. Mairani, A. Mereghetti, P.G. Ortega, J. Ranft, S. Roesler, P.R. Sala, V. Vlachoudis and G. Smirnov, *Overview of the fluka code*, [Annals of Nuclear Energy](#) **82** (2015) .

- [123] *Safety Code F - Radiation Protection*, Tech. Rep. [EDMS #335729](#), CERN, Geneva (2006).
- [124] R. Acquafredda et al., *The OPERA experiment in the CERN to Gran Sasso neutrino beam*, [JINST **4** \(2009\) P04018](#).
- [125] SND@LHC collaboration, *SND@LHC: The Scattering and Neutrino Detector at the LHC*, [2210.02784](#).
- [126] K. Kodama et al., *Detection and analysis of tau neutrino interactions in DONUT emulsion target*, [Nucl. Instrum. Meth. A **493** \(2002\) 45](#).
- [127] K. Kodama et al., *Momentum measurement of secondary particle by multiple Coulomb scattering with emulsion cloud chamber in DONuT experiment*, [Nucl. Instrum. Meth. A **574** \(2007\) 192](#).
- [128] L. Arrabito et al., *Hardware performance of a scanning system for high speed analysis of nuclear emulsions*, [Nucl. Instrum. Meth. A **568** \(2006\) 578 \[physics/0604043\]](#).
- [129] N. Armenise et al., *High-speed particle tracking in nuclear emulsion by last-generation automatic microscopes*, [Nucl. Instrum. Meth. A **551** \(2005\) 261](#).
- [130] M. Yoshimoto, T. Nakano, R. Komatani and H. Kawahara, *Hyper-track selector nuclear emulsion readout system aimed at scanning an area of one thousand square meters*, [PTEP **2017** \(2017\) 103H01 \[1704.06814\]](#).
- [131] A. Alexandrov et al., *A new fast scanning system for the measurement of large angle tracks in nuclear emulsions*, [JINST **10** \(2015\) P11006](#).
- [132] A. Alexandrov et al., *A new generation scanning system for the high-speed analysis of nuclear emulsions*, [JINST **11** \(2016\) P06002](#).
- [133] A. Alexandrov et al., *The Continuous Motion Technique for a New Generation of Scanning Systems*, [Sci. Rep. **7** \(2017\) 7310](#).
- [134] R. Zimmermann, J. Ebert, C. Hagner, B. Koppitz, V. Savelev, W. Schmidt-Parzefall, J. Sewing and Y. Zaitsev, *The precision tracker of the OPERA detector*, [Nucl. Instrum. Meth. A **555** \(2005\) 435](#).
- [135] K. Bondarenko, A. Boyarsky, O. Mikulenko, R. Jacobsson and M. Ovchinnikov, *Towards the optimal beam dump experiment to search for feebly interacting particles*, 2023.
- [136] P. Wertelaers et al., *SHiP Hidden Sector detector vacuum system*, Tech. Rep. [CERN-SHiP-INT-2019-010](#) (Dec, 2019).
- [137] “<https://www.caen.it/products/a1526/>.”
- [138] “<https://www.caen.it/products/sy4527>.”

- [139] A. Blanco, F. Clemencio, P. Fonte, C. Franco, N. Leonardo, L. Lopes, C. Loureiro, J. Saraiva and G. Soares, *The ship timing detector based on mrpc*, *Journal of Instrumentation* **15** (2020) C10017.
- [140] M. Xarepe, T. Aumann, A. Blanco, A. Corsi, D. Galaviz, H. Johansson, S. Linev, B. Löher, L. Lopes, J. Michel, V. Panin, D. Rossi, J. Saraiva, H. Törnqvist and M. Traxler, *Resistive plate chambers for precise measurement of high-momentum protons in short range correlations at r3b*, *Nuclear Instruments and Methods in Physics Research Section A: Accelerators, Spectrometers, Detectors and Associated Equipment* **1055** (2023) 168445.
- [141] D. Hebecker et al., *A Wavelength-shifting Optical Module (WOM) for in-ice neutrino detectors*, *EPJ Web Conf.* **116** (2016) 01006.
- [142] M. Ehlert, A. Hollnagel, I. Korol, A. Korzenev, H. Lacker, P. Mermod, J. Schliwinski, L. Shihora, P. Venkova and M. Wurm, *Proof-of-principle measurements with a liquid-scintillator detector using wavelength-shifting optical modules*, *JINST* **14** (2019) P03021 [[1812.06460](#)].
- [143] J. Benziger et al., *The Scintillator Purification System for the Borexino Solar Neutrino Detector*, *Nucl. Instrum. Meth. A* **587** (2008) 277 [[0709.1503](#)].
- [144] P. Wertelaers et al., *SHiP Hidden Sector spectrometer magnet*, Tech. Rep. [CERN-SHiP-INT-2019-008](#) (Dec, 2019).
- [145] H. Bajas and D. Tommasini, *SHiP spectrometer magnet – Superconducting options*, Tech. Rep. [CERN-SHiP-NOTE-2022-001](#) (EDMS 2440157) (Apr, 2020).
- [146] N.I. Azorskii et al., *New type of drift tubes for gas-discharge detectors operating in vacuum: Production technology and quality control*, *Phys. Part. Nucl. Lett.* **14** (2017) 144.
- [147] D. Sukhonos and A. Zelenov, *Spectrometer Straw Tracker 2017 Test Beam Results*, Tech. Rep. [CERN-SHiP-INT-2019-005](#) (Dec, 2019).
- [148] SHiP collaboration, *SST 2017 test beam: drift time distribution analysis*, .
- [149] SHiP collaboration, *The CERN-2017 engineering design concept of a generic straw station for the Spectrometer Tracker*, Tech. Rep. [CERN-SHiP-INT-2018-001](#) (Dec, 2018).
- [150] SHiP collaboration, *Cemented pack concept for the SHiP spectrometer straw tracker*, .
- [151] D. Bick, S. Bieschke, C. Hagner, B. Kaiser and W. Schmidt-Parzefall, *The Suspended Bridge Design Concept for the SHiP Spectrometer Straw Tracker*, Tech. Rep. [CERN-SHiP-INT-2019-006](#) (Dec, 2019).
- [152] P. Wertelaers, *Expanding piano frame for Straw Tracker*, Tech. Rep. [CERN-SHiP-INT-2019-007](#) (Dec, 2019).

- [153] C. Betancourt et al., *Application of large area SiPMs for the readout of a plastic scintillator based timing detector*, *JINST* **12** (2017) P11023 [[1709.08972](#)].
- [154] A. Korzenev et al., *Plastic scintillator detector with the readout based on an array of large-area SiPMs for the ND280/T2K upgrade and SHiP experiments*, in *International Workshop on New Photon Detectors (PD18)* Tokyo, Japan, November 27-29, 2018, 2019 [[1901.07785](#)].
- [155] SHiP collaboration, *Studies for the electro-magnetic calorimeter SplitCal for the SHiP experiment at CERN with shower direction reconstruction capability*, *JINST* **13** (2018) C02041.
- [156] M. Anelli et al., *A Facility to Search for Hidden Particles (SHiP) at the CERN SPS - the SHiP physics case*, Tech. Rep. [CERN-SPSC-2015-017](#), SPSC-P-350-ADD-1, SPSC-P-350-ADD-1, [[1504.04855](#)], CERN, Geneva (Apr, 2015).
- [157] W. Baldini, A. Blondel, A. Calcaterra, R. Jacobsson, A. Khotjantsev, Y. Kudenko, V. Kurochka, G. Lanfranchi, A. Mefodiev, O. Mineev, A. Montanari, E.N. Messomo, A. Saputi and N. Tosi, *Measurement of parameters of scintillating bars with wavelength-shifting fibres and silicon photomultiplier readout for the SHiP muon detector*, *Journal of Instrumentation* **12** (2017) P03005.
- [158] M. Ovchinnikov, J.-L. Tastet, O. Mikulenko and K. Bondarenko, *Sensitivities to feebly interacting particles: public and unified calculations*, [2305.13383](#).
- [159] I. Esteban, M.C. Gonzalez-Garcia, M. Maltoni, T. Schwetz and A. Zhou, *The fate of hints: updated global analysis of three-flavor neutrino oscillations*, *JHEP* **09** (2020) 178 [[2007.14792](#)].
- [160] A. De Roeck, M. Ferrillo and M. Ovchinnikov, *Exploration of the physics reach of emulsion and liquid argon options at the ECN3 hall*, .
- [161] Y. Nakamura et al., *Performance of an emulsion telescope for gamma-ray observations in the GRAINE2018 balloon-borne experiment*, *PTEP* **2021** (2021) 123H02.
- [162] CHORUS collaboration, *Observation of one event with the characteristics of associated charm production in neutrino charged-current interactions*, *Phys. Lett. B* **539** (2002) 188.
- [163] HERA-B collaboration, *Measurement of D^0 , D^+ , D_s^+ and D^{*+} Production in Fixed Target 920-GeV Proton-Nucleus Collisions*, *Eur. Phys. J. C* **52** (2007) 531 [[0708.1443](#)].
- [164] G. De Lellis, A.M. Guler, J. Kawada, U. Kose, O. Sato and F. Tramontano, *Search for charmed pentaquarks in high energy anti-neutrino interactions*, *Nucl. Phys. B* **763** (2007) 268.

- [165] G. Radel and R. Beyer, *Neutrino electron scattering*, *Mod.Phys.Lett.* **A8** **1067–1088** ((1993)) .
- [166] LEBC-EHS collaboration, *Charm Hadron Properties in 400-GeV/c p p Interactions*, *Z. Phys. C* **40** (1988) 321.
- [167] DsTAU collaboration, *DsTau: Study of tau neutrino production with 400 GeV protons from the CERN-SPS*, *JHEP* **01** (2020) 033 [[1906.03487](#)].
- [168] SHiP collaboration, *Track reconstruction and matching between emulsion and silicon pixel detectors for the SHiP-charm experiment*, *JINST* **17** (2022) P03013 [[2112.11754](#)].
- [169] SHiP collaboration, *Reconstruction of 400 GeV/c proton interactions with the SHiP-charm project*, Tech. Rep. [CERN-SHiP-NOTE-2020-002](#) (Nov, 2020).
- [170] A. Blanco et al., *TRAGALDABAS: a new RPC based detector for the regular study of cosmic rays*, *Journal of Instrumentation* **9** (2014) C09027.
- [171] “<https://meetingorganizer.copernicus.org/egu2019/orals/31219>.”
- [172] P. Abreu et al., *Marta: a high-energy cosmic-ray detector concept for high-accuracy muon measurement*, *The European Physical Journal C* **78** (2018) 333.
- [173] J. Alabau-Gonsalvo et al., *The CERN Neutrino Beam to Pyhäsalmi - CN2PY: Conceptual design report*, Tech. Rep. , CERN, Geneva (2015).
- [174] M. Vadai et al., “Beam loss and transmission along the chain.” 5 - 8 Dec 2022.
- [175] M. Vadai, A. Alomainy, H. Damerau, M. Giovannozzi and A. Huschauer, *Barrier bucket gymnastics and transversely split proton beams: Performance at the cern proton and super proton synchrotrons*, *Phys. Rev. Accel. Beams* **25** (2022) 050101.
- [176] H. Damerau, A. Funken, R. Garoby, S. Gilardoni, B. Goddard, K. Hanke, A. Lombardi, D. Manglunki, M. Meddahi, B. Mikulec, G. Rumolo, E. Shaposhnikova, M. Vretenar and J. Coupard, *LHC Injectors Upgrade, Technical Design Report* (2014), [10.17181/CERN.7NHR.6HGC](#).
- [177] E. Shaposhnikova, G. Arduini, T. Bohl, M. Chanel, R. Garoby, S. Hancock, K. Hanke, T.P.R. Linnecar, R. Steerenberg and B. Vandorpe, *Recent intensity increase in the CERN accelerator chain – Proceedings of 21st IEEE Particle Accelerator Conference, Knoxville, TN, USA, 16 - 20 May 2005*, Tech. Rep. [CERN-AB-2005-029](#) (2005).
- [178] F.M. Velotti, L.S. Esposito, M.A. Fraser, V. Kain, S. Gilardoni, B. Goddard, M. Pari, J. Prieto, R. Rossi, W. Scandale, L.S. Stoel, F. Galluccio, M. Garattini and Y. Gavrikov, *Septum shadowing by means of a bent crystal to reduce slow extraction beam loss*, *Phys. Rev. Accel. Beams* **22** (2019) 093502.

- [179] M.A. Fraser, B. Goddard, V. Kain, M. Pari, F.M. Velotti, L.S. Stoel and M. Benedikt, *Demonstration of slow extraction loss reduction with the application of octupoles at the CERN Super Proton Synchrotron*, *Phys. Rev. Accel. Beams* **22** (2019) 123501.
- [180] M. Ferrari, R.G. Alía, T. Giles, D. Senajova, S. Pandini, A. Zenoni and M. Calviani, ‘radiation to materials’ at cern, *IEEE Transactions on Nuclear Science* (2023) 1.
- [181] FOR THE N_TOF COLLABORATION collaboration, *Design development and implementation of an irradiation station at the neutron time-of-flight facility at CERN*, *Phys. Rev. Accel. Beams* **25** (2022) 103001.
- [182] F. Ravotti, N. Pacifico, R. Garcia Alia and S. Danzeca, *CERN Radiation Test Facilities Steering Group (RTF-SG)*, 2021.
<https://edms.cern.ch/document/2446501/1>.
- [183] F. Miringone, M. Calviani, C. Torregrosa Martin, O. Aberle, M. Bacak, E. Chiaveri, E. Fornasiere, A. Perillo-Marcone, V. Vlachoudis and t. n_TOF Collaboration, *Development of a neutron imaging station at the n-tof facility of cern and applications to beam intercepting devices*, *Instruments* **3** (2019) .
- [184] G. Gervino, O. Aberle, A.-P. Bernardes, N. Colonna, S. Cristallo, M. Diakaki, S. Fiore, A. Manna, C. Massimi, P. Mastinu, A. Mengoni, R. Mucciola, E. Musacchio González, N. Patronis, E. Stamati, P. Vaz and R. Vlastou, *Near: A new station to study neutron-induced reactions of astrophysical interest at cern-n-tof*, *Universe* **8** (2022) .
- [185] ARGONeUT collaboration, *Improved Limits on Millicharged Particles Using the ArgoNeuT Experiment at Fermilab*, *Phys. Rev. Lett.* **124** (2020) 131801 [[1911.07996](#)].
- [186] ARGONeUT collaboration, *First Constraints on Heavy QCD Axions with a Liquid Argon Time Projection Chamber Using the ArgoNeuT Experiment*, *Phys. Rev. Lett.* **130** (2023) 221802 [[2207.08448](#)].
- [187] ARGONeUT collaboration, *New Constraints on Tau-Coupled Heavy Neutral Leptons with Masses mN=280–970 MeV*, *Phys. Rev. Lett.* **127** (2021) 121801 [[2106.13684](#)].
- [188] MICROBooNE collaboration, *Search for long-lived heavy neutral leptons and Higgs portal scalars decaying in the MicroBooNE detector*, *Phys. Rev. D* **106** (2022) 092006 [[2207.03840](#)].
- [189] DARKSIDE collaboration, *Search for Dark Matter Particle Interactions with Electron Final States with DarkSide-50*, *Phys. Rev. Lett.* **130** (2023) 101002 [[2207.11968](#)].
- [190] M. Breitbach, L. Buonocore, C. Frugueule, J. Kopp and L. Mittnacht, *Searching for physics beyond the Standard Model in an off-axis DUNE near detector*, *JHEP* **01** (2022) 048 [[2102.03383](#)].

- [191] I. Bezshyiko et al., *TauFV: a fixed-target experiment to search for flavour violation in tau decays*, submitted to EPPSU, 2018.
- [192] S. Péraire, M. Ross and J.M. Zazula, *The SPS Target Station for CHORUS and NOMAD Neutrino Experiments*, .

SHiP Collaboration

R. Albanese^{16,d,f}, J. Alt⁸, A. Alexandrov^{16,d}, S. Aoki¹⁹, D. Aritunov¹⁰, A. Bay³¹, C. Betancourt³², I. Bezshyiko³², O. Bezshyyko³⁸, D. Bick⁹, A. Blanco²⁸, M. Bogomilov¹, I. Boiarska⁵, K. Bondarenko^{27,38}, W.M. Bonivento¹⁵, A. Boyarsky^{27,38}, M. Böhles¹¹, D. Breton⁶, A. Brignoli⁷, A. Buonaura³², S. Buontempo¹⁶, M. Campanelli³⁷, D. Centanni¹⁶, K.-Y. Choi²⁶, M. Climescu¹¹, A. Conaboy⁷, L. Congedo^{13,a}, M. Cristinziani¹², A. Crupano¹⁴, G.M. Dallavalle¹⁴, N. D'Ambrosio¹⁷, R. de Asmundis¹⁶, P. de Bryas³¹, J. De Carvalho Saraiva²⁸, G. De Lellis^{16,c}, M. de Magistris^{16,c}, A. De Roeck³⁰, M. De Serio^{13,a}, D. De Simone³², P. Dergachevⁱ, P. Deucher¹¹, A. Di Crescenzo^{16,30,c}, H. Dijkstraⁱ, O. Durhan³³, E. Elikkaya³³, F. Fedotovs³⁷, M. Ferrillo³², M. Ferro-Luzzi³⁰, R.A. Fini¹³, G. Fiorillo^{16,c}, H. Fischer⁸, P. Fonte²⁸, R. Fresa^{16,f}, T. Fukuda²⁰, G. Galati^{13,a}, L. Golinka-Bezshyyko^{32,38}, A. Golovatiuk^{16,c}, A. Golutvin³⁶, V. Gorkavenko³⁸, E. Graverini³¹, C. Grewing¹⁰, A. M. Guler³³, G.J. Haefeli³¹, C. Hagner⁹, J.C. Helo^{2,4}, E. van Herwijnen³⁶, A. Hollnagel¹¹, A. Iuliano^{16,c}, R. Jacobsson³⁰, M. Jonker³⁰, I. Kadenko³⁸, C. Kamiscioglu³⁴, Y.G. Kim²⁴, N. Kitagawa²⁰, K. Kodama¹⁸, D.I. Kolev¹, M. Komatsu²⁰, V. Kostyukhin¹², L. Krzempek^{2,30}, S. Kuleshov^{2,3}, E. Kurbatovⁱ, H.M. Lacker⁷, O. Lantwinⁱ, A. Lauria^{16,c}, K.S. Lee²⁵, K.Y. Lee²³, N. Leonardo²⁸, V.P. Loschiavo^{16,e}, L. Lopes²⁸, F. Lyons⁸, J. Maalmi⁶, A.-M. Magnan³⁶, A.M. Marshall³⁵, A. Miano^{16,c}, S. Mikado²¹, A. Mikulenko²⁷, M.C. Montesi^{16,c}, K. Morishima²⁰, N. Naganawa²⁰, M. Nakamura²⁰, T. Nakano²⁰, S. Ogawa²², M. Ovchynnikov^{27,38}, N. Owtscharenko¹², B.D. Park²³, A. Pastore¹³, M. Patel³⁶, K. Petridis³⁵, A. Prota^{16,c}, A. Quercia^{16,c}, A. Rademakers³⁰, F. Ratnikovⁱ, F. Redi³⁰, A. Reghunath⁷, H. Rokujo²⁰, O. Ruchayskiy⁵, T. Ruf³⁰, P. Santos Dias³⁰, O. Sato²⁰, W. Schmidt-Parzefall⁹, M. Schumann⁸, N. Serra³², M. Shaposhnikov³¹, L. Shchutska³¹, H. Shibuya²², S. Simone^{13,a}, G. Soares²⁸, J.Y. Sohn²³, A. Sokolenko³⁸, O. Soto^{2,3}, S. Takahashi¹⁹, J.L. Tastet⁵, I. Timiryasov⁵, V. Tioukov¹⁶, D. Tommasini³⁰, D. Treille³⁰, R. Tsenov¹, P. Ulloa^{2,4}, E. Ursovⁱ, G. Vankova-Kirilova¹, S. Vilchinski³⁸, C. Visone^{16,c}, S. van Waasen¹⁰, P. Wertelaers³⁰, M. Wurm¹¹, S. Xella⁵, D. Yilmaz³⁴, C.S. Yoon²³, J. Zamora Saa^{2,3}

¹Faculty of Physics, Sofia University, Sofia, Bulgaria

²Millenium Institute For Subatomic Physics At High-Energy Frontier - SAPHIR, Chile

³Universidad Andrés Bello (UNAB)^h, Santiago, Chile

⁴Universidad De La Serena (ULS)^h, La Serena, Chile

⁵Niels Bohr Institute, University of Copenhagen, Copenhagen, Denmark

⁶IJCLab, CNRS, Université Paris-Saclay, Orsay, France

⁷Humboldt-Universität zu Berlin, Berlin, Germany

⁸Physikalisches Institut, Universität Freiburg, Freiburg, Germany

⁹Universität Hamburg, Hamburg, Germany

¹⁰Forschungszentrum Jülich GmbH (KFA), Jülich , Germany

¹¹Institut für Physik and PRISMA Cluster of Excellence, Johannes Gutenberg Universität Mainz, Mainz, Germany

¹²Universität Siegen, Siegen, Germany

¹³Sezione INFN di Bari, Bari, Italy

¹⁴Sezione INFN di Bologna, Bologna, Italy

¹⁵Sezione INFN di Cagliari, Cagliari, Italy

¹⁶Sezione INFN di Napoli, Napoli, Italy

¹⁷Laboratori Nazionali dell'INFN di Gran Sasso, L'Aquila, Italy

¹⁸Aichi University of Education, Kariya, Japan

¹⁹Kobe University, Kobe, Japan

²⁰Nagoya University, Nagoya, Japan

²¹College of Industrial Technology, Nihon University, Narashino, Japan

²²Toho University, Funabashi, Chiba, Japan

²³Physics Education Department & RINS, Gyeongsang National University, Jinju, Korea

²⁴Gwangju National University of Education^d, Gwangju, Korea

²⁵Korea University^d, Seoul, Korea

²⁶Sungkyunkwan University^d, Suwon-si, Gyeong Gi-do, Korea

²⁷University of Leiden, Leiden, The Netherlands

²⁸LIP, Laboratory of Instrumentation and Experimental Particle Physics, Portugal

²⁹Institute of Physics, University of Belgrade, Serbia

³⁰European Organization for Nuclear Research (CERN), Geneva, Switzerland

³¹École Polytechnique Fédérale de Lausanne (EPFL), Lausanne, Switzerland

³²Physik-Institut, Universität Zürich, Zürich, Switzerland

³³Middle East Technical University (METU), Ankara, Turkey

³⁴Ankara University, Ankara, Turkey

³⁵H.H. Wills Physics Laboratory, University of Bristol, Bristol, United Kingdom

³⁶Imperial College London, London, United Kingdom

³⁷University College London, London, United Kingdom

³⁸STFC Rutherford Appleton Laboratory, Didcot, united Kingdom

³⁹Taras Shevchenko National University of Kyiv, Kyiv, Ukraine

^aUniversità di Bari, Bari, Italy

^bUniversità di Cagliari, Cagliari, Italy

^cUniversità di Napoli "Federico II", Napoli, Italy

^dAssociated to Gyeongsang National University, Jinju, Korea

^eConsorzio CREATE, Napoli, Italy

^fUniversità della Basilicata, Potenza, Italy

^gUniversità di Napoli Parthenope, Napoli, Italy

^hAssociated to SAPHIR, Chile

ⁱIndividuals who made crucial contributions to this LoI

Following the resolution of the CERN Council, Russian groups participating in the SHiP project are not included in the author list of this document. We acknowledge the contribution of the Russian scientists, in particular A. Anokhina, E. Atkin, N. Azorskiy, A. Bagulya, A.Y. Berdnikov, Y.A. Berdnikov M. Chernyavskiy, V. Dmitrenko, A. Dolmatov, T. Enik, A. Etenko, O. Fedin, K. Filippov, G. Gavrilov, V. Giuliaeva, V. Golovtsov, D. Golubkov, D. Gorbunov, S. Gorbunov, M. Gorshenkov, V. Grachev, V. Grichine, N. Gruzinskii, Yu. Guz, D. Karpenkov, M. Khabibullin, E. Khalikov, A. Khotyantsev, V. Kim, N. Konovalova, I. Korol'ko, I. Krasilnikova, Y. Kudenko, P. Kurbatov, V. Kurochka, E. Kuznetsova, V. Maleev, A. Malinin, A. Mefodev, O. Mineev, S. Nasybulin, B. Obinyakov, N. Okateva, A. Petrov, D. Podgrudkov, N. Polukhina, M. Prokudin, T. Roganova, V. Samsonov, E.S. Savchenko, A. Shakin, P. Shatalov, T. Shchedrina, V. Shevchenko, A. Shustov,

M. Skorokhvatov, S. Smirnov, N. Starkov, P. Teterin, S. Than Naing, S. Ulin, A. Ustyuzhanin, Z. Uteshev, L. Uvarov, K. Vlasik, A. Volkov, R. Voronkov.